# AN ATTEMPT TO MECHANICALLY DETECT NEURONAL SIGNALS

*Xue Ying Chua*

Doctor of Philosophy

Department of Physics

McGill University

Montreal, Quebec

August 2020

A thesis submitted to McGill University in partial fulfilment of the requirements of the degree of Doctor of Philosophy.

# ACKNOWLEDGEMENTS

Firstly, I would like to thank Professor Grutter for entrusting me with this project, and for his guidance throughout the entire process. This has been a rough journey for me, with more downs than ups. Nevertheless, you have been a very patient teacher with me; showing me the ways of a researcher, showing me how to design and perform experiments, and how to interpret the data that is being obtained. Thanks to you, I have grown to be the person that I am, and will continue to apply the skills and knowledge that I have obtained to my future endeavours.

Secondly, thank you to Professor Yoichi Miyahara for assisting me with the fixing, modifications, and troubleshooting of the lab equipment. Without you, I would not have come this far with the integrated set up.

Thirdly, thank you to Dr. Margaret Magdesian, Dr. Ricardo Sanz, and Dr. Tyler Dunn for teaching me how to perform and maintain the various cell cultures.

Special thanks to Dr. Madeleine Anthonisen and Dr. Tyler Enright for being very supportive lab partners. The both of you have provided me with brilliant ideas for my experiment and given me constant encouragement to finish this project. The two of you have motivated me and showed me that there is, indeed, an end to this tunnel.

Thank you to the rest of the Grutter lab members (past and present): Hussain, Matt, Antoine, Aaron, Ann-Laurienne, Zeno, Andreas, Oscar, Harrisson, Rikke, Megan, Jose, and Omur, for your support. I am forever grateful to have such a wonderful group to work with.

Thank you to the staff and technicians: Robert, John, Richard, Eddie, Juan, Louise, and the janitors, who have helped me with the technical and administrative challenges, and of course have contributed to make this journey possible.

Thank you to the collaborators from the Montreal Neurological Institute: Dr. Tyler Dunn, Dr. Carole Farah, Larissa, and Xin Tang for providing me with leftover Aplysia ganglia.

Thank you to Miguel and Prof. Bub from the Physiology department for supplying the cardiomyocyte cell cultures.

Thank you to members of the Hierlemann group in ETH Zurich: Marie, Torsten, Wei, Milosh, Jan, Sydney, Sergey, Frey, Douglas, David, and Professor Hierlemann, for teaching me how to use the CMOS-HDMEA, as well as providing the resources needed for this experiment to work.

Thank you to Dr. Josephine Nalbantoglu and Hui Chen for supplying the U87 glioma cells, and Benjamin D'Anjou for assistance with the calculations.

Thank you to my close friends and family: Susan, Howard, Rose, Zi, Zi Wang, mum, dad, Cedric, Catherine, Clementine, and Meatball, all of whom have provided me with a lot of love and support throughout this journey.

Finally, special thank you to Ms. Thomasina, Cedric, and Meatball for hearing me out and holding my hand during my moments of emotional instability.

# DEDICATION

*To my son, who never left my side throughout the entire writing process.*

# ABSTRACT

This thesis explores the possibility of creating an integrated platform which enables simultaneous measurements of electrical and mechanical signals from neurons. Mechanical cues, in addition to chemical signals, are known to influence and regulate cellular development, processes, and behaviour. In fact, abnormal changes in the mechanical properties of cells are usually an indication of a disease, debilitating condition, inflammation, or damage to the body. The repercussion of mechanical forces on biological cells is apparent, however, not much is known about the exact ways these forces are affecting cells and their overall functionalities. This research lab is primarily focused on studying the physical limitations of neurons as well as exploring alternatives to reconnect and repair severed neuronal connections, which would otherwise be permanently damaged in the central nervous system. However, here, this project is interested in the effects of mechanical deformations on neuronal signalling and vice-versa, thus giving rise to the development of the integrated platform. The atomic force microscope is a versatile tool which allows precise measurements of the elastic modulus of biological samples. Despite it's precision, the importance of modelling the geometry of the sample at the point of contact to obtain an accurate estimation of the elastic modulus is highlighted. Furthermore, the process of setting up an atomic force microscope (AFM) and multielectrode array (MEA) integrated platform is detailed. Challenges and creative solutions, involving noise, geometrical incompatibility, and lack of optical access, during the set-up journey are elaborated. Unfortunately, simultaneous mechanical and electrical measurements were unsuccessful due to the complexity of this particular integrated set up. Nevertheless, this thesis serves as a how-to guide with plenty of room for improvement in developing the next fully functional AFM and high density MEA integrated platform.

# ABRÉGÉ

Cette thèse explore la possibilité de créer une plate-forme intégrée permettant des mesures simultanées de signaux électriques et mécaniques à partir de neurones. Les signaux mécaniques, en plus des signaux chimiques, sont connus pour influencer et réguler le développement, les processus et le comportement cellulaire. En fait, des changements anormaux des propriétés mécaniques des cellules sont généralement le signe d'une maladie, d'un état débilitant, d'une inflammation ou de dommages corporels. La répercussion des forces mécaniques sur les cellules biologiques est évidente, cependant, on ne sait pas grand-chose sur la manière exacte dont ces forces affectent les cellules et leurs fonctionnalités globales. Ce laboratoire de recherche se concentre principalement sur l'étude des limitations physiques des neurones ainsi que sur l'exploration d'alternatives pour reconnecter et réparer les connexions neuronales rompues, qui autrement seraient endommagées de manière permanente dans le système nerveux central. Ici, cependant, ce projet s'intéresse aux effets des déformations mécaniques sur la signalisation neuronale et inversement, donnant ainsi lieu au développement de la plateforme intégrée. Le microscope à force atomique est un outil polyvalent qui permet des mesures précises du module élastique d'échantillons biologiques. Malgré sa précision, l'importance de modéliser la géométrie de l'échantillon au point de contact pour obtenir une estimation précise du module élastique est mise en évidence. En outre, le processus de mise en place d'un microscope à force atomique (AFM) et d'une plate-forme intégrée multiélectrodes (MEA) est détaillé. Les défis et les solutions créatives, impliquant le bruit, l'incompatibilité géométrique et le manque d'accès optique, au cours du procés d'installation sont élaborés. Malheureusement, les mesures mécaniques et électriques simultanées ont échoué en raison de la complexité de cette configuration intégrée particulière. Néanmoins, cette thèse sert de guide pratique avec beaucoup de marge d'amélioration pour le

développement de la prochaine plate-forme intégrée AFM et MEA haute densité entièrement fonctionnelle.

# TABLE OF CONTENTS

# LIST OF FIGURES

# STATEMENT OF ORIGINALITY AND CONTRIBUTIONS

The author claims the following elements of this thesis to be original:

- **Chapter 2: Analysis of AFM data of rat neurons and U87 glioma cells.** Hussain double-checked the author's derivations of the contact mechanics models, while Benjamin showed and helped the author perform calculations in Mathematica. Matlab codes were written and force distance curve analysis was performed with Monserratt. Results of the experimental findings were discussed as a group, involving Monserratt, Hussain, Margaret, and Peter.

- **Chapter 3: Analysis of cortical neuron signals on a CMOS-HDMEA.** CMOS-HDMEA chips and necessary set up were provided by the Hierlemann group. The recordings of rat cortical neuron signals was performed together with Milos, while in-depth analysis of the signals was performed by the author.

- **Chapter 4: Assembling the combined AFM and CMOS-HDMEA set up.** This thesis project was proposed by Margaret and Peter. The author assembled and characterised the combined AFM and CMOS-HDMEA system. Many provided suggestions or taught the author how to solve the individual challenges. The author acknowledges suggestions, help, input, or training by many, as detailed in the following. The author came up with the design for the modified PDMS stamp. Matt introduced the idea concept and first prototype of extended cantilever, while the author performed the rest of the modifications to improve on the extended cantilever. The extended tip cantilever was a suggestion from Peter based on Lynda's thesis project. The author borrowed that idea and made her version of the extended tip cantilevers. The extension cable for the AFM and CMOS-HDMEA set up was made with supplies obtained from the Hierlemann group. Yoichi taught the author and showed her how to solder the electrical connections. To retrieve out of range CMOS-HDMEA signals, a Python script was written by Marie and Urs. The author tested the efficacy of the script and made necessary modifications. Jan provided helpful suggestions to cover the on-chip amplifiers with a biocompatible opaque epoxy, while the author developed the methodology for painting a thin layer of epoxy onto the MEA chip. The finalised CMOS-HDMEA packaging protocol was developed by the author to accommodate the needs of this thesis project, based on modifications from an existing chip packaging protocol by the Hierlemann group. Identification and troubleshooting the sources of noise during the combination of a functioning Bioscope and CMOS-HDMEA, was performed by Yoichi and the author. Modifications to the Bioscope II AFM and solving the challenge of regaining optical access was performed mainly with helpful suggestions from Yoichi. Verifying and testing the combined AFM and CMOS-HDMEA functionality were performed by the author.

- **Chapter 5: Biological cultures and recordings.** Aplysia californica sea slug cultures and sharp electrode recordings on these neurons were performed by the author under the tutelage of Tyler. External stimulation of the Aplysia neuron using a concentric bipolar microelectrode was suggested by Tyler and performed by the author. Forming a methodology to culture Aplysia neurons successfully on the CMOS-HDMEA surface was developed by the author. Optical stimulation of the Aplysia neurons on the CMOS-HDMEA was an approach developed by the author. Cardiomyocytes were provided and cultured on the CMOS-HDMEA surface by Miguel. Recordings and analysis of the cardiomyocyte signals were performed by the author.

# CHAPTER 1

# INTRODUCTION

## 1.1 Motivation

As neurological diseases, spinal cord injuries, cancer, and other such diseases or conditions become more prevalent amongst humans, the need to gain a thorough understanding of the mechanics these systems and cells become more important. We were particularly intrigued by the inability of the central nervous system (CNS) to repair, once damaged following neurodegenerative diseases or spinal cord related injury. Past work in the lab has led to the successful development of a technique to reconnect severed neurons at rates several times higher than that of physiological processes. We proceeded to attempt to answer the question of whether these mechanically reconnected neurons have fully functional electrical connections and physical properties as their healthy counterparts. For that purpose, we attempted to develop a platform that allows simultaneous measurements of mechanical and electrical signals from biological samples, through the combination of an atomic force microscope (AFM) and a complementary metal oxide semiconductor microelectrode array (CMOS-MEA). This thesis is a detailed explanation of the developmental process of the integrated platform.

## 1.2 Background

Neurological dysfunction represents one of the main causes of disability in Canada. Neurological impairment can be a result of diseases such as Alzheimer's disease, amyotrophic lateral sclerosis, brain tumours, or physical traumas such as head and spinal cord injuries. Unfortunately, there is no known cure for most neurological conditions, and patients are left to experience permanent physical disabilities, limitations, and or a complete loss of function that progressively worsens over time. Currently, there exist medication and therapy that are capable of delaying or alleviating symptoms of the disease. However, these remedial treatments are unable to bring about a complete repair or reconnection of damaged neuronal circuits [Federation et al., 1992, Stichel and Müller, 1998, Tator et al., 2007]. As a consequence, the majority of neuroscience research has been devoted to study of the underlying mechanisms of neuronal growth and regeneration, in hopes of discovering a cure to these irremediable neurological impairments.

Neurons, in general, are known to be adaptable and responsive to electrical stimuli (eg. synaptic plasticity in learning and memory) or mechanical deformations (eg. regeneration after physical trauma). Yet, neuronal regeneration is restricted in mammalian adult central nervous system (CNS). The inability for adult CNS neurons to regenerate is believed to be a result of evolutionary adaptations to protect and conserve complex neural networks and processes that were developed in the body, via the release of inhibitory signals into the external environment that inhibit the regenerative abilities of these neurons [David and Aguayo, 1981, Aguayo et al., 1990, Yiu and He, 2006]. In the case of a severed neuron, the tips of the axon swell and develop retraction bulbs instead of new growth cones. The inability to assemble new growth cones compromises axonal guidance, which is a crucial step in neuronal development, thus, rendering the ability to initiate regeneration in the severed neuron impossible [Yiu and He, 2006, Bradke et al., 2012]. Besides that, demyelination and gradual formation of scar tissue by reactive astrocytes at the site of injury generates mechanical obstacles that further inhibits cellular growth [Ramon y Cajal, 1928, Bernstein and Bernstein, 1971, Aguayo et al., 1990, Yiu and He, 2006, Bradke et al., 2012, Chew et al., 2012, Tran et al., 2018]. Other reasons for the inability of CNS neurons to recover include inflammation [Trivedi et al., 2006, Tran et al., 2018, Schwartz and Ramos, 2020], microtubule damage [Kilinc et al., 2008, Magdesian et al., 2012, Johnson et al., 2013], pathologic swelling and loss of functionality due to calcium influx [Coleman, 2005, Beirowski et al., 2010, Magdesian et al., 2012], and axonal damage due mechanical stimulation [Magdesian et al., 2012]. A brief overview of the limitations experienced by an injured adult CNS neuron is depicted in Figure 1–1. Initially, the developing neurons are free to grow and respond to stimuli and guidance molecules, hence allowing for the development of the neural network. Upon maturity, the neurons are myelinated and chondroitin sulphate proteoglycans (CSPGs) are secreted by astrocytes to limit plasticity and sprouting. When an adult neuron is injured, the axon retracts and a retraction bulb is formed at the end. The injured axon is further exposed to additional CSPGs from the astrocytes and glial scars, and other inhibitory molecules derived from the oligodendrocytes and myelin debris.

Through studies of David and Aguayo in 1981, it is known that injured CNS neurons are able to regenerate given a permissive environment, but stimulation and repair of neural circuits in the CNS remain a challenge [David and Aguayo, 1981, Stichel and Müller, 1998]. For one, severed CNS neurons would have to travel a further distance to form a reconnection with the primary neural circuit, due to the increase in size of an adult [He and Jin, 2016]. Furthermore, studying and developing methods to overcome neuronal dysfunction is further complicated by the lack of access and advanced imaging methods to the site of injury [Magdesian et al., 2012]. Without the ability to regenerate neurons over long distances, treatment options would remain restricted to preserving the viability of the injured neurons via reduction of inflammation and swelling in the site of injury, thus limiting functional recovery of the patient [Yiu and He, 2006]. Motivated by the pressing need for new technological advances, Magdesian et al. have developed a novel technique to mechanically reconnect CNS neurons across long distances in vitro via micropipette manipulation [Magdesian et al., 2016]. Albeit being on a fundamental scale, such a technique has opened up avenues for the advancement of treatments and possibly a cure to neurological impairment. To date, we possess insufficient knowledge on the topic of neuronal regeneration in the CNS. We have yet to understand the basic forces and mechanisms that contribute to neuronal growth and regeneration, along with developing a procedure to rewire and restore damaged neuronal circuits in mature CNS systems [Yiu and He, 2003].

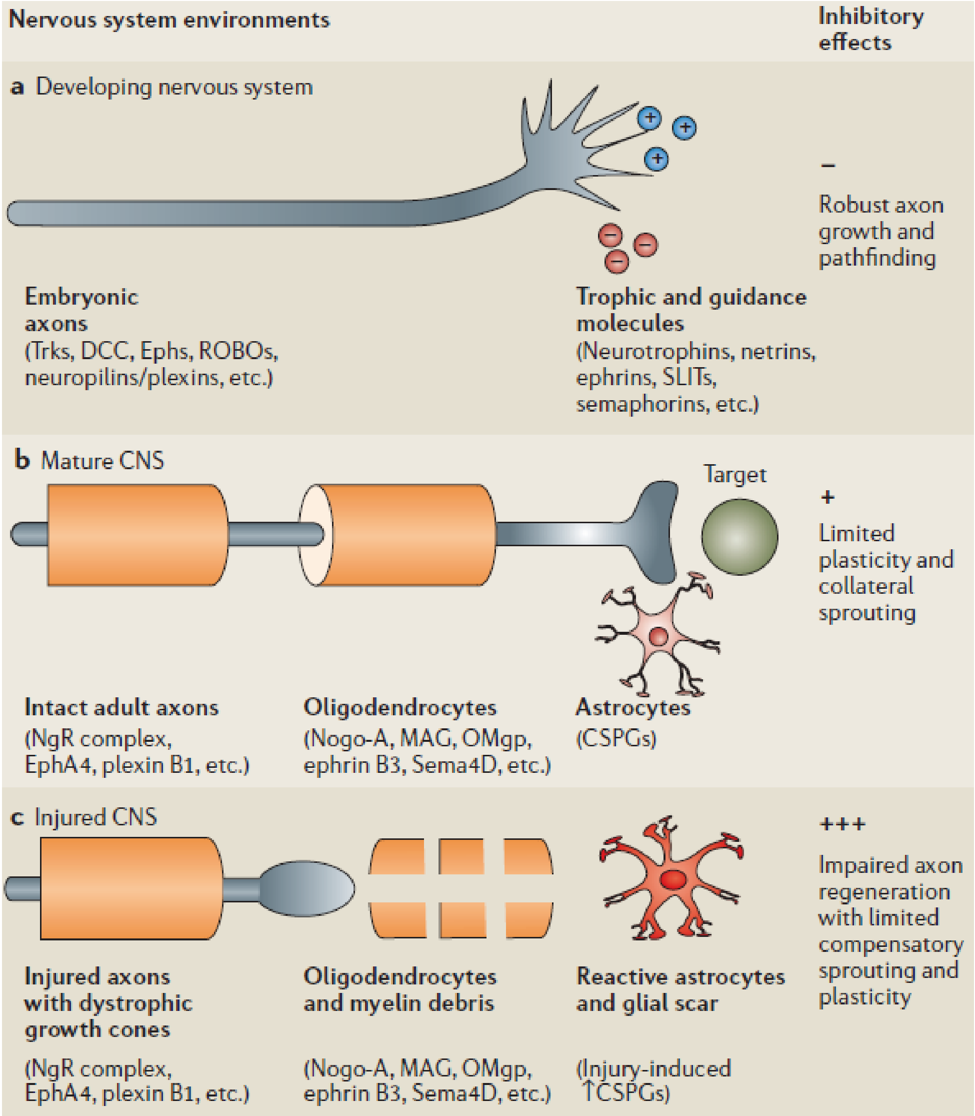

Figure 1–1: **Guidance and inhibitory molecules in the CNS external environment during development, maturation, and after an injury. a.** Developing embryonic neurons face no inhibition during neural development. **b.** Mature neurons become myelinated and CSPGs are secreted by astrocytes to limit plasticity and collateral sprouting. **c.** Injured CNS neurons retract and form a retraction bulb at the end of the axon. The neuron is further subjected to additional CSPGs from astrocytes and glial scars, and inhibitory molecules from oligodendrocytes and myelin debris. The growth and regeneration of neurons is very limited at this point. This figure was obtained with permission from *Glial inhibition of CNS axon regeneration by G. Yiu and Z. He, 2006, Nature Reviews Neuroscience 7(8): 617-627, Copyright © 2006, Springer Nature.*

## 1.3 Aim and thesis outline

The aim of this thesis is to develop an integrated experimental platform allowing simultaneous force and electrophysiological measurements on live cells. Specifically, we hypothesise that the integration of an AFM and a CMOS-MEA would provide a means to perform said measurement on a single neuron. Moreover, the AFM would provide the ability to micromanipulate the neuron and the CMOS-HDMEA would allow us to observe the development of functional electrical connections, all the while building upon the neuronal micropipette manipulation technique developed by Magdesian et al. in 2016.

Chapter 2 investigates the importance of the field of mechanobiology. In a study by Maia and Kutz in 2014, it was shown that individual injured axons can compromise functionality at a network level due to changes in voltage spikes that are delayed, reflected, or deleted, or by the reshaping of spike trains that are attributed to alterations of the geometry of the axon [Maia and Kutz, 2014]. Motivated to find out how neurological dysfunction is affected by the change in physical properties of neurons or how physical changes can eventually lead to impairment, we strove to, first, learn the roles that mechanical cues have on biological cells (not limited to neurons) in regulating cellular processes. This chapter also touches on the effects that mechanical stress can have on cellular viability. Next, we explore and compare popular techniques that enable one to measure physical properties of biological cells. The atomic force microscopy (AFM) technique is heavily discussed, as an introduction to the AFM being one of the key components of the integrated AFM and CMOS-HDMEA set up. Although the AFM is a well-established method, we were aware of the discrepancies in reported elastic modulus values for the same cell type across the literature. As such, the end of Chapter 2 details an experimental approach of obtaining the elastic modulus of cells using the classic Hertz model with the intention to highlight the reasons for the disparities as well as provide the reader with suggestions for improving the measurement.

Chapter 3 explores the fundamental properties of electrical signalling in cells. Returning to the topic of neurological impairment, the function of voltage spikes, also termed as action potentials, is imperative to proper function of neural networks. In this chapter, two types of electrogenic cells, neurons and cardiomyocytes, are discussed as these are the biological samples which are utilised in the following chapters.

The formation of action potentials in each of these cell types are explained to obtain a basic comprehension of the cellular features that give rise to such spikes. Following that, we explore various electrophysiology recording techniques which allow action potentials of cells to be measured. The next half of the chapter is centred around the CMOS-HDMEA, as an introduction to the second key component of the integrated set up. The analysis of recordings of dissociated cortical neurons cultured on a multielectrode array (MEA) will be detailed as a demonstration of the capabilities of this device.

Chapter 4 probes the relationship between electrical signalling and physical properties of biological cells. *How, exactly, is neuronal communication altered following a traumatic brain injury?* We acknowledge the fact the electrical and mechanical properties of cells are adequately understood when studied individually, however, little is known about how these two properties interact with each other. In the beginning, Chapter 4 researches previous studies which have proven that action potential signalling in electrogenic cells are not solely electrical in nature. We also explore previous attempts at modelling these phenomena in hopes of obtaining a better understanding of the link between physical changes and voltage signals in cells. Following that, an overview of advancements in techniques to measure mechanical changes in cells during electrical signalling is discussed. We walk through the process and development of the integrated AFM and CMOS-HDMEA platform, which also happens to be the core of this thesis project and a major contribution to scholarship. Fine details explaining the challenges and measures taken during each step of the process is explained. The chapter concludes with a review of the performance of the integrated set up.

Chapter 5 shows our attempts at utilising the integrated set up with live cells. The process was broken down into several phases to ensure the viability of the cell cultures and to troubleshoot problems pertaining to incorporating biological samples to the integrated platform, with the end goal of performing experiments on an isolated rat neuron. Due to unforeseen circumstances (COVID-19), further efforts at the project had to be halted. Consequently, this phase of the project was unfinished.

Chapter 6 concludes this thesis project. The advantages and disadvantages of the integrated AFM and CMOS-HDMEA platform will be reviewed, and suggestions for improvements of this platform will be listed.

# CHAPTER 2

# MECHANOBIOLOGY OF CELLS

## 2.1 Introduction to mechanobiology

Over a century ago, it was hypothesised that tissue formation was influenced by mechanical forces [Eyckmans et al., 2011]. This statement implied that cellular behaviour is regulated by mechanical signals in addition to chemical signals. Recent studies have shown that manipulation and shaping of cellular processes via biochemical and physical cues are crucial to maintaining proper biological functions in the body [Vogel, 2006, Kim et al., 2009, Tyler, 2012, Jansen et al., 2015, Vogel, 2017]. Multiple operations of varying degrees of complexity are known to be generated and regulated by tensional forces generated by cells themselves; for instance mitochondrial transport (sub-cellular level), cell division (cellular level), tissue formation (multi-cellular level), and contraction of the heart (organ level) [Ingber, 1991, Ingber, 1997, Chicurel et al., 1998, Ingber, 2003, Vogel, 2006, Jacot et al., 2010, Vogel, 2017].

The circulatory system, which encompasses some of the most mechanically active cells in the body, demonstrates the importance of mechanosensing in regulating biological functions in the body. The most notable of this system is the ability of cardiomyocytes to generate and synchronise their contractions across the heart. Cardiomyocytes have the ability to sense mechanical forces at a high level of sensitivity from neighbouring cells and its' surroundings, thus enabling synchronicity in the heart, accurate regulation of hydrostatic pressure, and transportion of blood to the rest of the body [Jacot et al., 2010]. On a lesser known perspective, mechanical changes are also known to occur in the nervous system. As an example, membrane deformations in the axon follow the occurrence of action potentials, mechanical impulses are seen at axon terminals during vesicle fusion, and dendritic spines are known to move in response to synaptic activity. The influence of these mechanical dynamics is evidently crucial to brain function yet remains much less understood [Hill, 1950, Crick, 1982, Tasaki et al., 1989, Star et al., 2002, Tyler, 2012]. Anomalous changes in the mechanical properties of cells can also be an indication of a disease or pathological condition such as cancer. Malignant cells are reported to be 70% less stiff than normal cells. The reduction of stiffness in the extracellular matrix (ECM) is the key to the start and proliferation of cancer [Cross et al., 2007, Lekka and Laidler, 2009]. Although substantial amounts of studies point towards the importance of mechanical forces in biological cells, our understanding on this topic is still inadequate.

Mechanobiology is an interdisciplinary field devoted to understanding the effects that cellular mechanics and mechanical forces have on the behaviour of cells and tissues, by merging and utilising techniques from the fields of biology, neuroscience, physics, and engineering [Kim et al., 2009, Jansen et al., 2015, Krieg et al., 2019]. Mechanobiology branches into two subtopics; the first focusing on the ways cells sense, transduce, and respond to mechanical forces to regulate cellular function, and, the second, on characterising the mechanical properties of cells [Kim et al., 2009].

## 2.2 Techniques in mechanobiology

Advancement of the field of mechanobiology was brought upon predominantly by the development of complex methods and tools, which opened the doors to probing and quantification of mechanical forces in biological samples [Eyckmans et al., 2011]. Figure 2–1 provides an illustration of some of the mechanobiology tools that have been developed or modified to incorporate biological measurements.

- The AFM (Figure 2–1(a)), invented and developed by Binnig et al. in 1986 [Binnig et al., 1986], is an example of a microcantilever-based force sensor. A flexible cantilever (AFM probe) is used to deform the region of interest in a biological sample. Based on the deflection of the cantilever, measured by

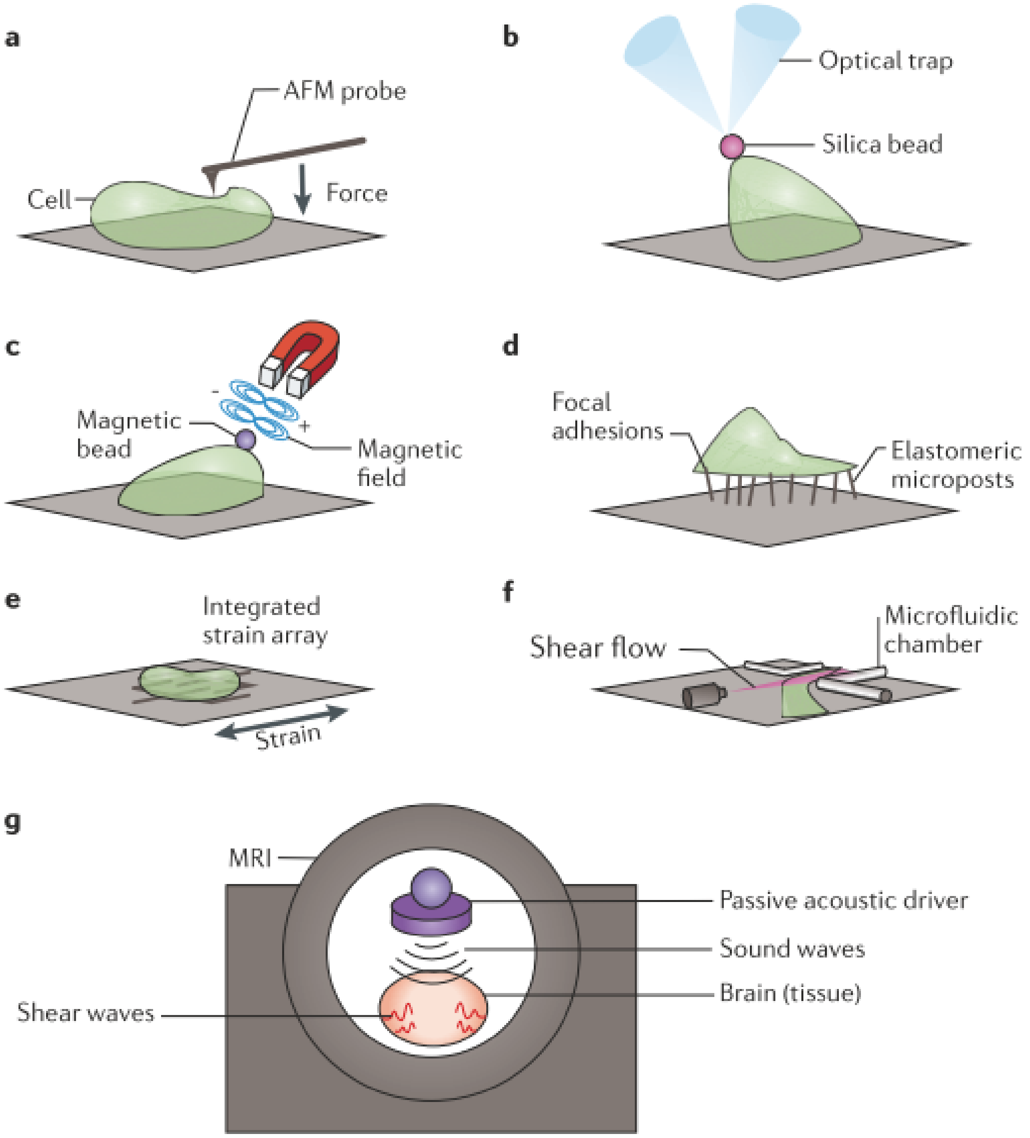

Figure 2–1: **Techniques in mechanobiology a.** Atomic force microscopy. **b.** Optical laser trapping. **c.** Magnetic force spectroscopy. **d.** Microfabricated silicone elastomeric micropost arrays. **e.** Integrated strain array. **f.** Microfluidic chambers. **g.** Magnetic resonance elastography. This figure was obtained with permission from *The mechanobiology of brain function by W. Tyler, 2012, Nature Reviews Neuroscience 13(12):867–878, Copyright © 2012, Springer Nature.*

reflecting a laser beam off the surface of the cantilever tip to a photodiode, high-resolution mechanical measurements of cells, such as the topography or viscoelastic properties, can be extracted [Kim et al., 2009, Tyler, 2012, Ahmed et al., 2015, Chighizola et al., 2019].

- Optical laser trapping, or more commonly known as optical tweezers (Figure 2–1(b)), is a tool that utilises laser beams to trap objects within a defined region. The field of optical laser trapping was first introduced by Arthur Ashkin in 1970s [Ashkin, 1970], an invention in which Ashkin and his team won the 2018 Physics Nobel Prize. Optical laser trapping has since extended its application to biological samples. With this tool, microbeads that are attached to a cell or molecule can be probed by the laser beams. The forces applied to and measured from the cell can be obtained from the forces required to constrain the microbeads [Kim et al., 2009, Tyler, 2012, Ahmed et al., 2015]. Despite the benefits of optical tweezers, long term exposure of cells to the laser beams are known to induce morphology changes [Bronkhorst et al., 1995, Kaneta et al., 2001, Kim et al., 2009].

- Magnetic tweezers are an example of magnetic force spectroscopy (Figure 2–1(c)). Invented by Strick et al. in 1996, magnetic tweezers were used to study the elasticity of supercoiled DNA [Strick et al., 1996]. In this tool, mechanical measurements are obtained by controlling magnetic microbeads, which are attached to the surface of the cell, by magnetic gradient forces or by oscillating magnetic fields [Amblard et al., 1996, Puig-De-Morales et al., 2001, Ahmed et al., 2015]. Advantages of magnetic tweezers over optical tweezers include the ability to manipulate multiple microbeads simultaneously and the prevention of cellular damage by laser beams [Gosse and Croquette, 2002, Danilowicz et al., 2005, Kim et al., 2009, Tyler, 2012, Ahmed et al., 2015, Sarkar and Rybenkov, 2016].

- Microfabricated silicone elastomeric micropost arrays (Figure 2–1(d)) enable the measurement of traction forces of cells. Here, cells are cultured and spread across the micropost arrays. Deflections of the tips of the microposts can be used to derive the position, trajectory, and magnitude of force generated by the cells during cellular migration or contraction. An advantage of this technique includes the ability to modify the substrate stiffness by changing the dimensions or spacing of the microposts, while maintaining the same surface topology and composition [Tan et al., 2003, Sniadecki and Chen, 2007, Kim et al., 2009, Tyler, 2012, Goedecke et al., 2015, Beussman et al., 2016].

- Integrated strain arrays (Figure 2–1(e)) are deformable membranes which subject cell cultures to grow under strain. This technique allows varying strain levels to be applied to different cell populations simultaneously, thus allowing for high-throughput micromechanical, and in some cases, electrical measurements of cell cultures [Simmons et al., 2011, Rajagopalan and Saif, 2011, Tyler, 2012].

- Since the invention and advancement of microfluidic chambers, a vast array of measurements on cells have been made possible depending on the design of the device. In the example shown in Figure 2–1(f), shear force is applied to cells by flowing fluids through the chambers [Taylor et al., 2010, Tyler, 2012]. To date, simultaneous electrical and mechanical measurements on single cells have also been made possible [Chen et al., 2011].

- Magnetic resonance elastography (MRE) (Figure 2–1(g)) is a non-invasive magnetic resonance imaging (MRI) based method for assessing the stiffness of soft tissues in vivo. Low frequency mechanical waves are generated in the tissue, and propagating waves are analysed using a phase contrast MRI technique to obtain the elastograms of tissues. Currently, MREs are used clinically to assess patients with hepatic fibrosis. Research is ongoing to extend the application of MRE to study pathologies of other organs [Mariappan et al., 2010, Tyler, 2012, Venkatesh et al., 2013].

Alternative mechanobiology tools and methodologies include micropipette aspiration, uniaxial stretchers, and traction force microscopy, just to name a few. In short, there exists a device or a combination of devices that allow one to to probe mechanobiological parameters of interest at the molecular, cellular, and multi-cellular levels.

## 2.3 Atomic force microscopy in biology

Since the invention of AFM by Binnig et al. in 1986, this microscope has evolved to incorporate new imaging capabilities, which has enabled the probing and measurements of mechanical properties of living cells, sub-cellular biological components and molecules to tissues under diverse environmental conditions.

Figure 2–2 illustrates the evolution of the AFM. Starting from the first AFM in 1986, the two main technological improvements were the Bio-AFM (Bio-AFM), where optical microscope techniques and fluid cells were incorporated to the AFM platform to enable monitoring and imaging of cells in liquid, and dynamic mode AFM (DM-AFM), where the cantilever tip was made to oscillate while scanning to reduce lateral forces and thus damage to biological samples due to shear forces. From there on, simultaneous measurement modes were enabled, for example, force-distance curve based AFM (FD-AFM) allowed concurrent topographic and force-volume mapping of the sample; multiparametric AFM (MP-AFM) enabled topographic imaging while obtaining physical or chemical measurements from the sample; molecular recognition AFM (MR-AFM) enabled simultaneous imaging and mapping of interactions of samples; multifrequency AFM (MF-AFM) obtained various physical parameters of the sample by oscillating the cantilever at multiple frequencies; combined optical and AFM imaging (Opto-AFM) allowed AFM images to be correlated with advanced optical images; and high-speed AFM (HS-AFM) which made AFM movies possible by increasing the image acquisition time [Dufrêne et al., 2017].

Apart from having diverse functionalities, the primary benefits of AFM include the ability to manipulate and measure forces at the nano-scale, characterise various mechanical parameters such as cell topography, stiffness, adhesion, and viscoelasticity in biological samples, perform live cell imaging in physiological conditions without the need to fix or label cells, and avoid cellular damage via the measuring probe or laser beam exposure [Gavara, 2017, Krieg et al., 2019, Stylianou et al., 2018].

### 2.3.1 Fundamentals of atomic force microscopy

A typical AFM set up is shown in Figure 2–3(a). Biological samples are cultured on a coverslip and placed in a fluid cell, where the sample is probed by a flexible cantilever tip. The cantilever, mounted on the AFM head, has a laser beam focused

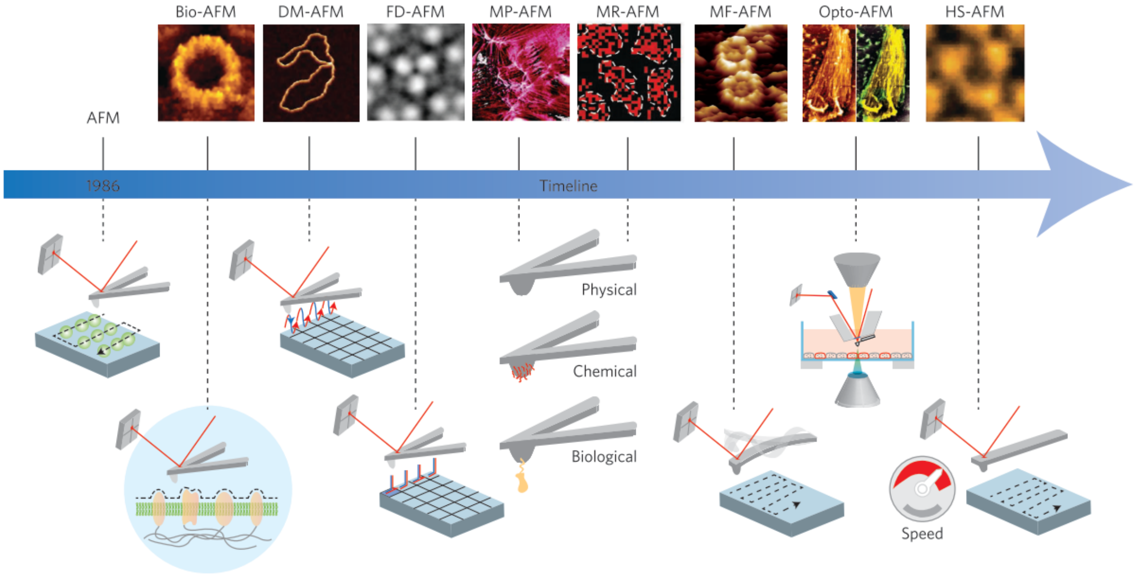

Figure 2–2: **Evolution of the atomic force microscope** From left to right: First AFM invented in 1986, Bio-AFM, dynamic mode AFM, force–distance curve-based AFM, multiparametric AFM, molecular recognition AFM, multifrequency AFM, combined optical and AFM imaging, high- speed AFM. This figure was obtained with permission from *Imaging modes of atomic force microscopy for application in molecular and cell biology by Y. Dufrêne, T. Ando, R. Garcia, D. Alsteens, D. Martinez-Martin, A. Engel, C. Gerber, and D. Müller, 2017, Nature Nanotechnology 12(4):295–307, Copyright © 2017, Springer Nature.*

on the back of the sharp tip. While the cantilever bends in response to forces between the tip and the sample, any horizontal and vertical deflections of the laser beam in the photodetector is recorded [Stylianou et al., 2018].

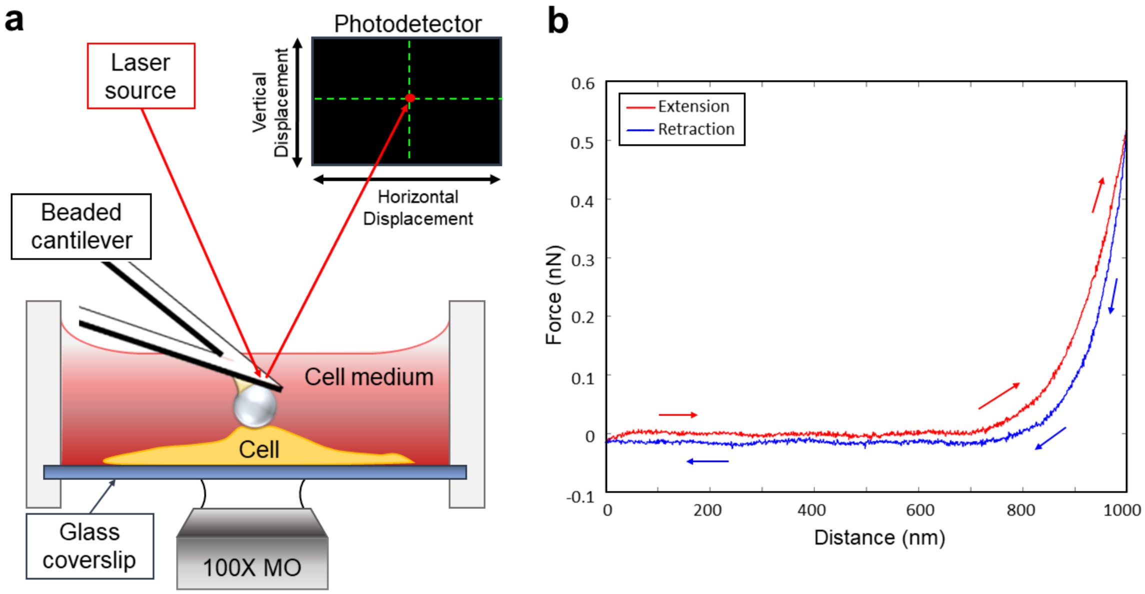

Figure 2–3: **Atomic force microscope set up and force distance curve. a.** Schematic diagram showing an AFM cantilever indenting a cell plated on a glass coverslip. The laser beam focuses on the back of the cantilever and reflects off to a photodetector where horizontal and vertical displacements are measured as the cantilever indents the sample, resulting in a force-distance measurement. A 100X microscope objective (MO) at the bottom of the dish enables sample observation during experiments. **b.** Force-distance curve obtained from the indentation of an axon using a beaded cantilever. The distance indicates the position of the cantilever in the z-axis, while the force is calculated from the measured deflection on the photodetector. The extension curve (red) represents the cantilever during the approach and downward indentation onto the sample, while the retraction curve (blue) represents the withdrawal of the cantilever from the sample.

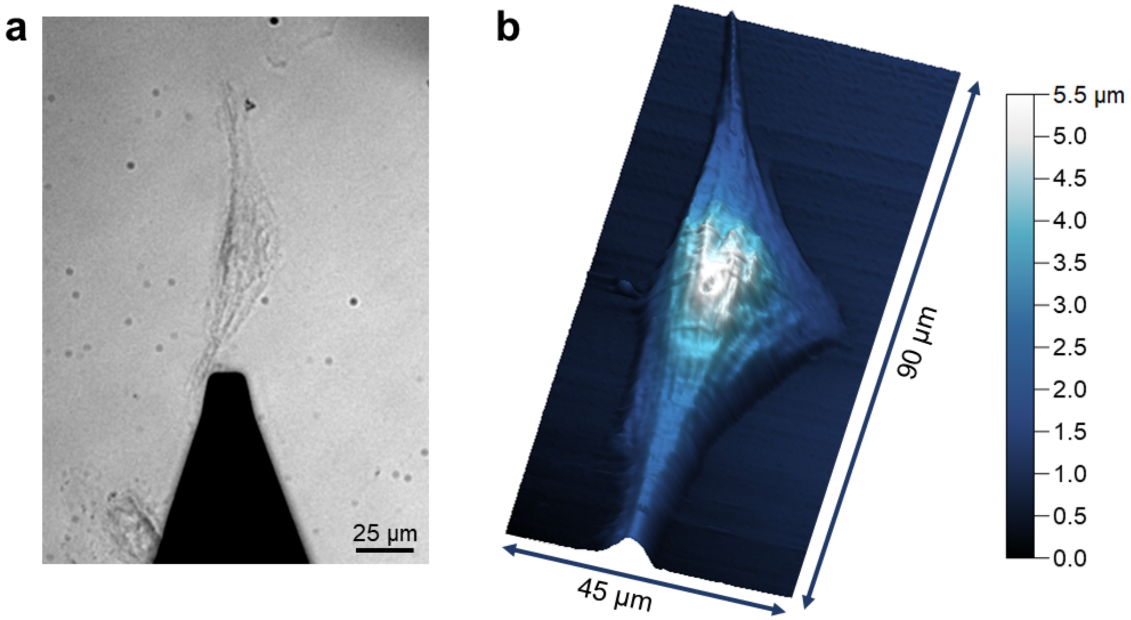

Figure 2–4: **Topographic AFM image of a U87 glioma cell. a.** Optical image of the AFM cantilever (black) scanning a U87 glioma cell. **b.** Height trace of the U87 glioma cell obtained through intermittent contact mode imaging. Experimental protocols are explained in detailed in Section 2.3.2.2.

#### 2.3.1.1 Imaging mode

In AFM imaging mode, topographic images are created by performing a raster scan across the surface of the biological sample. Variations in the morphology of the cell are obtained from the deflection of the cantilever. During the scan, a feedback loop is used to adjust the position of the cantilever with respect to the sample, to keep the deflection constant. In other words, the distance between the tip and the sample is kept constant, while the cantilever scans over the surface of the sample, much like the needle of a turntable. The change in vertical position of the cantilever is then used to obtain the topography of the sample, e.g. Figure 2–4 shows an AFM image of a U87 glioma cell. High resolution AFM imaging has provided a non-invasive avenue for resolving structures of biological samples without detrimental cell staining or labelling [Duman et al., 2012, Gavara, 2017].

#### 2.3.1.2 Force mode

Force imaging mode is used to measure the forces between the tip and sample at a region of interest. To obtain the force-distance (FD) curves, mechanical indentation of local regions on single cells are performed with the AFM. As the cantilever extends towards the cell, an apparent increase in deflection is sensed by the photodetector (Figure 2–3(b) red trace). The point at which the force increases indicates the point of contact between the tip and the sample. The force continues to increase as the tip compresses the sample. Upon reaching a maximum set force, the tip is retracted from the sample until it completely detaches from the surface (Figure 2–3(b) blue trace). The force between the tip and the sample can be calculated following Hooke's law,

$$F = -k\delta_c \tag{2.1}$$

where $\delta_c$ represents the deflection of the cantilever, $F$ represents the tip-sample interaction force, and $k$ represents the spring constant of the cantilever. Based on Equation 2.1, it is crucial select an appropriate cantilever and probe in order to obtain accurate measurements of the mechanical properties of cells. The cantilever chosen has to be similar in stiffness as the biological system to be measured, as a cantilever that is much stiffer than the sample reduces the sensitivity of the cantilever, while a cantilever that is too soft is unable to fully indent the sample [Krieg et al., 2019]. The tip-sample indentation, $\delta_i$, can then be measured by taking the difference between the z-piezo displacement of the AFM, $Z$, and the cantilever deflection $\delta_c$ [Cappella and Dietler, 1999],

$$\delta_i = Z - \delta_c \tag{2.2}$$

As shown in Figure 2–3(b), the extension curve represents the approach and indentation of the cantilever onto the sample, while the retraction curve represents the withdrawal of the cantilever from the sample. Note that the extension and retraction curves are non-identical due to hydrodynamic drag of the cantilever, plastic deformations of the sample, and adhesion between the tip and sample [Smith et al., 2005, Gavara, 2017]. Depending on the parameter to be studied, the force-distance curve can be fitted with the appropriate contact mechanics model to obtain the mechanical property of interest for the biological sample.

#### 2.3.1.3 Contact mechanics models

The selection of the appropriate contact mechanics model depends on the type of tip-sample interaction, type of material (i.e. linear or non-linear elastic), and the geometry of the cantilever tip. The three main contact mechanics models that have been developed over time are the Hertz, Derjaguin-Müller-Toporov (DMT), and Johnson-Kendall-Roberts (JKR) models, as shown in Figure 2–5.

The Hertz model, developed in 1881 to describe the contact between two curved surfaces, is the most widely used model to extract mechanical properties from AFM FD curves. Since then, the Hertz model has been modified for various tip geometries: spherical, cylindrical, conical, parabolic, and blunted pyramidal [Hertz, 1882, Sneddon, 1965, Bilodeau, 1992, Rico et al., 2007]. The major assumptions of the Hertz model include [Hertz, 1882, Puttock and Thwaite, 1969, Johnson, 1982]:

- The surfaces of the indenter and sample are assumed to be homogeneous, continuous, perfectly smooth, and non-conforming (i.e. having dissimilar profiles)
- The strains in the contact region are small and lie within the linear elastic regime of the indenter and sample
- There are no external adhesion or frictional forces within the area of contact, so that only a normal pressure is conducted between the indenter and sample.

Despite the wide use of this model, it is important to note that these assumptions are not realistic in a biological contact. With regards to the first and third assumptions, neither the AFM tips nor the surface of the sample are perfectly smooth, and the force applied by the AFM tip is not normal to the sample due to the tilt in the cantilever on the AFM head. For the second assumption, the empirical rule of thumb is to indent a maximum of 10% of the cell height in order to remain within the linear elastic regime of the Hertz model. For instance, for cell thicknesses of 100 $nm$, this implies indentations no more than 10 $nm$ in depth. For, any further indentation will lead to sub-cellular molecules adding to the elastic modulus measurement [Dimitriadis et al., 2002, Gavara, 2017, Krieg et al., 2019]. Moreover, indentations above

10% of the thickness of the cell allow substrate effects to play a role in the measurement, as supported by AFM and modelling of the mechanical properties using finite element methods [Ladjal et al., 2009, Wang et al., 2019]. Even though the Hertz model assumes that there are no surface forces between the tip and the sample, the hysteresis in the extension and retraction of FD curves indicate otherwise as adhesion is known to be present when indenting cells [Notbohm et al., 2012, Friedrichs et al., 2013, Krieg et al., 2019].

To account for adhesion, the DMT and JKR models were derived. The Derjaguin-Müller-Toporov (DMT) model incorporates attractive forces outside of the area of contact (i.e. long range surface forces) [Derjaguin et al., 1975]. The DMT model also assumes that a stiff sample is indented by an indenter with small-radius, and that the adhesion between the tip and sample is weak. The Johnson-Kendall-Roberts (JKR) model, on the other hand, incorporates attractive forces within the area of contact (i.e. short range surface forces) [Johnson, K. L., Kendall, K. & Roberts, 1971]. This model assumes that a soft sample is being indented by a large-radius indenter, and that the adhesion between the tip and sample is strong. Not shown in Figure 2–5 is the polymer brush model developed by Iyer et al. [Iyer et al., 2009] to take into account long-range interactions due to the presence of brush-type structures on the surface of cells [Gavara, 2017].

### 2.3.2 Effects of cellular morphology on elastic modulus measurements

#### 2.3.2.1 Introduction and motivation

As stated above, one of the aims of this thesis is to lay the foundation to measure forces simultaneously with electrical signals. The mechanical properties of a living cell provides insight on how forces are transmitted though the cell and how changes are induced in the cell's internal environment and performance [Ingber, 1997, Charras and Horton, 2002]. AFM, with the ability to apply exceptional control of forces on cells under nearly physiological conditions and without prior labelling, has enabled the characterisation of elastic modulus (EM) of several cell types, for example, bone cells [Charras et al., 2001, Charras and Horton, 2002, Komarova et al., 2014], cancer cells [Lekka and Laidler, 2009, Lekka et al., 2012], airway smooth muscle cells [Smith

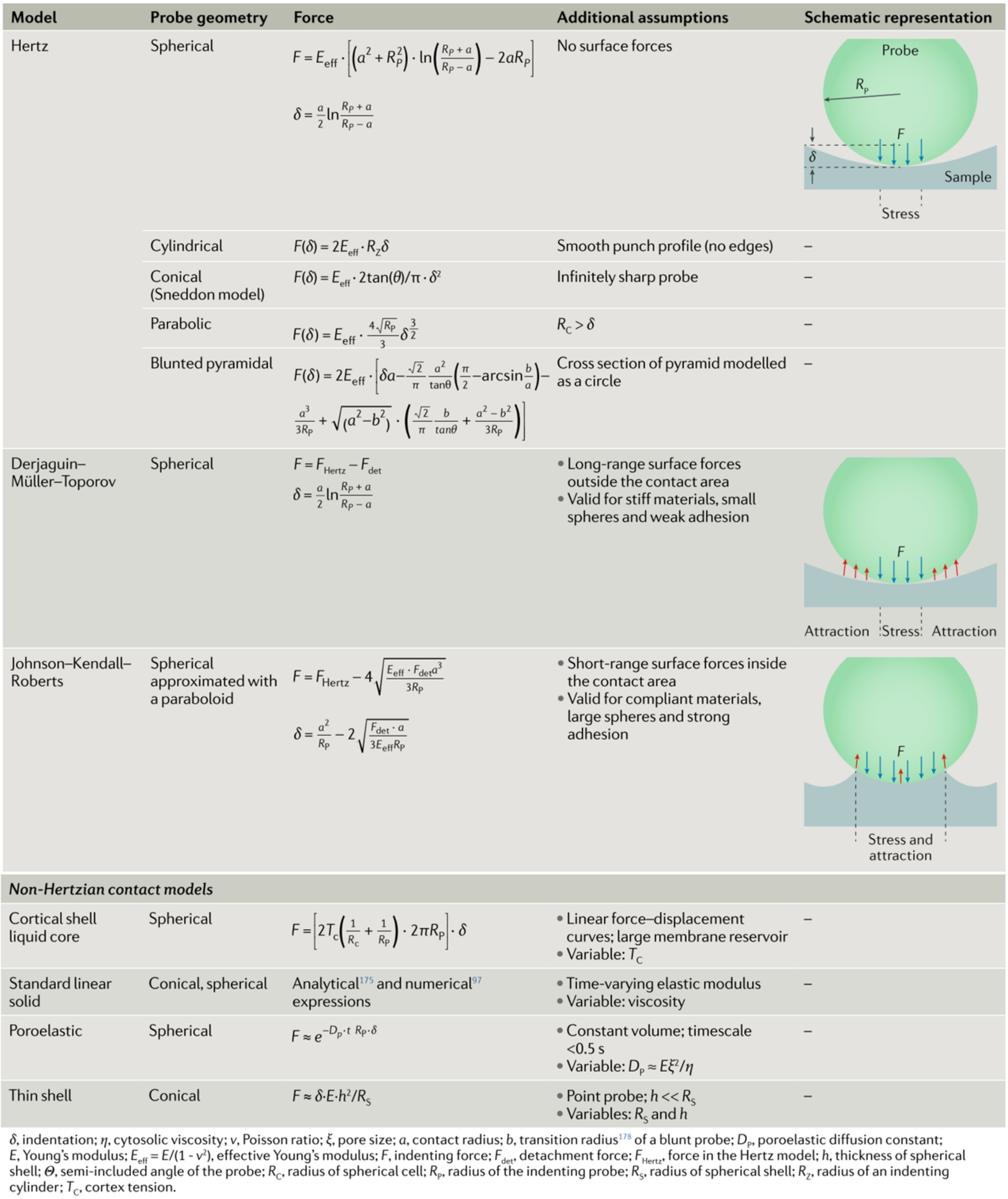

| Model | Probe geometry | Force | Additional assumptions | Schematic representation |
|---|---|---|---|---|
| Hertz | Spherical | $F = E_{\mathrm{eff}} \cdot \left[ \left(a^2 + R_P^2\right) \cdot \ln\left(\frac{R_P + a}{R_P - a}\right) - 2aR_P \right]$<br>$\delta = \frac{a}{2} \ln \frac{R_P + a}{R_P - a}$ | No surface forces | |
| | Cylindrical | $F(\delta) = 2E_{\mathrm{eff}} \cdot R_Z \delta$ | Smooth punch profile (no edges) | – |
| | Conical (Sneddon model) | $F(\delta) = E_{\mathrm{eff}} \cdot 2\tan(\theta)/\pi \cdot \delta^2$ | Infinitely sharp probe | – |
| | Parabolic | $F(\delta) = E_{\mathrm{eff}} \cdot \frac{4\sqrt{R_P}}{3} \delta^{\frac{3}{2}}$ | $R_C > \delta$ | – |
| | Blunted pyramidal | $F(\delta) = 2E_{\mathrm{eff}} \cdot \left[ \delta a - \frac{\sqrt{2}}{\pi} \frac{a^2}{\tan\theta} \left(\frac{\pi}{2} - \arcsin\frac{b}{a}\right) - \frac{a^3}{3R_P} + \sqrt{(a^2 - b^2)} \cdot \left( \frac{\sqrt{2}}{\pi} \frac{b}{\tan\theta} + \frac{a^2 - b^2}{3R_P} \right) \right]$ | Cross section of pyramid modelled as a circle | – |
| Derjaguin–Müller–Toporov | Spherical | $F = F_{\mathrm{Hertz}} - F_{\mathrm{det}}$<br>$\delta = \frac{a}{2} \ln \frac{R_P + a}{R_P - a}$ | • Long-range surface forces outside the contact area<br>• Valid for stiff materials, small spheres and weak adhesion | |
| Johnson–Kendall–Roberts | Spherical approximated with a paraboloid | $F = F_{\mathrm{Hertz}} - 4\sqrt{\frac{E_{\mathrm{eff}} \cdot F_{\mathrm{det}} a^3}{3R_P}}$<br>$\delta = \frac{a^2}{R_P} - 2\sqrt{\frac{F_{\mathrm{det}} \cdot a}{3E_{\mathrm{eff}} R_P}}$ | • Short-range surface forces inside the contact area<br>• Valid for compliant materials, large spheres and strong adhesion | |
| ***Non-Hertzian contact models*** | | | | |
| Cortical shell liquid core | Spherical | $F = \left[ 2T_c \left( \frac{1}{R_c} + \frac{1}{R_P} \right) \cdot 2\pi R_P \right] \cdot \delta$ | • Linear force–displacement curves; large membrane reservoir<br>• Variable: $T_C$ | – |
| Standard linear solid | Conical, spherical | Analytical[175] and numerical[97] expressions | • Time-varying elastic modulus<br>• Variable: viscosity | – |
| Poroelastic | Spherical | $F \approx e^{-D_p \cdot t \; R_P \cdot \delta}$ | • Constant volume; timescale <0.5 s<br>• Variable: $D_p \approx E\xi^2/\eta$ | – |
| Thin shell | Conical | $F \approx \delta \cdot E \cdot h^2/R_S$ | • Point probe; $h << R_S$<br>• Variables: $R_S$ and $h$ | – |

$\delta$, indentation; $\eta$, cytosolic viscosity; $v$, Poisson ratio; $\xi$, pore size; $a$, contact radius; $b$, transition radius[178] of a blunt probe; $D_p$, poroelastic diffusion constant; $E$, Young's modulus; $E_{\mathrm{eff}} = E/(1 - v^2)$, effective Young's modulus; $F$, indenting force; $F_{\mathrm{det}}$, detachment force; $F_{\mathrm{Hertz}}$, force in the Hertz model; $h$, thickness of spherical shell; $\Theta$, semi-included angle of the probe; $R_C$, radius of spherical cell; $R_P$, radius of the indenting probe; $R_S$, radius of spherical shell; $R_Z$, radius of an indenting cylinder; $T_C$, cortex tension.

Figure 2–5: **Contact mechanical models** Force equations for the Hertz, Derjaguin-Müller-Toporov (DMT), and Johnson-Kendall-Roberts (JKR) are listed. Each equation corresponds to a specific tip geometry and assumption. For the purpose of this thesis, only the Hertzian contact mechanics models will be discussed. This figure was obtained with permission from *Atomic force microscopy-based mechanobiology by M. Krieg, G. Fläschner, D. Alsteens, B. Gaub, W. Roos, G. Wuite, H. Gaub, C. Gerber, Y. Dufrêne, and D. Müller, 2019, Nature Reviews Physics 1(1):41–57, Copyright © 2018, Springer Nature.*

et al., 2005], and neurons [Mustata et al., 2010, Bernick et al., 2011, Magdesian et al., 2012, Spedden et al., 2012a, Spedden et al., 2012b, Martin et al., 2013].

However, the estimated elastic modulus values for the same cell presented by different publications vary by several orders of magnitude, as shown in Figure 2–10. The differences in elastic modulus values result in the opportunity to draw any conclusion based solely on a comparison of the elastic modulus values impossible [Mustata et al., 2010, Spedden et al., 2012b]. It is well known that the large variation in elastic modulus values can be attributed to biological differences (e.g. cell types, phenotype, developmental cycle, or non-homogeneity of nominally identical cells), differences in the parameters for measuring the elastic modulus (e.g. maximum force applied by the cantilever, rate of indentation, type of cantilever tips), and differences in the methodology for extracting the elastic modulus (e.g. methodology of data analysis, contact point determination) [Sokolov, 2007, Gavara, 2017, Zemła et al., 2018].

The Hertz contact mechanics model is the most widely applied model to estimate the elastic modulus for biological samples in the AFM community. Depending on the geometry of the cantilever tip, the classic Hertz's sphere on a plane (for a spherical tip) and Sneddon's cone on a plane model (for a pyramidal tip) are used [Magdesian et al., 2012, Mustata et al., 2010, Spedden et al., 2012b, Andolfi et al., 2014]. These models assume the sample to be planar, however, not all cells are flat. Biological cells come in a wide variety of shapes and sizes [Kuznetsova et al., 2007, Mustata et al., 2010, Magdesian et al., 2012, Martin et al., 2013]. Neurons, for instance, are composed of a round cell body and multiple cylindrical extensions that constitute axons and dendrites. Therefore, the geometrical approximations of the contact mechanical model should be adjusted depending on the geometry of the region of indentation.

In this section, the importance of taking into account the cell morphology to achieve an accurate elastic modulus value will be demonstrated. FD curves obtained using the AFM on two different samples, rat dorsal root ganglion neurons (DRG) and U87 glioma cells, were evaluated using three different contact mechanic models which differ only by the geometric representation of the sample. The results indicate significant differences in the elastic modulus values obtained despite having the same cells and experimental parameters. Therefore, emphasising the importance of taking the sample shape into consideration when quantitatively analysing the AFM elastic modulus data.

### 2.3.2.2 Materials and methods

#### Cell cultures

All animal experimentation were approved by the institutional animal care committee and conformed to the guidelines of the Canadian Council of Animal Care. DRG neurons from Sprague Dawley rat embryos at embryonic day 18–19 (E18–E19) of either sex (Charles River, Wilmington, MA) were prepared as previously described [Magdesian et al., 2012]. Neurons were plated in polydimethysiloxane (PDMS) microfluidic chambers (Advanced Nano Design Applications, Montreal, QC, CA) mounted on $35mm$ glass-bottom dishes (MatTex, Ashland, MA) coated with $100\mu g/mL$ poly-d-lysine solution (Sigma-Aldrich, St. Louis, MO). Cells were kept in neurobasal medium supplemented with L-glutamine, penicillin-streptomycin, and serum-free B-27 supplement (Invitrogen, Life Technologies Inc., Ontario, Canada) in an incubator at $37°C$ with 5% $CO_2$. The microfluidic chambers were removed 8–10 days after cell plating. U87 glioma cell line (courtesy of Dr. Josephine Nalbantoglu, Department of Neurology, Neurosurgery and Medicine, McGill University, Montreal, QC, CA) were plated onto $25mm$ No.1 glass coverslips (MatTex, Ashland, MA) and cultured in Dulbecco's modified eagle medium containing 10% heat-inactivated fetal bovine serum and penicillin-streptomycin (Invitrogen, Life Technologies, Inc., Ontario, Canada), as described [Li et al., 1999]. Glioma cells were kept in an incubator at $37°C$ with 5% $CO_2$ and washed with phosphate-buffered saline solution before experimentation.

#### Atomic force microscopy

**Imaging:** Experiments were conducted using two different AFM setups: a Bioscope II AFM (Veeco, Plainview, NY) and the MFP-3D-BIO AFM (Asylum Research, Santa Barbara, CA). Rat DRG neurons were imaged at $37°C$ with $CO_2$ supply on the Bioscope AFM, mounted on top of an inverted optical microscope (Axiovert S100TV, Carl Zeiss, Toronto, Ontario, Canada), using a 100X microscope oil objective lens, as shown in the schematic diagram of Figure 2–3 (a). Sequential images of the neurons were acquired using a 1 K charge-coupled device (CCD) camera (Photometrics, Tucson, AZ, USA). Glioma cells are imaged at $37°C$ on a MFP-3D-BIO AFM, mounted on top of an Olympus IX-71 inverted optical microscope with a 40X microscope objective lens. Sequential images are acquired using a liquid-cooled Cascade II CCD camera (Photometrics, Tucson, AZ, USA). In both cases, cells were observed from below the dish through the optical microscope, while the AFM probe accessed the sample from above. The region of interest was located and aligned with the cantilever tip using the optical microscope and cantilever deflection as a guide. To obtain topographic images, the cells were fixed using 4% paraformaldehyde and probed using intermittent contact mode imaging in liquid with an applied force of $0.03nN$ at a scan rate of $0.1Hz$.

**FD-cuves:** Silicon nitride probes (Cat. No. MSCT-AUHW, Microlevers, Veeco) with a nominal spring constant of $k = 0.01N/m$ were used as AFM cantilevers. A 20 $\mu m$ polysterene bead (Polysciences, Warrington, PA) was attached to the tip of each cantilever using epoxy structural adhesive (Loctite E-30C Hysol, Henkel, AU), to prevent the sharp tip of the AFM cantilever from piercing the cell membrane. Before each experiment, the cantilevers were calibrated and the spring constant was measured by applying the thermal noise method described by Hutter and Bechhoefer [Hutter and Bechhoefer, 1993]. Using a built-in calibration software, the power spectrum of the thermal fluctuations was measured. By taking the integral of the power spectrum, the mean-square fluctuations of the cantilever, $< x^2 >$, can be used to estimate the spring constant, $k$, given by this equation:

$$k = \frac{k_B T}{< x^2 >} \tag{2.3}$$

where $k_B$ and $T$ are the Boltzmann's constant and temperature respectively. For this experiment, the average spring constants were determined to be $k = 0.010 \pm 0.003N/m$. Forces of $0.3 \pm 0.1nN$ were applied every 15 seconds on top of the axons of rat DRG neurons and on top of the cell body of the U87 glioma cells to obtain 15 consecutive FD curves in static mode at 30 second intervals. Bright field images were taken using a charged-coupled device camera before and after the compression to observe any variations in the cell morphology that would indicate impairment.

#### 2.3.2.3 Data analysis

Three Hertz derived contact mechanics models were used to analyse the FD curves; sphere on a plane, sphere on a sphere, and sphere on a cylinder model. These three models were selected as reasonable approximations of the tip and sample geometries. Note that one often observes adhesion in biological systems, nevertheless, the Hertz model is the most commonly used model in literature and will, thus, be utilised here.

Utilising Hertzian contact mechanics models as suggested and derived by Puttock and Thwaite [Puttock and Thwaite, 1969], the equation for the sphere on a plane model can be expressed by,

$$F_{cell=p} = \frac{(2\delta_{BeadOnAPlane})^{\frac{3}{2}}}{3\left(\frac{1-\sigma_{bead}^2}{E_{bead}} + \frac{1-\sigma_{cell}^2}{E_{cell}}\right)\left(\frac{1}{D_{bead}}\right)^{\frac{1}{2}}} \tag{2.4}$$

where $F_{cell=p}$ is the total compression force applied onto the cell, $\delta_{BeadOnAPlane}$ is the total deformation of the bead on a flat surface, $\sigma_{bead}$ is the Poisson's ratio of the bead, $\sigma_{cell}$ is the Poisson's ratio of the cell, $E_{bead}$ is the elastic modulus of the bead, $E_{cell}$ is the elastic modulus of the cell, and $D_{bead}$ is the diameter of the bead. Full derivation for the sphere on a plane model can be found in Supplementary Material S2. Similarly, the sphere on a sphere model is given by,

$$F_{cell=s} = \frac{(2\delta_{BeadOnASphere})^{\frac{3}{2}}}{3\left(\frac{1-\sigma_{bead}^2}{E_{bead}} + \frac{1-\sigma_{cell}^2}{E_{cell}}\right)\left(\frac{1}{D_{bead}} + \frac{1}{D_{cell}}\right)^{\frac{1}{2}}} \tag{2.5}$$

where $F_{cell=s}$ is the total compression force applied onto the cell, $\delta_{BeadOnASphere}$ is the total deformation of the bead on a spherical substrate, and $D_{cell}$ is the diameter of the cell. Full derivation for the sphere on a sphere model can be found in Supplementary Material S1. Finally, the sphere on a cylinder model is given by,

$$F_{cell=c} = \frac{\delta^{\frac{3}{2}}_{BeadOnACylinder}\left(D_{bead} \cdot -\frac{1}{e}\frac{dE}{de}\right)^{\frac{1}{2}}}{\frac{3K^{\frac{3}{2}}}{2\pi}\left(\frac{1-\sigma^2_{bead}}{E_{bead}} + \frac{1-\sigma^2_{cell}}{E_{cell}}\right)} \tag{2.6}$$

where $F_{cell=c}$ is the total compression force applied onto the cell, $\delta_{BeadOnACylinder}$ is the total deformation of the bead on a cylindrical substrate, $e$ is the eccentricity of the ellipse of contact, $K$ is the complete elliptic integral of the first class with modulus $e$, and $-\frac{1}{e}\frac{dE}{de}$ is the complete elliptic integral of the second class with modulus $e$. Full derivation for the sphere on a cylinder model can be found in Supplementary Material S3.

The elastic modulus values were estimated by fitting the three Hertz contact mechanics models to the FD curves at a fraction of 10% of the cell height (Figure 2–6 (a)). The force equation to be fit is as follows,

$$F_{cells=x} = \delta_i^{\frac{3}{2}} M_x \tag{2.7}$$

where the subscript $x$ denotes the geometry of the cell in contact (i.e. $p$ for plane, $s$ for sphere, $c$ for cylinder), $M_x$ is the slope of the fit, $\delta_i$ represents the total deformation of the bead on the cell, and the subscript $i$ denotes the equation of the Hertz model used (i.e. Equation 2.4: sphere on a plane model, Equation 2.5: sphere on a sphere model, Equation 2.6: sphere on a cylinder model).

All the curve-fittings were performed using nonlinear least squares regression method in MATLAB (Mathworks, MA) (Figure 2–6 (b)). Statistical differences for the results obtained were tested using a paired Student's t-test. The results were accepted as significant if $p < 0.05$.

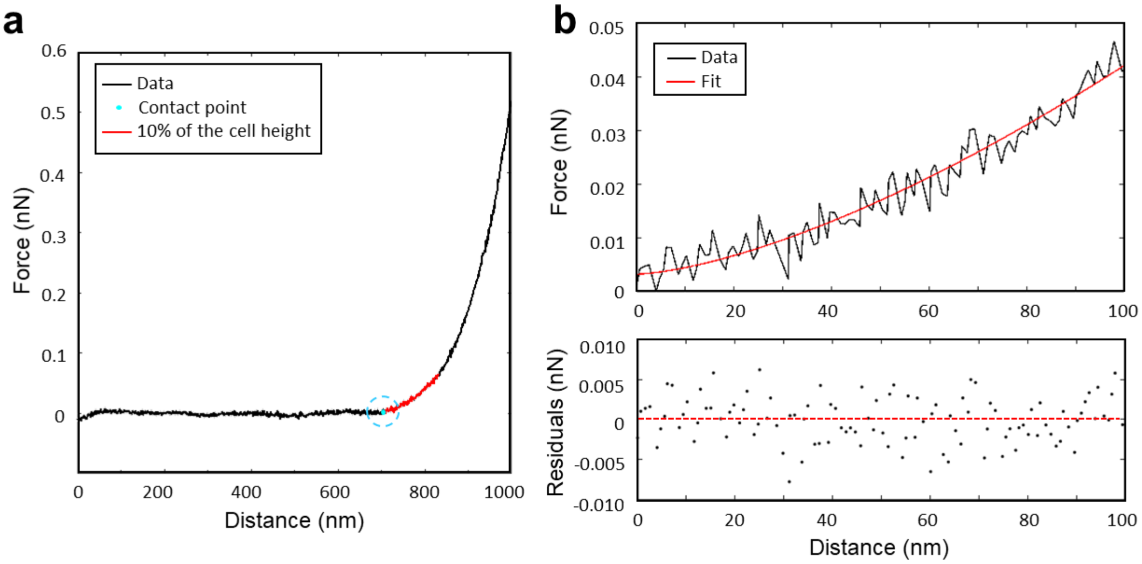

Figure 2–6: **Force-distance curve fitting.** The figure shows an extension curve taken from the indentation on the axon of a rat DRG neuron. **a.** The portion, equivalent to 10% of the cell height (red), is used for the curve-fitting procedure. The contact point (blue) is the point at which the FD curves begins to increase. **b.** Selected region of the FD curve is fitted using nonlinear least squares regression to Equation 2.7. The residual plotted shows the goodness of fit.

#### 2.3.2.4 Results and discussion

**Selection of the contact mechanics model to determine the elastic modulus of the cell**

Height profiles of the U87 glioma cells (Figure 2–7(a)) and fixed rat DRG neurons (Figure 2–7(b)) were used to determine the closest geometric approximation of the cell at the point of contact. From the topography images, the cell heights were determined to be $5\mu m$ for U87 glioma cells and $1\mu m$ for the axons of the DRG neurons. Additionally, the AFM height traces were an indication that the cell is not planar at the point of contact. Figure 2–7(c) is a schematic representation of a beaded AFM cantilever indenting the top of the cell body of a U87 glioma cell. Based on the AFM height trace, the cell body can be approximated as a sphere, thus the sphere on a sphere contact mechanics model (Figure 2–7(f)) would be the preferred model to extract the elastic modulus. Similarly, Figure 2–7(d) is a schematic representation of a beaded AFM cantilever compressing the top of an axon, which can be approximated as a cylinder. The sphere on a cylinder model (Figure 2–7(g)) would be the preferred model to determine the elastic modulus of the axon, in this case. In the event that the region of indentation is planar, for instance at the periphery of a cardiomyocyte [Domke et al., 1999], the schematic representation is shown in Figure 2–7(e) and the corresponding sphere on a plane contact mechanics model in Figure 2–7(h).

**Measuring the elastic modulus of cells**

Recalling the classic Hertz model assumptions, the indentation of the tip and sample are assumed to be within the linear elastic regime of the sample and the empirical rule of thumb is to analyse the indentation equivalent to 10% of the cell height. To confirm if this rule extends to different cell geometries (eg. spherical cell body and cylindrical axon), the FD-curves were analysed for deformations from 1% to $\approx$ 20% of the cell height. For all the FD-curve analysis, the contact point was defined as the point where the extension curve starts increasing (Figure 2–6(a), blue point). Fractions of the FD-curve were fitted to the three contact mechanic models (Equations 2.4, 2.5, 2.6) to evaluate the elastic modulus, and the results are shown in Figure 2–8. The indentation fraction between 9% and 11% of the cell height (Figure

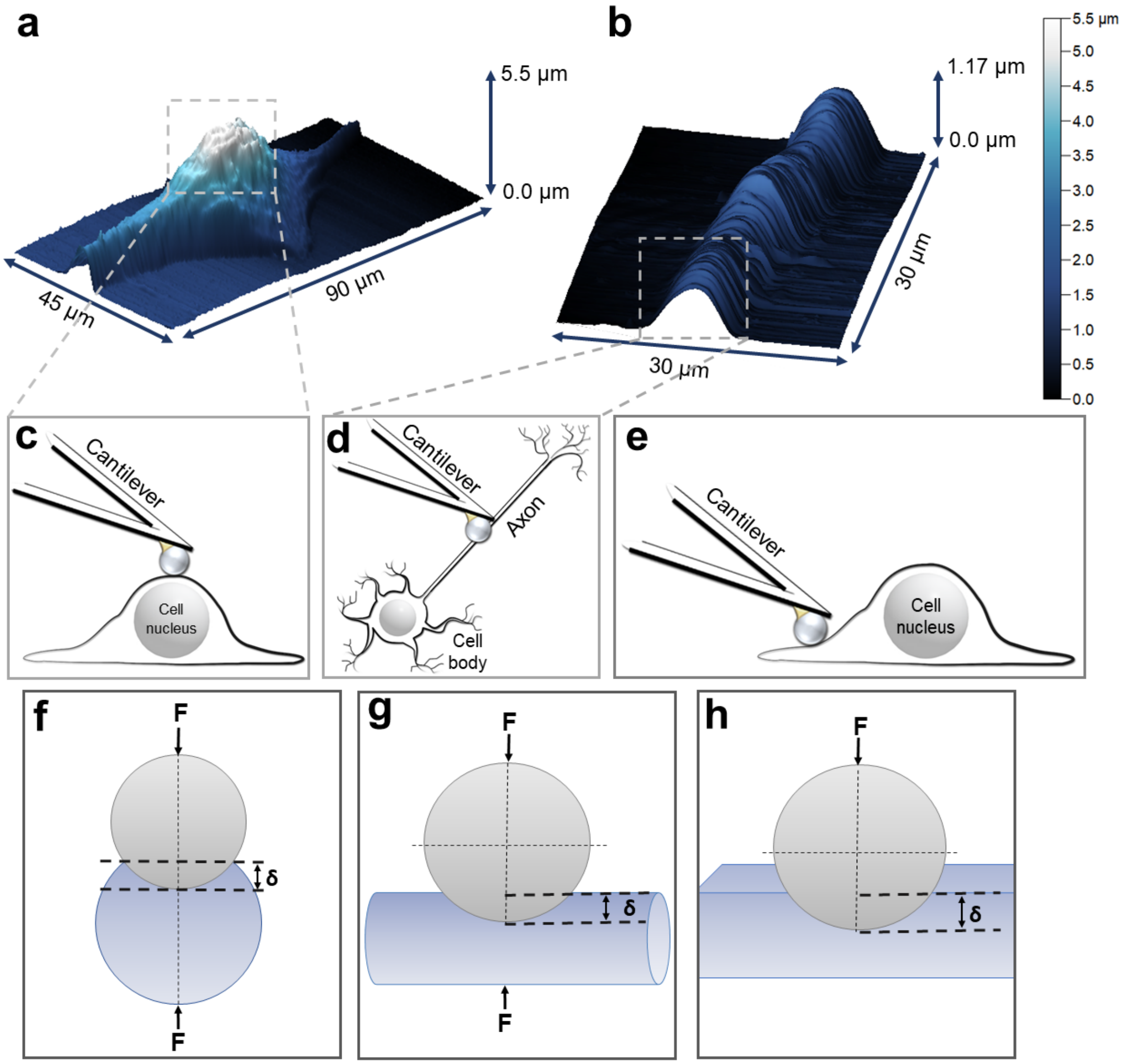

Figure 2–7: **AFM height topography and schematic diagrams of the Hertz contact mechanics models. a.** Height trace of a U87 glioma cell. **b.** Height trace of a rat DRG axon. **c.** Side view representation of a beaded cantilever compressing the cell body, which can be approximated to be a sphere. **d.** Top view of a beaded cantilever compressing the axon of a neuron, which can be approximated as a cylinder. **e.** Side view representation of a beaded cantilever compressing the periphery of a cell body, which can be approximated to be a flat plane. **f - h.** Schematic representations of the contact mechanics models that were used to determine the elastic modulus of cells. In all three representations, $F$ represents the total applied force and $\delta$ represents the total elastic compression at the point of contact between the tip and the sample. **f.** Model for a sphere in contact with a sphere. **g.** Model for a sphere in contact with a cylinder. **h.** Model for a sphere in contact with a plane.

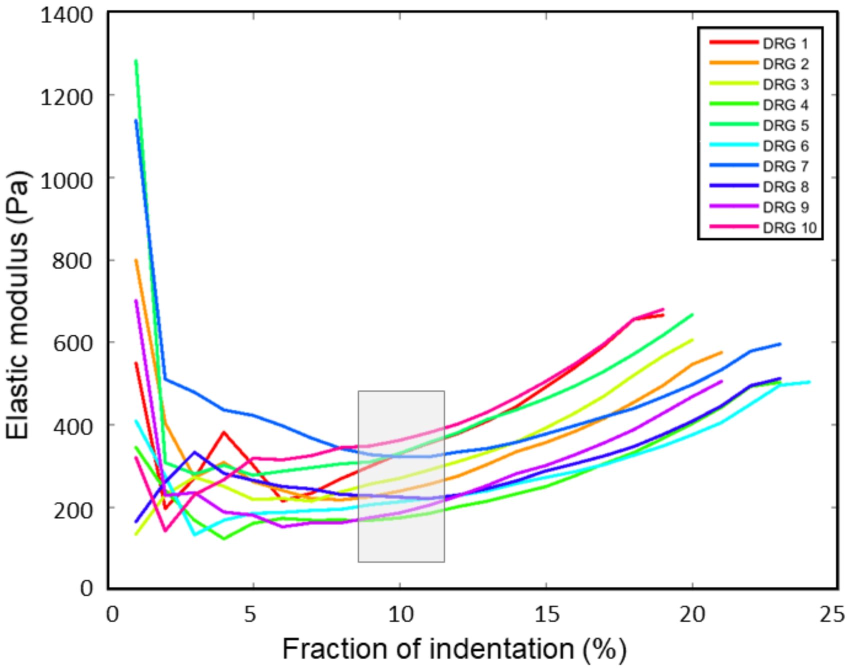

Figure 2–8: **Elastic modulus values as a function of fraction of indentation.** Ten FD-curves from rat DRG neurons were fitted to the sphere on a plane model (Equation 2.4) at indentation depths ranging from 1% to ≈ 20% of the cell height. The results show great variability in the first 1% to 7% fraction of indentation, and an increase in values at indentation depths above 10%. Elastic modulus values in the shaded region (9% to 11% of the cell height) are consistent as this region corresponds to the linear elastic regime of the tip and the sample.

2–8, shaded region) presented the best fit ($R^2 > 0.95$), as assessed by $R^2$ values. This region is in agreement with the classic Hertz model and can be applied to both cell geometries used in the present study. However, large variations were present in the 1% to 7% region, and the reason for this occurence is unknown. Moreover, the elastic modulus values were seen to increase steadily at indentations past 10%, consistent with findings reported by Magdesian et al. [Magdesian et al., 2012]. Her study found that the depth-dependent increase in elastic modulus values was a reflection of an increase in axonal stiffness due to cytoskeletal resistance. This section emphasises the importance of being in the linear elastic regime to avoid over or underestimating the elastic modulus of the cell.

Next, the distribution of the elastic modulus values calculated for the two cell types were evaluated. Since the contact point selection and region of fit were identical for the FD-curves, not surprisingly, the spread of values were identical (Figure 2–9(a)) and differing only by a constant corresponding to the contact mechanic model used (full derivations of the elastic modulus equations can be found in Supplementary Material S1, S2, S3). A summary of the elastic modulus values obtained for both U87 glioma cells and rat DRG neurons can be found in Figure 2–9(b). In both cases, there is an observable increase in the calculated elastic modulus, where $E_{cell=p} < E_{cell=c} < E_{cell=s}$. In order to understand this increasing trend, a Taylor series expansion with respect to the ratio of $\left(\frac{D_{bead}}{D_{cell}}\right)$ were calculated for the elastic modulus equations ($E_{cell=x}$). The elastic modulus of a sphere on a sphere ($E_{cell=s}$) and that of a sphere on a cylinder ($E_{cell=c}$) can be expressed in terms of the elastic modulus of a sphere on a plane ($E_{cell=p}$), as follows:

Sphere on a sphere model approximation,

$$E_{cell=s} \approx E_{cell=p} + E^2_{cell=p} \cdot \frac{(2D_{bead})^{\frac{1}{2}}}{3M\left(1-\sigma^2_{cell}\right)} \left(\frac{D_{bead}}{D_{cell}}\right) + \theta \left(\frac{D_{bead}}{D_{cell}}\right)^2 \tag{2.8}$$

Sphere on a cylinder model approximation,

$$E_{cell=c} \approx E_{cell=p} + E^2_{cell=p} \cdot \frac{\left(\frac{D_{bead}}{2}\right)^{\frac{1}{2}}}{3M\left(1-\sigma^2_{cell}\right)} \left(\frac{D_{bead}}{D_{cell}}\right) + \theta \left(\frac{D_{bead}}{D_{cell}}\right)^2 \tag{2.9}$$

The different sample geometries lead to correction terms that, to first order, are a function of the tip and sample geometric parameters and constants. In the limit that $\frac{D_{bead}}{D_{cell}} \ll 1$, the correction terms become negligible and the above models are reduced to that of a sphere on a plane, as expected. In typical indentation experiments, the ratio $\frac{D_{bead}}{D_{cell}}$ is larger than 1. For this work, the ratios are $\frac{D_{bead}}{D_{neuron}} \approx 20$ and $\frac{D_{bead}}{D_{glioma}} \approx 4$, thus, the correction terms are non-negligible. To reinstate, to first order approximation, the contact mechanics models predict an increase in the elastic modulus values such that $E_{cell=p} < E_{cell=c} < E_{cell=s}$, as shown in the results of Figure 2–9(b).

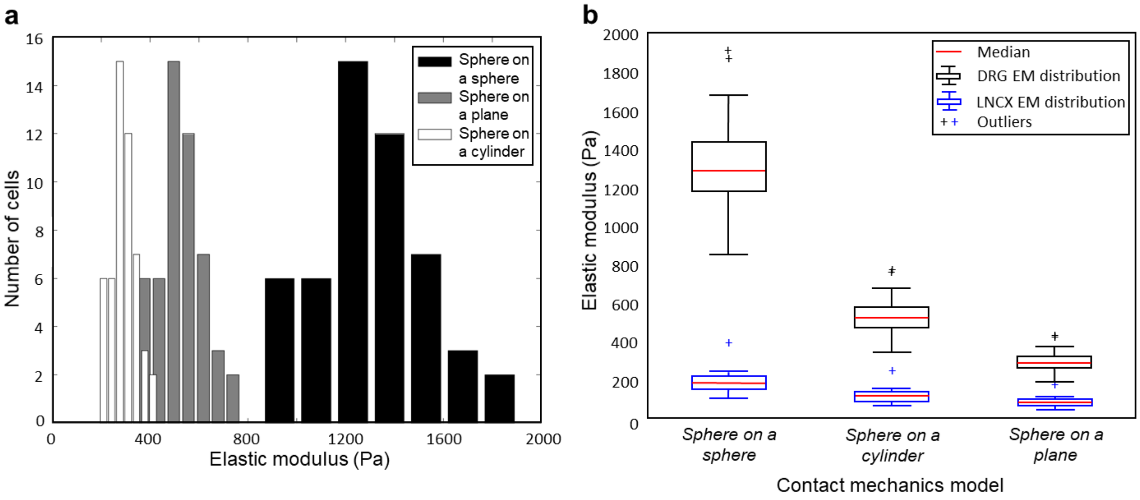

Figure 2–9: **Histogram and box plot of elastic modulus values. a.** Histograms of elastic modulus values for the three contact mechanics models fitted to FD-curves of rat DRG neurons. The spread of the three distributions are identical with differing values of mean and standard deviation. **b.** Box plot of elastic modulus values obtained for the rat DRG neurons ($n = 51$) and U87 glioma cells ($n = 17$). The top and bottom of the box plots represent the $25^{th}$ and $75^{th}$ percentiles of the distribution, the red line represents the median, and + above the box plots are outliers in the data.

## Discussion

The mechanical properties of biological samples, such as the elastic modulus provide insights into the internal structure, dynamics and biochemical processes of cells [Ingber, 1997, Charras and Horton, 2002, Lamontagne et al., 2008, Iyer et al., 2009, Roduit et al., 2009]. However, a wide range of elastic modulus values are reported in the literature for the same cell type, as shown in Figure 2–10 [Mustata et al., 2010, Bernick et al., 2011, Spedden et al., 2012b, Spedden and Staii, 2013]. Multiple factors can lead to this variability and can be attributed to either of biological origin or due to differences in details of the experimental methods used. One factor, in particular, is the option of utilising different methods and models to extract the elastic modulus of cells from FD-curves. While some contact mechanics models incorporate adhesive forces, all the models require starting assumptions on the relative geometry of the indenter and sample. Although, the often implicitly made assumption is that the region of indentation in the sample is homogenous and planar, the AFM topography images reveal otherwise (Figure 2–7). As a consequence, comparing the elastic modulus values for the same cell type (for instance, in studying cellular properties during different stages of development, division, or disease), might still be challenging especially when the shape of the cells are not identical.

In this work, the significance of cellular geometry in determining the elastic modulus using a simple Hertz model analysis was evaluated, and the results emphasise the importance of accurately modelling the cell morphology at the point of contact, in order to obtain an accurate estimation of the elastic modulus. Results of this investigation prove that the elastic modulus values obtained do differ significantly when a different cell geometry is used for the contact mechanics model. For instance, when the DRG neurons and U87 glioma cells were modelled as spheres, the elastic modulus values obtained were significantly higher than when the cells were modelled as a plane or cylinder. And, this is a consequence of geometrical correction terms in the Hertz contact mechanics models. As previously derived, these correction terms become negligible in the limit that $\frac{D_{tip}}{D_{cell}} \ll 1$, resulting in the contact mechanics models being reduced to an indenter on a plane model. In other words, the shape of the cell may be approximated as planar if the tip in contact is significantly smaller than the cell, as in the case of a sharp AFM tip. However, sharp AFM tips are not generally used for probing biological samples as there is a high risk of piercing the membrane of the cell being studied.

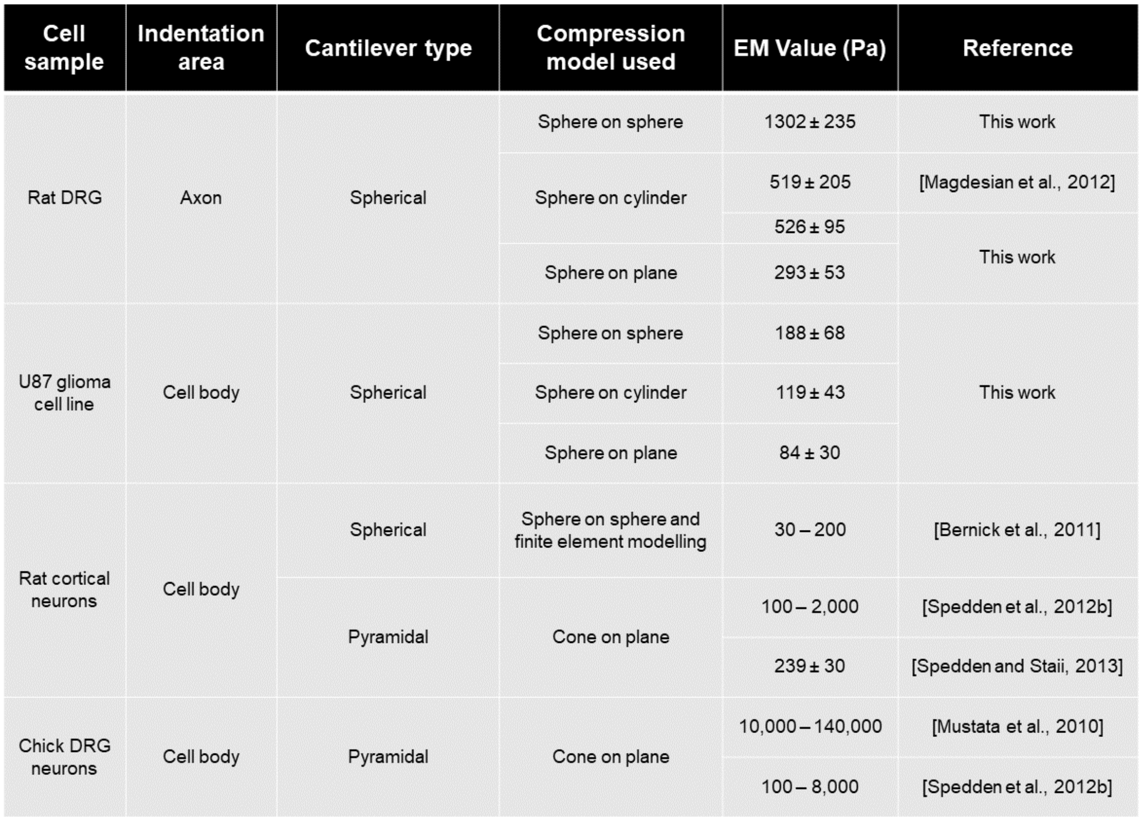

| Cell sample | Indentation area | Cantilever type | Compression model used | EM Value (Pa) | Reference |
|---|---|---|---|---|---|
| Rat DRG | Axon | Spherical | Sphere on sphere | 1302 ± 235 | This work |
| | | | Sphere on cylinder | 519 ± 205 | [Magdesian et al., 2012] |
| | | | | 526 ± 95 | This work |
| | | | Sphere on plane | 293 ± 53 | |
| U87 glioma cell line | Cell body | Spherical | Sphere on sphere | 188 ± 68 | This work |
| | | | Sphere on cylinder | 119 ± 43 | |
| | | | Sphere on plane | 84 ± 30 | |
| Rat cortical neurons | Cell body | Spherical | Sphere on sphere and finite element modelling | 30 – 200 | [Bernick et al., 2011] |
| | | Pyramidal | Cone on plane | 100 – 2,000 | [Spedden et al., 2012b] |
| | | | | 239 ± 30 | [Spedden and Staii, 2013] |
| Chick DRG neurons | Cell body | Pyramidal | Cone on plane | 10,000 – 140,000 | [Mustata et al., 2010] |
| | | | | 100 – 8,000 | [Spedden et al., 2012b] |

Figure 2–10: **Summary of reported elastic modulus values of AFM measurements on various biological samples.** The differences in elastic modulus values can be observed from the area of indentation, geometry of the cantilever tip, and the compression model used.

While the estimation of elastic modulus through fitting of a contact mechanics model to a FD-curve seems simple, this method is actually not trivial. As shown in this section, the quantitative values of elastic modulus depend strongly on the geometry of the cell modelled in the contact mechanics model used. Ideally, one would combine finite element modelling with AFM techniques, as seen in [Bernick et al., 2011], to accurately represent the cell morphology at the point of contact. Finally, comparison of absolute elastic modulus values across the literature needs to be done with care, as these values depend on a list of factors and parameters that would otherwise provide an inaccurate estimate of the elastic modulus value of the cell.

## 2.4 Conclusion

The knowledge of the elastic modulus of a cell is crucial to understanding the underlying properties and mechanisms that maintain a cell's shape, and assist in cellular processes such as cell proliferation, migration, and differentiation. In this chapter, the findings demonstrate how the accuracy and thus reliability of elastic modulus values extracted from an analysis of contact mechanics is strongly affected by assumptions of the sample geometry. The three compression models used to extract the elastic modulus values of biological samples differ significantly for the same set of FD curves obtained through the same AFM indentation methods. Therefore, accurate determination of elastic modulus of cells is not as straightforward as it seems.

# CHAPTER 3

# RECORDINGS OF CELLULAR SIGNALS

## 3.1 Introduction to electrogenic cells

Electrogenic cells are cells that are able to generate electrical activity through transient depolarisation of the cellular membrane. Neurons, cardiomyocytes, and photoreceptors are examples of cells that, when triggered either externally (by an external stimuli or by another cell) or internally (through spontaneous cellular processes), exhibit electrogenic properties. Coordinated electrical activity between these cells is thought to be the basis of complex information processing in the brain as well as for proper functioning of spontaneous physiological processes in the body. Recording and decoding electrical activity from electrogenic cells provides a means of understanding the communication and synchronisation of activity between cells [Franks, 2005, Heer, 2005, Hierlemann et al., 2011].

### 3.1.1 Neurons

#### The nervous system

The brain is a highly complex organ which oversees a wide range of function in the body, such as decision-making, emotion regulation, voluntary movements, and basic involuntary motions of the body. There are over $10^{11}$ nerve cells, i.e. the fundamental units of the nervous system. These nerve cells can be classified into three types; sensory neurons, motor neurons, and interneurons. Sensory neurons receive external stimuli from the environment, motor neurons send signals that control the movement of muscle cells, and interneurons are involved in communication between other neurons. While the underlying morphology of neurons are similar for the three types of neurons, the complexity of the brain lies in the way these neurons connect and form intricate circuits with each other [Johnston and Wu, 1995, Kandel et al., 2000, Heer, 2005, Mishra and Majhi, 2019].

The nervous system also contains glial cells that grow in the spaces surrounding neurons. Albeit not being directly involved in neuronal signalling, glial cells provide structural support by surrounding neurons in the CNS of vertebrates. Oligodendrocytes and Schwann cells, two specific types of glial cells, are involved in the production of the myelin sheath that insulates axons of neurons. Astrocytes form the blood-brain barrier that inhibits harmful substances from entering the brain, and radial glial cells are involved in axonal guidance and growth. Other roles of these non-neuronal cells include releasing growth factors that help neurons thrive, regulating properties of the presynaptic terminal, removing excess neurotransmitters during synaptic transmission, and getting rid of waste following a neuronal injury or death [Kandel et al., 2000].

Neurons, the fundamental signalling units of the nervous system, have four primary regions: the dendrites, the cell body, the axon, and the presynaptic terminals, as shown in Figure 3–1 (a). Dendrites are filament like extensions that protrude from the cell body to receive incoming signals (excitatory or inhibitory) from other neurons. These incoming signals are converted into electrical signals and transmitted to the cell body. In the CNS, the dendrites are long and branch out extensively to form connections with other neurons in the brain. Signals from dendrites are directed to the cell body and integrated. If the incoming signals induce a large enough change in intracellular potential, an action potential will be generated. The cell body also houses the cell nucleus and functions as the metabolic centre of the neuron. Here, genetic information is stored, proteins are synthesised, and another type of extension extends away from the cell body (i.e. the axon). The axon is often a single filament which extends and branches, as far as 1 metre in length, away from the cell body to its target locations. Axons come in two varieties, myelinated and unmyelinated. Myelinated axons are insulated by myelin sheaths, which are generated by Schwann cells in the peripheral nervous system and oligodendrocytes in the CNS. The myelin sheaths serve as electrical insulators to increase the efficacy of action potential (AP) propagation. The formation of myelin sheaths are restricted periodically along the axon by nodes of Ranvier, where the AP is regenerated at an increased rate. This rapid and energy efficient process of AP propagation in myelinated axons is called saltatory conduction, and results in a significant increase in the speed of AP propagation when compared to that of unmyelinated axons. At the distal end of the axon, presynaptic terminals transmit information to other neurons or target cells [Johnston and Wu, 1995, Kandel et al., 2000, Heer, 2005, Debanne et al., 2011, Mishra and Majhi, 2019, Suminaite et al., 2019].

### Neuronal signalling

Neurons transmit information to each other through chemical or electrical synapses. During chemical synapses, the action potential causes neurotransmitters to be released from the axon terminal of the presynaptic neuron to receptors on dendrites of the postsynaptic neuron. During electrical synapses, transmission of electrical signals flows directly from the presynaptic neuron to postsynaptic neuron through gap junctions. These neuronal signals are generated by rapid changes of the membrane potential difference, which are mediated by ion channels. The ion channels are ion specific and respond at high rates to certain chemical, electrical, or mechanical cues [Kandel et al., 2000, Heer, 2005].

The types of ion channels present and the relative concentration gradients of ions determine the membrane potential and electrical activity of neurons. At rest, a charge separation is maintained across the intracellular and extracellular membrane of the cell, resulting in the resting membrane potential (Figure 3–1 (b)). The unequal distribution of charges is maintained by selectively permeable membrane proteins while the concentration gradients are produced and maintained by the $Na - K$ pumps. Therefore, resulting in a net positive charge on the extracellular membrane and a net negative charge on the intracellular membrane. Setting the extracellular potential as $0V$, the resting membrane potential difference of neurons are typically in the range of $-40mV$ to $-80mV$. During an AP, the opening and closing of ion channels result in rapid changes in the membrane potential. An illustration of the classic AP waveform is shown in (Figure 3–1 (c)). For most neurons, the

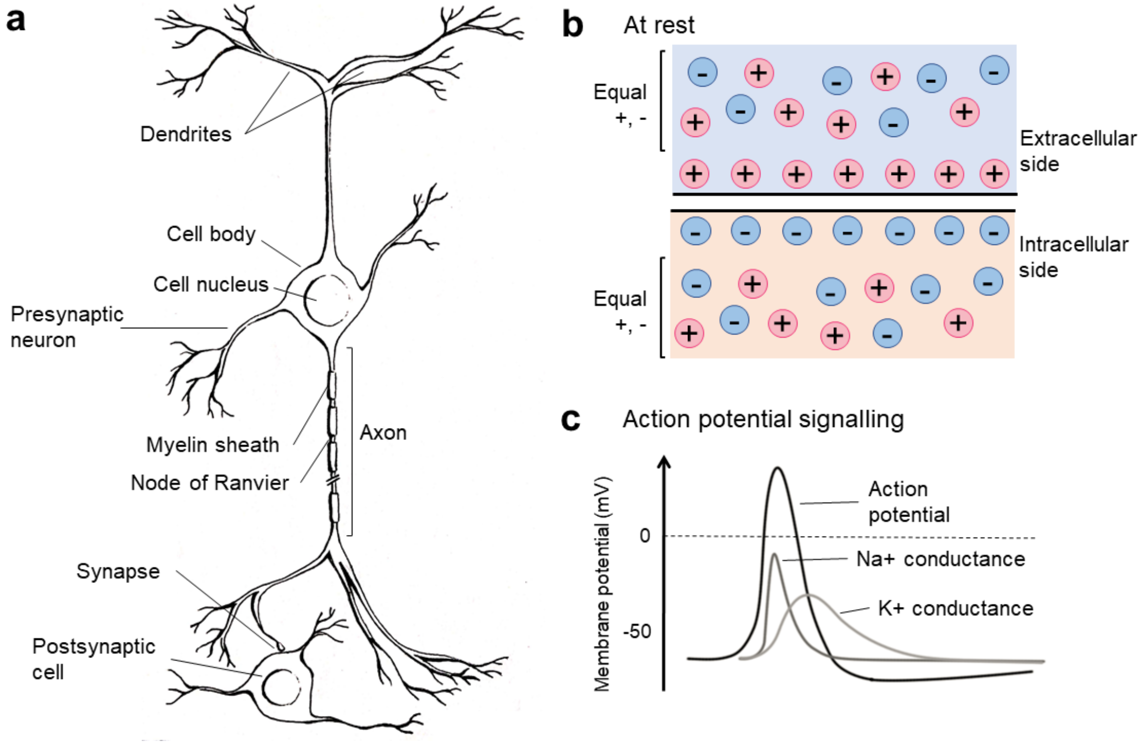

Figure 3–1: **Structure of the neuron, the membrane potential, and the action potential. a.** Illustration of a myelinated neuron making synaptic contact with a postsynaptic cell. The cell body contains the nucleus, which stores genetic information. From the cell body, two types of extensions are formed: dendrites which receive incoming signals from other cells and axons which transmit neuronal signals to other neurons or receiving cells. Myelinated axons contain layers of myelin, which insulate the axon, and unmyelinated sections called nodes of Ranvier. Neuronal signals are transmitted fron the postsynaptic neuron to the postsynaptic cell via synapses. **b.** Illustration of the charge separation at the neuron membrane. At rest, there is a different distribution of positively and negatively charged ions on the surface of the intracellular and extracellular membranes. This inequality in membrane charges gives rise to the resting membrane potential. **c.** Illustration of an action potential. The shape of the action potential is determined by the changes in conductance of $Na^+$ and $K^+$ ions. At the start of the action potential, there is an influx of $Na^+$ ions into the cell. Following that, the cell is further repolarised by $K^+$ ions flowing out of the cell. All of the illustrations were recreated based on figures in [Kandel et al., 2000].

depolarisation of the cell membrane is, firstly, caused by an influx of $Na^+$ ions into the cell. The membrane is further depolarised by a flow of $K^+$ ions out of the cell following the activation of voltage-gated $K^+$ ionic channels. Subsequently, the membrane undergoes a refractory period, whereby another AP would not be triggered during this moment [Hodgkin and Huxley, 1952, Kandel et al., 2000, Debanne et al., 2011, Carter and Shieh, 2015, Mishra and Majhi, 2019].

### 3.1.2 Cardiomyocytes

The cardiovascular system contains specialised muscle cells that coordinate electrical signals to produce rhythmic contractions of the heart. Similar to neurons, these cardiac cells are electrogenic and are able to produce rapid changes in their membrane potential to generate an AP. The electrical activity of cardiomyocytes are determined by the ion channels and relative ionic concentrations across the cell membrane. There are five phases that describe the waveforms of the cardiomyocytes and cardiac pacemaker cells, shown in Figure 3–2. Starting with Phase 4, the resting membrane potential of cardiomyocytes sits at approximately $-85mV$. Phase 0 represents the upstroke of the AP, bringing the membrane potential up to approximately $+50mV$. During this phase, the cell enters an absolute refractory period where no stimulus is able to induce another AP. Following that, the AP enters Phase 1, a rapid repolarisation phase, and subsequently Phase 2, the plateau phase. Lastly, the cell undergoes another phase of rapid repolarisation, Phase 3, whereby the membrane potential is restored to its resting potential [Zaza, 2000, Grant, 2009, Oudit and Backx, 2018].

## 3.2 Electrophysiology recording techniques

As we have learnt from the previous section, action potentials are an all-or-nothing event, whereby a certain threshold has to be met before a signal can be produced. Thus, the amplitude and duration of the APs generated are similar along the length of the axon or amongst similar cardiac cells. *How, then, is information encoded to relay different messages?* In the case of neurons, information is encrypted in the number and frequency of firing of APs. Due to the complexity of such signals, an assortment of experimental tools have been developed to observe, record, and analyse cardiac and neuronal signals in order to understand the fundamentals of information processing, cellular communication, and network formation [Hodgkin and Huxley,

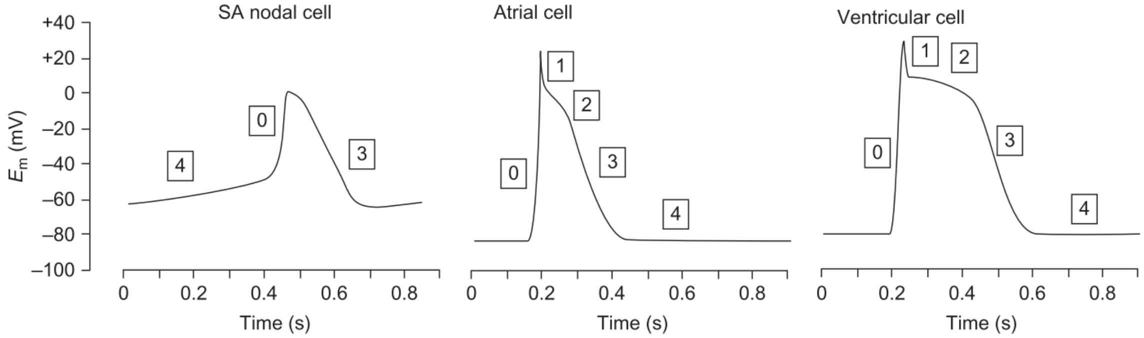

Figure 3–2: **Cardiac action potentials.** Illustrations of action potentials in sinoatrial nodal cells, atrial muscle cells, and ventricular muscle cells. Phases 4, 0, 1, 2, 3 represent the resting membrane potential, upstroke of the action potential, rapid repolarisation, plateau, rapid repolarisation phases respectively. Sinoatrial nodal cells lack phases 1 and 2, as the membrane potential is unstable and depolarises spontaneously back to $-50mV$. This figure was obtained with permission from *The cardiac action potential by A. Zaza, 2006, An Introduction to Cardiac Electrophysiology, pages 59–82, Copyright © 2012, Elsevier.*

1952, Kandel et al., 2000, Debanne et al., 2011, Obien et al., 2015, Mishra and Majhi, 2019].

Electrophysiology is a division of neuroscience, focused on studying the electrical activity of biological cells and tissues. The idea of bio-electricity in animals was first introduced over two centuries ago. Since then, various electrophysiological techniques have been developed and improved upon, and are the preferred methodology for investigating cellular activity today. Electrophysiology recording techniques can be divided into two main branches, intracellular recording and extracellular recording, based on the type of recording instrument, type of recording electrode, and placement of electrode on the cell. Each of these groups of techniques have enabled the recording and study of the electrical properties of cells both in vitro and in vivo [Lechasseur et al., 2011, Wickenden, 2014, Carter and Shieh, 2015, Obien et al., 2015].

### 3.2.1 Intracellular recording techniques

As the name suggests, intracellular recording techniques involve taking measurements from the interior of the cell, as shown in Figure 3–3. This branch of technique involves impaling the cell of interest to measure the membrane potential, by taking the potential difference of the tip of the intracellular electrode and the reference electrode. Thus, local membrane potential changes caused by synaptic activity can be measured on the order of millivolts ($mV$). Intracellular techniques were used to determine the ionic basis of the membrane potential in squid giant axons, a study that earned Alan Hodgkin and Andrew Huxley the 1963 Nobel Price in Physiology or Medicine. Since then, researchers have been able to investigate the effects that drugs, neurotransmitters, and neuromodulators have on the local membrane potential and action potentials of cells [Hodgkin and Huxley, 1952, Wickenden, 2014, Carter and Shieh, 2015]. For the purpose of this thesis, only the sharp microelectrode technique and patch clamp recording technique will be discussed.

#### 3.2.1.1 Sharp microelectrode technique

Intracellular 'sharp' microelectrode recording technique was developed and introduced in the 1950s to observe the potential difference across the cell membrane. Microelectrode pipettes are formed by pulling a glass tube, using a pipette puller, to form a glass rod with a thin and tapered tip. Formation of the microelectrode pipettes are crucial as the type of glass used, diameter of tip opening, amount of taper at the tip, and the type of solution used to back-fill the electrode impact the quality of recordings obtained. The microelectrode pipettes are typically adjusted from cell to cell, in order to minimise the damage done when impaling the cell. The microelectrode pipettes have the ability to pass current through the microelectrode while recording the membrane potential simultaneously. Utilising a Wheatstone bridge circuit, the potential drop across the microelectrode resistance can be balanced out to isolate the signals originating from the cell membrane, also termed as bridge-balancing. Bridge-balancing provides the user with a direct measure of the resistance across the microelectrode pipette, which is also used as an indication of the quality of the tip of the recording pipette, i.e. the size of the pipette tip, indication of blockages due to air bubbles, or if the tip has been broken or not. Lack of or improper bridge-balancing results in inaccuracies in the values of the signals obtained [Parkington and Coleman, 2012].

There are several benefits to using the sharp microelectrode technique. Firstly, this technique can be applied while the cell being probed remains connected to neighbouring cells or the extracellular matrix, therefore, allowing electrical communication between cells to be studied. Next, enzymes are not required to 'clean' the surface of the plasma membrane to facilitate cell impalement with the pipette tip, thus preserving the integrity of the cell. Due to the sharp tapered end of the microelectrode pipette, this technique is said to inflict minimal damage to the cell membrane and the cytoplasmic components in the cell, thus prolonging the lifespan of the cell for experimentation. That being said, the only caveat in the previous statement implies that the user is extremely skilled at performing this sharp microelectrode technique. Some downsides to this technique include introducing stress to the cell due to poking of the pipette tip, inaccuracies in the values of the recorded membrane potential, and leakage of ions from the microelectrode into the intracellular environment of the cell [Parkington and Coleman, 2012].

#### 3.2.1.2 Patch clamp recording technique

The most widely used intracellular electrode recording technique is the patch clamp recording method, a technique developed by Erwin Neher and Bert Sakmann which also earned them the 1991 Nobel Prize in Physiology or Medicine. Like the sharp microelectrode technique, patch clamp recording enables the user to measure intracellular signals of cells, with the added ability to measure ionic activity through patches of the cell membrane. Unlike sharp microelectrode pipettes, patch clamp pipettes have larger and blunt tips, which are important to form tight Gigaohm seals between the tip of the pipette and the cell membrane. There are four recording configurations in patch clamp recording, as illustrated in Figure 3–3 [Bannister and Langton, 2012, Wickenden, 2014]:

- **Whole-cell:** As the name implies, this configuration records signals from the entire cell. The membrane of the cell is initially ruptured to allow the pipette solution to be in contact with the intracellular environment of the cell. Careful considerations have to be made to ensure that the pipette solution is very similar to that of the interior of the cell to prevent ionic imbalances, contamination, dilution, or washout within the cell.

- **Cell-attached:** Cell-attached is one of the three isolated patch clamp configurations that allow the study of single ion channels. This is the least invasive and most stable of all four configurations as the membrane patch remains intact. However, the amount of modulations that can be made to the cell is limited as the internal environment of the cell is not directly accessible through the cell-attached configuration.

- **Inside-out:** The final two configurations are excised patch configurations where a piece of the cell membrane is broken off from the parent cell, performed simply by removing the electrode away from the cell after forming a Gigaohm seal in either cell-attached or whole-cell mode. In inside-out configuration, the intracellular side of the cell membrane is facing the recording chamber.

- **Outside-out:** In the outside-out configuration, the extracellular side of the membrane is facing the recording chamber instead. Excised patch configurations allow single ion channels on the cell membrane to be studied, however, these configurations disregard the rest of the cellular components that may play an important role in regulating the activity of membrane ion channels.

While both the sharp microelectrode and patch clamp recording techniques are similar in many ways, there are a few apparent differences which set them apart. Firstly, the large tip of the patch clamp pipette allows for more current flow and more control in voltage-clamp experiments, however, cytoplasmic constituents of the cell may be lost to the pipette environment. Secondly, APs recorded with sharp microelectrodes are attenuated compared with that of the patch clamp electrode, possibly due to the greater capacitance of the sharp microelectrodes. In both cases, however, there is a risk of damage when probing the cell with the pipettes. Hence, one has to exercise care and caution to minimise damage to the cell to, effectively, prolong the recording time of the experiment.

### 3.2.2 Extracellular recording techniques

In extracellular recording techniques, sensors or electrodes are placed very close to the surface of the cell to record changes in the membrane potential, as shown in

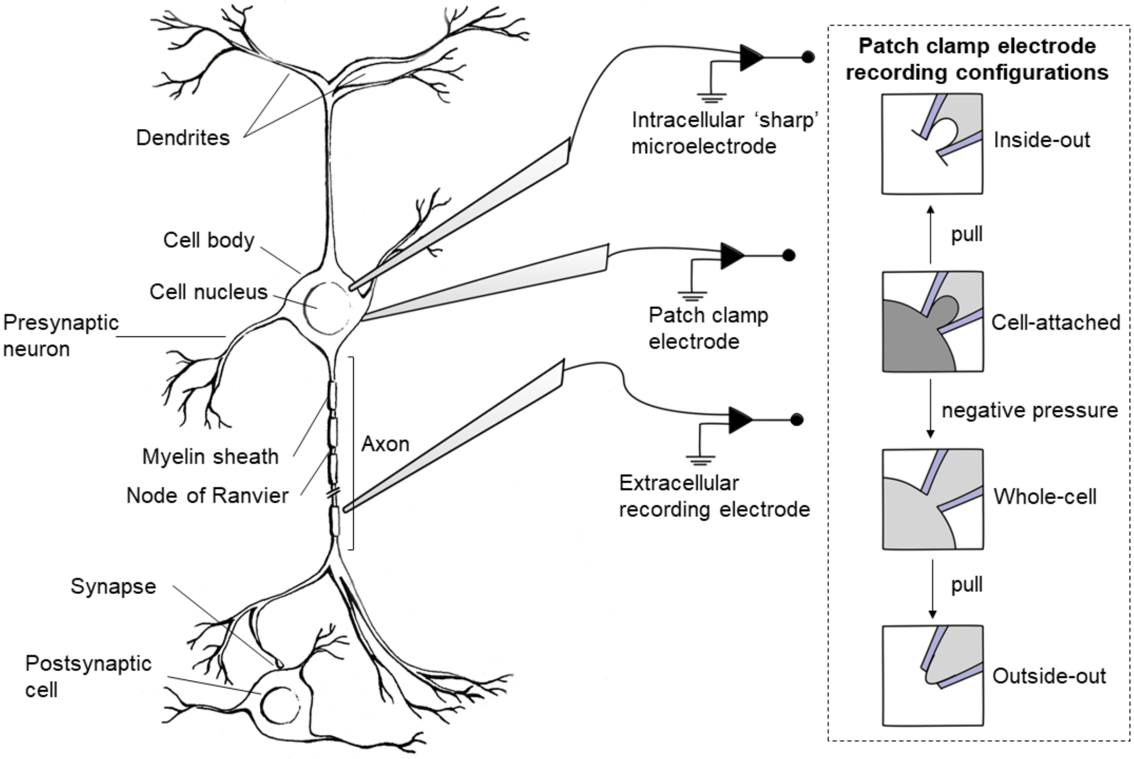

Figure 3–3: **Electrophysiology recording techniques.** The recording techniques are classified based on the position of the electrode on the cell. Sharp microelectrode recording (intracellular 'sharp' microelectrode) and patch clamp recording (patch clamp electrodes) techniques are examples of intracellular recording techniques. There are four different recording configurations for patch clamp recording technique: inside-out, cell-attached, whole-cell, and outside-out configurations. Extracellular recording electrodes are placed close to the cell and do not rupture the cell membrane. All of the illustrations were recreated based on figures in [Kandel et al., 2000, Wickenden, 2014, Carter and Shieh, 2015].

Figure 3–3. When APs are generated, there is a change in the membrane potential on the extracellular side due to the flow of ions across the membrane. The flow of ions also generates an electric field which directly influences the metal recording microelectrode. The main benefit of extracellular recording techniques is that extracellular probes are noninvasive, thus, one is able to maintain the integrity of cells to allow for long-term experiments. Additionally, some extracellular electrodes consist of multiple sensors, which enable signals to be measured from multiple sites of the same cell or across multiple cells simultaneously. Unlike intracellular recording techniques, extracellular recording techniques are easy to implement as precise handling and positioning of extracellular electrodes are not required for this method to work. The only requirement being that the extracellular electrode has to be in close enough in proximity to detect signals from the cell of interest. A downside to extracellular recording techniques would be the inability to measure subthreshold potential changes in the membrane (e.g. excitatory postsynaptic potentials or inhibitory postsynaptic potentials). Furthermore, depending on the density of the cell culture on the recording electrode, it may be difficult to discern the signals produced by a single neuron or by multiple neurons [Hierlemann et al., 2011, Carter and Shieh, 2015].

Extracellular recording techniques have been developed for multiple stages of the cellular organisation. For instance, spontaneous or evoked brain activity can be measured using methods such as functional magnetic resonance imaging, positron emission tomography, and electroencephalography. On a cellular or tissue level, microelectrode arrays (MEAs), developed through the integration of metal electrodes, open-gate field-effect transistors or oxide-semiconductor field-effect transistors, are used to measure local field potentials and extracellular APs from the cell samples. In some cases, on site stimulation electrodes are integrated in the MEA to allow for electrical stimulation of the cells. The development and advancement of extracellular recording techniques have enabled and facilitated the measurements of cellular signals in vivo and in vitro [Obien et al., 2015]. For the following section, the applications of complementary metal oxide semiconductor (CMOS) based high density MEAs (HDMEAs) to in vitro cellular experiments will be discussed.

#### 3.2.2.1 Microelectrode arrays

Microelectrode arrays (MEA) were first introduced in 1972 by Thomas et al. [Thomas et al., 1972] to measure signals from cultured chick DRG neurons. The microelectrodes developed consisted of 30 gold electrodes on glass, insulated with a photoresist, and electroplated with platinum (Pt) black to further reduce the impedance of the electrodes. The first measurements on cultured chick DRG neurons on the MEA were unsuccessful as there was a layer of glial cells which insulated the neurons from the microelectrodes. Nevertheless, Thomas et al. were later able to record signals from dissociated chick myocytes. Those recordings became the first cellular recording via MEA in history and has opened the door to the MEA technology that we have today. Since then, efforts have been made to improve and optimise the design of MEAs (e.g. increasing the number and density of electrodes, improving signal-to-noise ratio (SNR), increasing the reliability of spike sorting analysis, and including on-chip source localisation) for electrophysiological studies [Thomas et al., 1972, Pine, 2006, Obien et al., 2015]. The advancement of MEA is influenced by technological advancements in the semiconductor industry. For instance, silicon-based biosensors have developed to field-effect transistor based devices which encompass 2D arrays, and further to CMOS based devices which now have additional processing capabilities fabricated on-chip. An in-depth review of the evolution of MEA devices can be found in a review article by Obien et al. [Obien et al., 2015].

The capacity to incorporate thousands of microelectrodes on a single chip is one of the many benefits of using CMOS-based MEAs (CMOS-MEAs). Along with microelectrodes, amplifiers and filter units can also be integrated on-chip, to allow CMOS-MEAs to operate as an active array and to avoid complications arising from parasitic capacitance and attenuation of small signals. Having an active MEA circuitry allows for simultaneous stimulation and recording from multiple electrodes on the MEA, a process that would otherwise be impossible in conventional MEAs. Additionally, signals can be controlled and transmitted without the fear of mechanical and electrical influence or loss of information, with the help of on-chip analog-to-digital conversion (ADC) units. Altogether, CMOS-MEAs boasts many benefits. Ones in particular include efficient on-chip control and connectivity, improved signal quality, and practical usage through programmable and automated softwares which accompany these CMOS-MEAs. Lastly, through CMOS technology, the thousands of microelectrodes and on-chip circuitry can be integrated into a small area measuring approximately $20 - 40mm^2$, therefore, resulting in small and portable devices that can be adapted or used directly with other experimental equipment [Hierlemann et al., 2011, Obien et al., 2015, Müller et al., 2015].

CMOS based high density MEAs (CMOS-HDMEA) is a branch of MEAs which have high SNR and are able to record signals with high spatial and temporal resolutions. Increased spatial resolution is made possible by densely packing thousands of small microelectrodes, a feature which grants the experimenter the ability to record the dynamics of the an entire neuron with a fine level of detail. While the CMOS-HDMEA brings about multiple improvement to electrophysiology recording techniques, the advancement of the MEA technology does come at a cost. For instance, the reduction in the size of the microelectrodes and integration space to cram in all the electrodes and on-chip circuitry, inevitably results in an increase in thermal noise and other types of noise sources. Consequently, there exist a limit to the size and number of microelectrodes that can be integrated on-chip without sacrificing the quality of the signals recorded. In addition, the visibility of biological samples is greatly reduced due to the nature of the substrate used for fabrication. In general, CMOS-HDMEAs are fabricated on silicon, which is an opaque substrate. Moreover, additional preventive measures have to be taken to protect on-chip electronic components from corrosion and damage resulting from exposure to cellular media. On-chip stimulation procedures, such as high current or voltage pulses, could also add to the corrosion of the CMOS-HDMEA chips. For these reasons, utilising a packaging solution that is biologically compatible, electrically and thermally inert, and waterproof is crucial to protect the on-chip circuitry of the CMOS-HDMEA for the entirety of the experiments [Frey et al., 2009a, Hierlemann et al., 2011, Viswam et al., 2018].

### 3.2.3 Cellular activity recorded using CMOS-HDMEA

The following section serves as an introduction to the CMOS-HDMEA obtained in collaboration with the Department of Biosystems Science and Engineering of Eidgenössische Technische Hochschule (ETH) Zürich, Switzerland. This CMOS-HDMEA is involved with the formation of the integrated AFM and CMOS-HDMEA platform, which will be described in detail in the following chapter.

#### 3.2.3.1 Introduction

The usage of microelectrode arrays (MEAs) in neuroscience and biology related research has been increasing over the years due to the improvement of signals recorded, which are a direct result of technological advancements and the benefit of being non-invasive to biological samples. Depending on the design of the MEA and the nature of the experiment, there are three main methods of utilising the MEAs: constrain of the biological sample with respect to the position of the MEA, adaptation of the MEA to the biological sample, or culture of dissociated cells or tissue samples on the surface of the MEAs. The third option is the preferred methodology for preparing biological samples on CMOS-HDMEA devices. While dissociated cell cultures enable the study of isolated single cells, the natural location and connection of the cell with respect to its native environment are disrupted. Tissue cultures, on the other hand, preserve the relative composition of the biological sample but do not permit the isolation of signals from single cells [Frey et al., 2007, Frey et al., 2009b, Hierlemann et al., 2011].

MEAs play an important role in the field of neuroscience, where recorded signals are used in an attempt to understand neuronal communication, neuron growth, synaptic activity, or the effects of drugs on neurons. An example of such experiments include studying electrical signals from brain slices that were cultured on MEAs and introducing channel specific blockers to interrupt the activity of the brain slice [Obien et al., 2015]. In 2013, the process of neural network maturation was observed when Ito et al. used MEAs to measure the electrical activity of cultured cortical networks. They showed that spontaneous spiking activity evolved into synchronised bursts during the development of neural networks [Ito et al., 2013]. Furthermore, Gandolfo et al. were able to track bursting patterns in hippocampal cell cultures, which lead them to develop an analysis method to investigate the spatial and temporal patterns of neuron activity and network bursts [Gandolfo et al., 2010]. It is evident that the ability to record signals at high spatial and temporal resolution using CMOS-HDMEAs have made it possible to capture burst activities, which are known to contain various information about neuronal communication [Obien et al., 2015]. More complex experiments such as estimating functional connections in hippocampal neuron cultures were also successfully performed on CMOS-HDMEAs [Maccione et al., 2012]. Besides that, tracking the propagation of action potentials across cells in dissociated cultures was only made possible by the recording capabilities of the CMOS-HDMEA [Bakkum et al., 2013].

It is evident that microelectrodes, such as the CMOS-HDMEA, were developed to record APs by detecting changes in the extracellular field caused by ionic fluxes across the cellular membrane. However, MEAs are not solely specific to the biological samples of interest, and are also sensitive to current flows in the surrounding extracellular medium and neighbouring cells. As a consequence, one should practice caution when detecting and recording signals using a MEA. In MEA recordings, the occurrence of a 'spike', a signal that surpasses a set threshold, is typically associated with an AP. The spike is generally on the order of ten to hundred microvolts in amplitude, depending on the magnitude of the originating AP and distance of the cell from the microelectrode. Furthermore, the spike waveform recorded by a MEA device starts out with a sharp negative dip followed by a positive rise, consistent with the influx of $Na^+$ and the efflux of $K^+$ ions respectively during an AP event [Obien et al., 2015].

The neuron-electrode interface can be described by the equivalent circuits shown in Figure 3–4. In 1968, Robinson developed the first model, describing the interface between neurons and microelectrodes in vivo [Robinson, 1968]. This model was later modified to describe neuron-electrode interfaces in MEAs, and termed the 'point or area contact model', as shown in Figure 3–4 (a) [Fromherz, 2003]. A generalised neuron-electrode model, which is applicable for tissue slices and dissociated cell cultures in MEA devices is shown in Figure 3–4 (b) [Obien et al., 2015]. In the generalised model, the MEA surface is assumed to be an insulator, resulting in a two part separation for the model, termed the upper-"Fluid"-side and lower-"Metal"-side in the illustration. On the upper-"Fluid"-side, the point-source equation, derived by Obien et al. can be used to solve the potential, $V_e$, at any electrode, $e$ [Obien et al., 2013]. In MEAs, the microelectrode measures changes in the rate of ion exchange across the cell membrane. As a result, the cell can be considered to be a system of current sources and sinks, termed point sources in this model. Assuming the extracellular medium to be homogeneous and extending infinitely, the voltage as measured by the microelectrode, $V_e(d_n)$, is given by

$$V_e(d_n) = \frac{1}{4\pi\sigma} \sum_n \left( \frac{I_n}{d_n} \right) \tag{3.1}$$

where $I_n$, is the point-current source, $\sigma$, is the conductivity of the medium, and $d_n$, is the distance between the microelectrode and source, given by

$$d_n = \sqrt{x_n^2 + y_n^2 + z_n^2}. \tag{3.2}$$

Using the method of image charges, the voltage measured for two point-current sources, $I$, located at $(0, 0, z')$ and $(0, 0, -z')$ can be described as,

$$V_e(x, y, z) = \frac{1}{4\pi\sigma} \left( \frac{I}{\sqrt{x^2 + y^2 + (z - z')^2)}} + \frac{I}{\sqrt{x^2 + y^2 + (z + z')^2}} \right) \tag{3.3}$$

However, the extracellular medium does not extend infinitely in the CMOS-HDMEA. Therefore, a first-order boundary condition was put in place by assuming that the surface of the CMOS-HDMEA is an insulating plate. As a result, the distances of the point-current sourses are equal and the point-source equation reduces to,

$$V_e = \frac{1}{2\pi\sigma} \sum \frac{I}{d} \tag{3.4}$$

where, $I$, is the point-current source and $d$, is the distance between the microelectrode and the point-source or point of measurement on the cell [Obien et al., 2013, Obien et al., 2015]. As can be seen from Equation 3.4, the magnitude of the signal measured is highly influenced by the distance between the cell and the microelectrode. In other words, it would be possible to backtrack and estimate the distance between the cell and microelectrodes from Equation 3.4. On the lower-“Metal”-side, the signal transformation by the electrode-electrolyte interface is being described. In this model, the point source potential, $V_e$, is connected to the effective electrode impedance, $Z_e^{'}$, which is then connected in series to the effective amplifier input impedance, $Z_a^{'}$. To briefly describe, the lower-"Metal"-side illustrates the importance of the design of the microelectrodes to achieve high signal resolution of the final signals recorded.

CMOS-HDMEAs have paved an avenue for a new generation of complex, multicellular experiments that will lead to a more in-depth understanding of the brain and other biological specimens. In the next subsection, preliminary results obtained from recordings of dissociated cortical neurons on a CMOS-HDMEA will be discussed. The following experiment was performed in Basel, Switzerland, under the guidance of Milos Radivojevic, to master the use of the CMOS-HDMEA. In-depth analysis of the recorded signals was performed by the author to demonstrate the capabilities of this device.

#### 3.2.3.2 Materials and methods

**Cell cultures**

All animal experimentation were approved by the Basel Stadt veterinary office according to Swiss federal laws on animal welfare and were executed according to the approved guidelines. Cortical neurons were obtained from Wistar rat embryos at embryonic day 18 (E18), according to protocols described in [Hales et al., 2010, Radivojevic et al., 2016]. The cortices were first dissociated enzymatically in trypsin supplemented with 0.25% ethylene-diamine-tetra-acetate (EDTA) (Invitrogen, Life Technologies Inc., Bleiswijk, Netherlands), and physically triturated for 15 minutes at 37°. After that, the trypsin solution was replaced with cell culture plating medium; Neurobasal (Invitrogen, Life Technologies Inc., Bleiswijk, Netherlands) supplemented with 10% horse serum (HyClone, GE Healthcare), $0.5mM$ GlutaMAX (Invitrogen, Life Technologies Inc., Bleiswijk, Netherlands), and 2% B27 (Invitrogen, Life Technologies Inc., Bleiswijk, Netherlands). The cortical tissue was, then, mechanically dissociated gently with a pipette tip and kept aside for cell plating. Before plating the neurons, the surface of the CMOS-MEA was plated with a layer of 0.05% polyethyleneimine (Sigma-Aldrich, St. Louis, MO) diluted in borate buffer solution (Chemie Brunschwig, Basel, CH) for approximately 2 hours. Following that, the polyethyleneimine solution was removed and replaced with $0.02mg/mL$ laminin

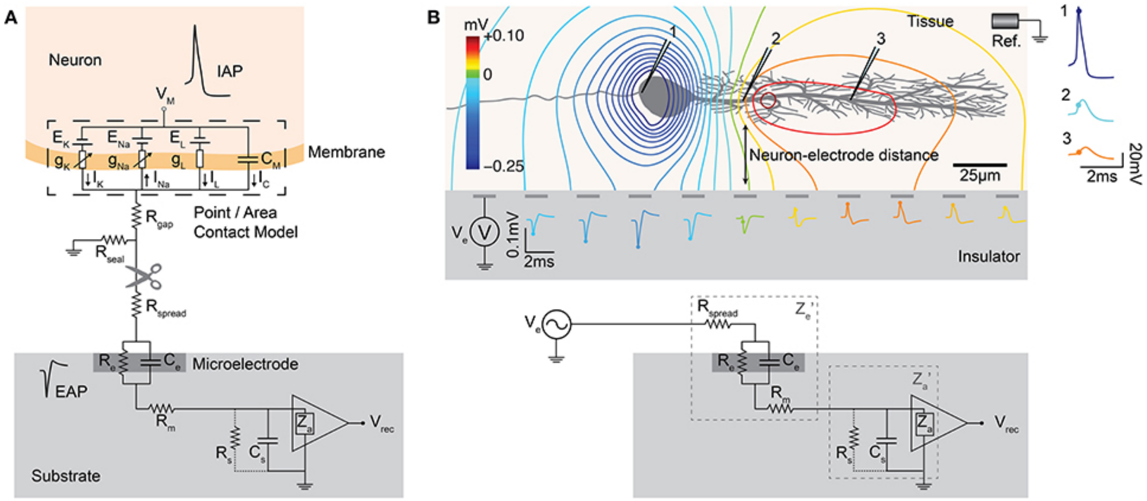

Figure 3–4: **Neuron-electrode interface. a.** Illustration of the point or area contact model derived from [Fromherz, 2003], based on the classic Hodgkin-Huxley model of the squid axon [Hodgkin and Huxley, 1952]. The symbols represented are as follows: $C_M$, capacitance across the neuron membrane, $g_K$, non-linear conductance of the $K^+$ ion channels, $g_{Na}$, non-linear conductance of the $Na^+$ ion channels, $g_L$, linear conductance of the leak ion channels, $E_K$, Nernst potential of the $K^+$ ions, $E_{Na}$, Nernst potential of the $Na^+$ ions, $E_L$, Nernst potential of the leak ions, $I_K$, $K^+$ ion flow, $I_{Na}$, $Na^+$ ion flow, and $V_{rec}$, recorded voltage signal. Examples of AP waveforms are shown as $IAP$ for intracellular recordings and $EAP$ for extracellular recordings. **b.** Illustration of the generalised neuron-electrode interface which can be separated into two parts. On the top half, Upper-"Fluid"-side, potentials at the MEA surface can be solved using the method of images, as the MEA surface is assumed to be an insulator. The figure also illustrates the amplitude of signal recorded due to the neuron-electrode distance. On the lower half, Lower-"Metal"-side, $Z_e'$ represents the effective electrode impedance and $Z_a'$ represents the effective input impedance. The electrical parameters of the electrode-electrolyte interface influence the voltage measured at the electrode. Detailed explanations of the models can be found in [Robinson, 1968, Nelson et al., 2008, Hierlemann et al., 2011, Obien et al., 2015]. This figure was obtained with permission from *Revealing neuronal function through microelectrode array recordings by Obien et al., 2015, Frontiers in Neuroscience, 9(JAN):423., Copyright © 2015 Obien, Deligkaris, Bullmann, Bakkum, and Frey.*

(Sigma-Aldrich, St. Louis, MO) in Neurobasal (Invitrogen, Life Technologies Inc., Bleiswijk, Netherlands). To limit the cells to the MEA, only a drop of cell solution, covering approximately $3mm^2$ was seeded on the centre of the MEA, resulting in cell densities of 1000 - 2000 $cells/mm^2$. After 6 days, the cell culture plating medium was replaced with growth media, consisting of Dulbecco's Modified Eagle Medium (Invitrogen, Life Technologies Inc., Bleiswijk, Netherlands) supplemented with 10% horse serum (HyClone, GE Healthcare), $0.5mM$ GlutaMAX (Invitrogen, Life Technologies Inc., Bleiswijk, Netherlands), and $1mM$ sodium pyruvate (Invitrogen, Life Technologies Inc., Bleiswijk, Netherlands). Cortical cell cultures were kept in an incubator at $37°C$ with 5% $CO_2$.

### CMOS-HDMEA

**CMOS-HDMEA chip:** The CMOS-HDMEA used incorporates 11,011 microelectrodes into a 2.00 x 1.75 $mm^2$ active sensing area, as shown in Figure 3–5. Each microelectrode measures 5 x 7 $\mu m^2$ with a pitch of 18 $\mu m$. The on-chip circuitry consists of a flexible switch matrix and 13,000 static random-access memory cells which allow readout channels to be reconfigured and routed to specific electrodes within the order of milliseconds. The 126 readout channels allow for bidirectional communication, involving recording and stimulation, with the biological samples. Using the 8-bit ADC, biological signals are sampled at 20 $kHz$ per channel, while the two 10-bit digital-to-analog conversion (DAC) can be used to deliver electrical stimuli. There are programmable on-chip gain and filter settings which help in removing direct current (DC) offsets and fluctuations; a first-order high-pass filter with an adjustable cutoff frequency range of 0.3 - 100 $Hz$ and a second-order low-pass filter with a cutoff frequency range of 3.5 - 14 $kHz$. More detailed information about the CMOS-HDMEA can be found in [Frey, 2007, Frey et al., 2007, Frey et al., 2009b, Livi et al., 2010, Müller et al., 2012, Jäckel et al., 2012, Obien et al., 2013, Radivojevic et al., 2016].

**Fabrication:** The CMOS-HDMEA is fabricated in a $0.6\mu m$ 3-metal, 2-polysilicon CMOS-process, resulting in a chip size of 7.5 x 6.3 $mm^2$, as shown in Figure 3–6. Following that, a 2-mask post-processing step involving sputtering 20 $nm$ of Tungsten-titanium (Ti:W) and 200nm of platinum (Pt) is performed. To prevent

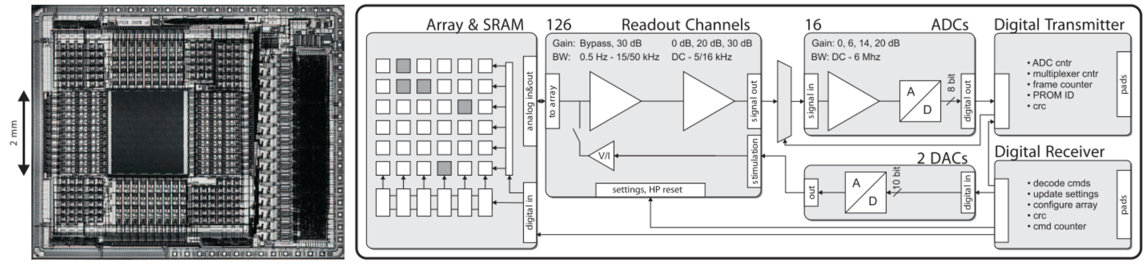

(a) (b)

Figure 3–5: **CMOS-HDMEA. a.** Micrograph of the CMOS-HDMEA. The active electrode array is the black square in the centre of the micrograph. This MEA region measures 2.00 x 1.75 $mm^2$, and is surrounded by on-chip circuitry which are involved with basic functionalities of the CMOS-HDMEA. **b.** Schematic diagram of the on-chip circuitry in the CMOS-HDMEA. This figure was obtained with permission from *Depth recording capabilities of planar high-density microelectrode arrays by U. Frey et al., 2009, 4th International IEEE/EMBS Conference on Neural Engineering, NER '09, 2:207–210, Copyright © 2009, IEEE.*

corrosion, a 1.6 $\mu m$ thick passivation layer of silicon dioxide ($SiO_2$) and silicon nitride ($Si_3N_4$) is deposited. These processing steps were crucial to allow the chip to be functional when in contact with cellular media in physiological conditions. To further ensure long-term stability of the CMOS-HDMEA chips, the Pt electrode openings were shifted away from the CMOS aluminium contact points. There are also on-chip Pt-electrodes integrated around the electrode array which can be used as reference electrodes during measurements. The CMOS-HDMEA chips are connected to a custom-designed printed circuit board (PCB), which is then connected to a field-programmable gate array (FPGA) (re-programmable Virtex II pro FPGA (Xilinx Inc., San Jose, USA)), and a computer. Data is sent to the FPGA board at a rate of 16 $Mb/s$, where the data is pre-processed and sent to the computer for further analysis and processing. Detailed descriptions of the fabrication of the CMOS-HDMEAs can be found in [Frey, 2007, Frey et al., 2007, Heer et al., 2007].

**Packaging:** The CMOS-HDMEA is mounted and wire-bonded on a custom-designed PCB with peripheral component interconnect extended (PCIx) connectors. To protect the bond wires and pads from liquid damage, a glass ring is first glued onto the PCB to create a well. A transparent bio-compatible epoxy (EPOTEK 302-3M, Epoxy

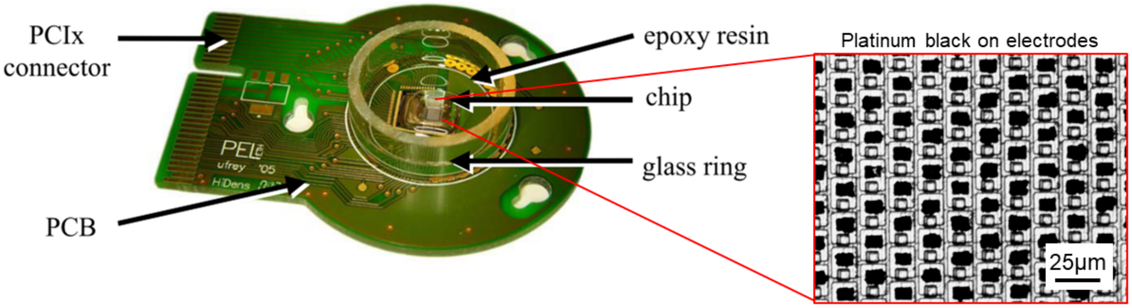

Figure 3–6: **Packaged CMOS-HDMEA.** Packaging the CMOS-HDMEA involves gluing a glass ring and covering the area surrounding the active MEA sensing area with bio-compatible and water-resistant epoxy. Close up figure shows the microelectrodes after platinum black deposition (black rectangles). This figure was obtained with permission from *Cell recordings with a CMOS high-density microelectrode array by U. Frey et al., 2007, Annual International Conference of the IEEE Engineering in Medicine and Biology - Proceedings, pages 167–170, Copyright © 2007, IEEE.*

Technology Inc.) is then used to fill in the areas surrounding the active MEA area. The epoxy coverage allows the CMOS-HDMEA chip to be water-resistant for biological experiments. Platinum black (Pt-black) is further deposited electrochemically on the electrodes to reduce electrode impedance and to increase the electrode-neuron interface area. The Pt-black electrochemical solution consists of 7 $mM$ hexachloroplatinic acid (Sigma-Aldrich, St. Louis, MO) and 0.3 $mM$ lead (II) acetate (Sigma-Aldrich, St. Louis, MO), pH adjusted to 1. On-chip stimulation circuitry is used to apply 180 $mA$ current to all the electrodes simultaneously while a platinum counter electrode is immersed in the Pt-black electrochemical solution. A cotton swab is used to gently pack down the Pt-black into the electrodes during the process. The electrochemical deposition cycle is repeated until a uniform distribution of Pt-black is achieved, as shown in the inset figure of Figure 3–6. More details regarding the CMOS-HDMEA chip packaging can be found at [Frey, 2007].

**Cell recordings**

Cell culture recordings were performed 2 weeks after the cell culture. A thin layer of mineral oil (Sigma-Aldrich, St. Louis, MO) was added to the surface of the growth medium to prevent evaporation and osmolarity changes during experimentation, while allowing $O_2$ and $CO_2$ to pass through to the cells [Hales et al., 2010, Radivojevic et al., 2016]. Recordings were performed in an incubator at $37°C$ with 5% $CO_2$. Spontaneous activity was recorded by performing a block scan, consisting of 147 overlapping block configurations to cover the entire active MEA area (Figure 3–7(a)). Cell signals were recorded from each recording block for 40 $s$, and a 2000 $ms$ delay was implemented to switch recording block configurations.

### 3.2.3.3 Results and discussion

Spontaneous neuronal activity of E18 cortical rat neurons were recorded using a CMOS-HDMEA. Activity from the entire active MEA area was obtained by scanning 147 sequential and overlapping blocks configurations to ensure coverage from all the microelectrodes. A threshold of 5 times the noise level ($5\sigma_n$) was used to identify and isolate spikes from the raw signals, and the average of the spikes are plotted for each electrode in the colour map shown in Figure 3–7(b). There is noticeably high activity in the middle right portion of the MEA area, indicating that there is a high possibility of the presence of spontaneously active neurons. The activity map provides the user with an overview of the viability, activity, and approximate location of neurons that were plated on the CMOS-HDMEA. Without optical verification, one can only perform a calculated assumption of the exact location and number of neurons. Nevertheless, the activity map provides the user with useful preliminary information about the cells that are being cultured on the CMOS-HDMEA.

To further visualise the activity recorded by the microelectrodes, the raw signals from the individual electrodes can be plotted. Figure 3–8 shows neuronal signals from 10 randomly selected electrodes which originated from the same recording block configuration. The signals reveal spiking activity that appear to be a few magnitudes larger in amplitude compared to the base noise level. Additionally, the recordings indicate bursting AP activity in some electrodes and synchronised spiking across most of the electrodes. At this moment, it would be premature to come to any conclusions

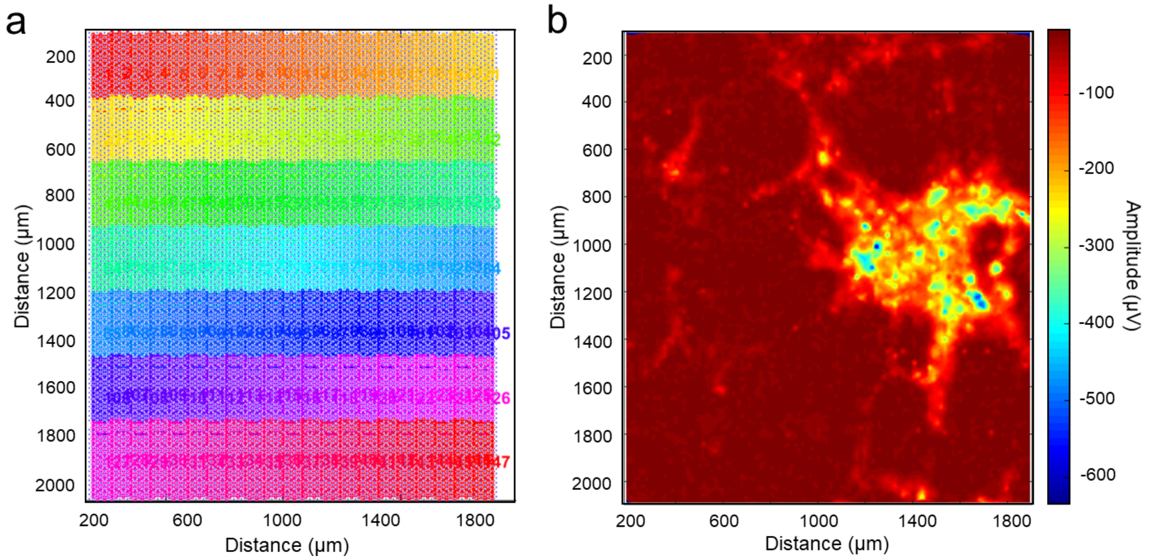

Figure 3–7: **Recording block configurations and activity map. a.** 147 recording block configurations, which are sequential and overlapping, to cover the entire MEA area. Each colour corresponds to a single block configuration. **b.** Spontaneous activity of E18 rat cortical neurons, recorded using the CMOS-HDMEA. The average spiking activity is plotted for each electrode, and there is significantly higher activity in the middle right portion of the MEA area. This first scan provides the user with a rough overview of where the neurons are located on the MEA area.

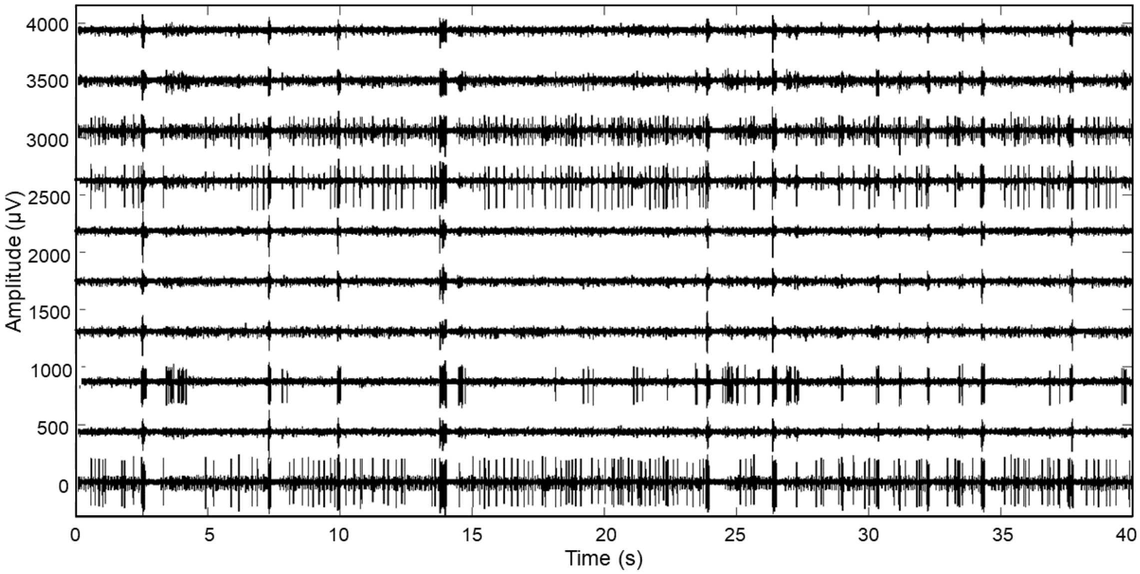

Figure 3–8: **Individual neuronal signals.** Figure shows neuronal signals from 10 randomly selected electrodes from the same recording block. The signals are plotted at a constant offset from one another. The 40s recordings indicate synchronicity across most of the electrodes, and in some cases bursting neural activity.

about the neuronal activity that is being seen, except, to simply confirm that there exist cellular activity at these microelectrodes of the CMOS-HDMEA. Under regular experimental circumstances, subsequent recordings would be performed from selected electrodes, i.e. electrodes that have high cellular activity, which are chosen from the activity map plotted. The subsequent recordings would be specific to the type of experiments that one would like to perform. As an example, the exact position of a cell and its axonal branches can be identified through a spike sorting procedure. For this thesis, no further recordings or experimentation were performed on this cell culture and CMOS-HDMEA as this recording was meant to serve as an introduction to the usage of this specific CMOS-HDMEA.

Following a recording from a CMOS-MEA, the raw signals typically undergo filtering, spike detection, and spike sorting. Filtering using a non-causal band-pass filter, between the range of 300-3000 $Hz$, removes fast APs and low frequency noise, enabling the neuronal spikes to be visualised better. Next, the spikes are identified using amplitude thresholding. The threshold level suggested by Quiroga in 2004 is as follows [Quiroga et al., 2004],

$$Thr = 5\sigma_n \tag{3.5}$$

where,

$$\sigma_n = median\left(\frac{|x|}{0.6745}\right) \tag{3.6}$$

where $|x|$, is the band-pass filtered signal and $\sigma_n$, is an estimate of the standard deviation of the background noise. This amplitude thresholding method is robust against outliers as it is a measure based on the median of the signal. After spike detection via amplitude thresholding, the spikes are sorted by discarding those that reflect random variations and only keeping those which help with spike classification. There are multiple ways to perform spike sorting analysis. For instance, through the comparison of the amplitude, width, and energy of the spikes, or the first principal components, or the wavelet coefficients; factors which will enable the spikes to be separated into clusters. The ultimate goal of spike sorting is to figure out which sets of spikes correspond to which neuron on the MEA, given the assumption that neurons display specific shaped spike waveforms and spiking patterns, which are a result of the neuron morphology itself [Quiroga et al., 2004, Quiroga, 2012, Obien et al., 2015].

In this experimental data, amplitude thresholding was performed according to Equation 3.5 to detect the spikes in the recorded signals from the MEA. All the identified spikes obtained from a single recording trace were plotted in Figure 3–9 (a). The grey lines are individual spikes superimposed in the same figure, while the black line represents the average of all the spikes. From Figure 3–9 (a), two distinct clusters of spikes can be seen. One cluster could be originating from the neuron that is sitting directly above the microelectrode, and the other cluster could be signals originating from close-by neurons. Therefore, taking an average of all the spike traces would lead misleading and inaccurate information about the neuron that resides in that particular location of the MEA. A plot of the spike amplitude

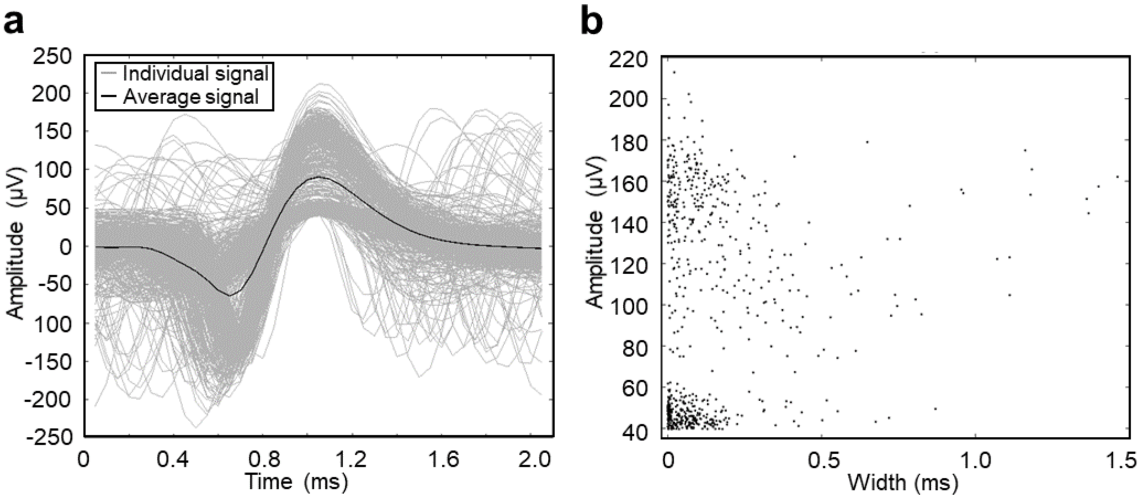

Figure 3–9: **Amplitude threshold spike detection and spike sorting.** A simple method to detect spikes by extracting spikes that meet a certain threshold. **a.** Alignment of all the spikes detected from a single recording trace. The grey lines are individual spike traces, and the black line represents the average of all the grey traces. It is not entirely obvious, but two distinct waveforms can be seen from the spike overlays. **b.** Categorising the detected spikes by amplitude and width (FWHM). The two distinct populations of the spike waveforms are seen more evidently in this plot.

versus the width at full-width half-maximum (FWHM) was made to visualise the distribution of the clusters (Figure 3–9 (b)). It is apparent that there are two clusters of spikes; one group with amplitudes ranging from 130-180 $\mu V$ and another group with amplitudes ranging from 40-60 $\mu V$. Judging by the amplitude of the signals, the former cluster could be originating from the neuron sitting directly above the microelectrode since the magnitude of the voltage recorded is inversely proportional to the distance between the cell and electrode, as previously described in Equation 3.4. And, the latter cluster would be signals originating from surrounding neurons.

For this thesis, further analysis of the signals were performed in attempts to extract more information about the neuronal signals recorded. Recalling the synchronicity seen across the electrodes in Figure 3–8, we were curious to see if those synchronised spikes originated from synchronised neuronal activity or if the coordinated spiking was a result of cross-talk in the system. In order to investigate that, a

3D plot of the spikes detected for all the electrodes, from the same recording block configuration, at a specific time frame was plotted (Figure 3–10 (a)). In both subfigures, the spike traces were plotted as a function of distance and colour coded as darkest blue being the reference microelectrode, blue being the closest neighbouring microelectrode, and red being the farthest neighbouring microelectrode. An electrode map of the microelectrode placement can be found in the inset figure of Figure 3–10 (a). In Figure 3–10 (a), the peak of the spikes are seen to be shifted as the neighbouring microelectrodes are further away from the reference microelectrode. This delay was hypothesised to be a result of AP propagation. The hypothesised propagation speed for spikes recorded from this recording block configuration was calculated and found to be on average $1.01 \pm 0.58\ m/s$. This value corresponds well with physiological values reported in the literature [Bakkum et al., 2013, Radivojevic et al., 2016]. For that reason, we can presume that for this particular time frame, the delay between the spikes was caused by the propagation of AP along the axon of that neuron. Histograms of all the delays calculated from the same recording block configuration is shown in Figure 3–10 (b) and from all 147 recording block configurations is shown in Figure 3–10 (c). The spread of time delays measured whenever there is a spiking activity could be attributed to the position of the microelectrode along the neuron during AP propagation.

A cross-correlation analysis was further calculated for all the signals recorded from the same recording block configuration, to rule out the possibility that the synchronicity across the microelectrodes could be a result of cross-talk between the microelectrodes. Figure 3–11(a) shows the results of the cross-correlation analysis, where the darkest blue trace represents the auto-correlation of the reference electrode with itself, and blue to red traces correspond to neighbouring electrodes that are increasing in distance from the reference electrode. The peak of the cross-correlation coefficient was plotted as a function of distance from the reference electrode in Figure 3–11(b), highlighting the significant drop in correlation coefficient of the neighbouring electrodes from the reference electrode. The findings imply that there is very little to no cross-talk between the microelectrodes, therefore, implying that the CMOS-HDMEA was in proper function and that the signals were neuronal in nature, consistent with previous signal analysis.

For completion, the rate of firing was calculated to determine if there were any trends in the firing patterns of the neurons. A raster plot for all the electrode

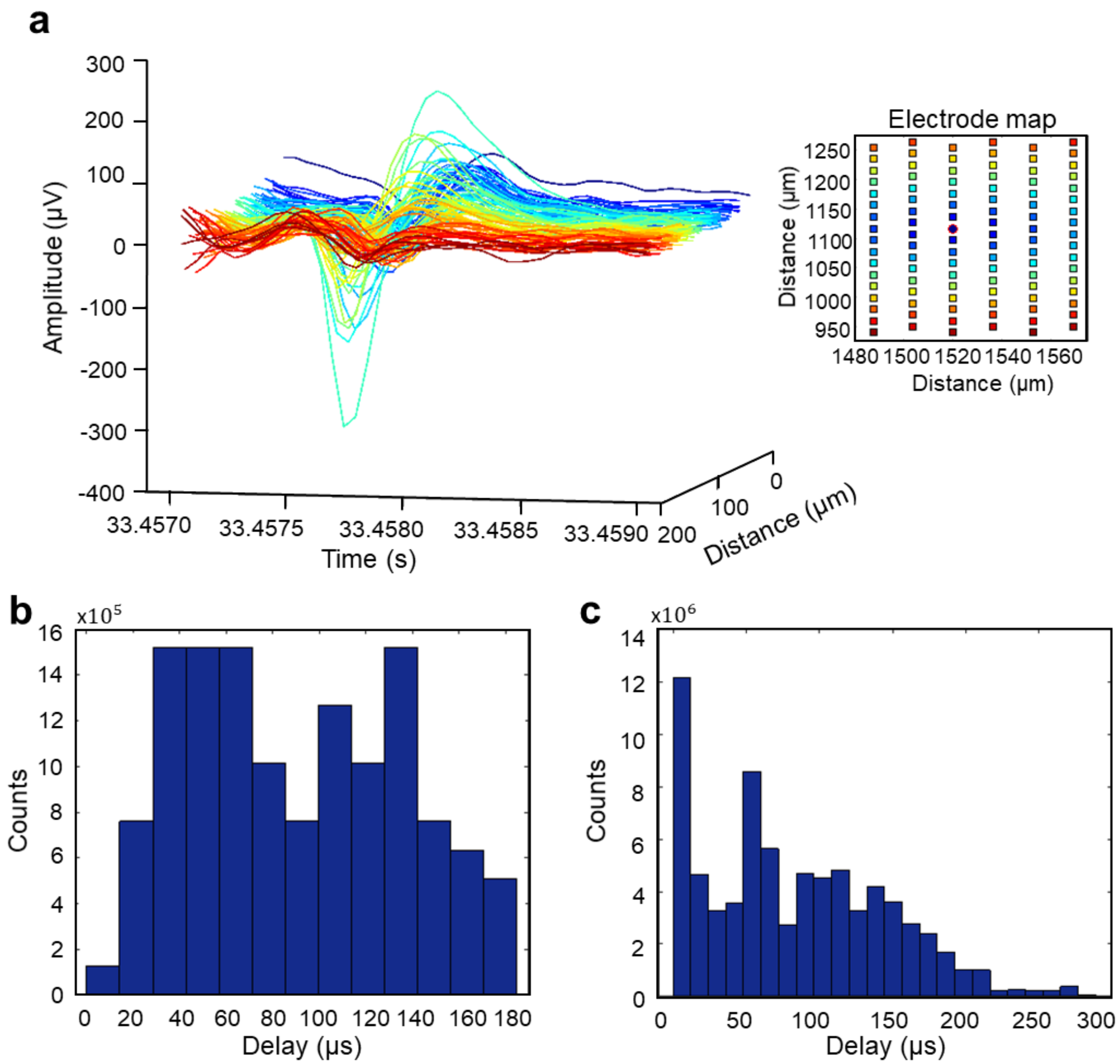

Figure 3–10: **Spike delay across the microelectrodes.** **a.** Spikes detected are superimposed on top of one another and colour coded by distance (red colour being far from the reference electrode and blue colour being close to the reference electrode). **b.** Histogram of delays obtained by subtracting the moments the spikes meet the peak of the AP from that of the reference electrode from a single recording block. **c.** Histogram of delays from all the electrodes from signal traces from all 147 recording blocks.

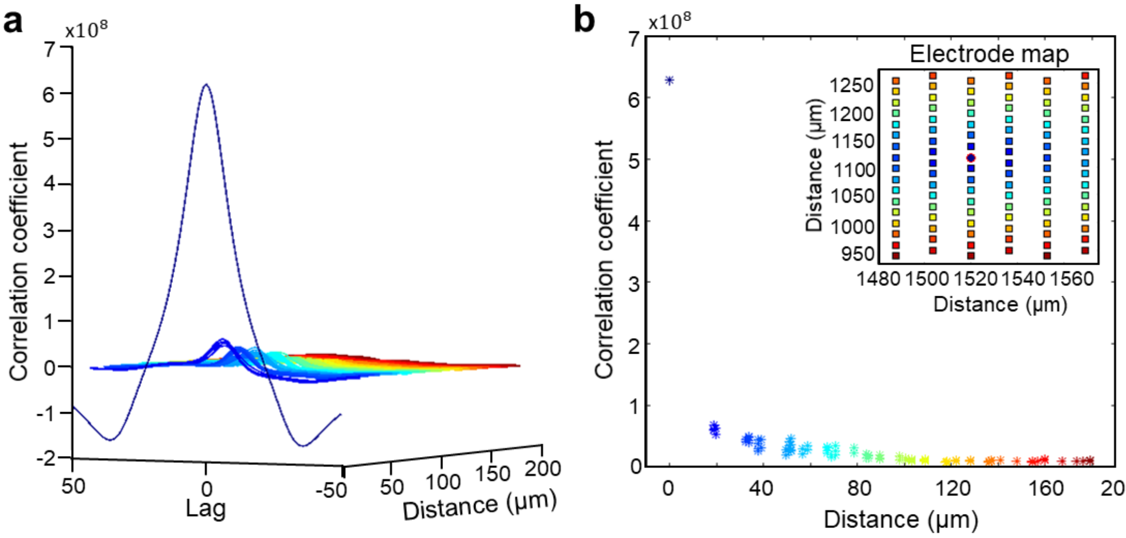

Figure 3–11: **Signal cross-correlation. a.** Cross-correlation of the signals against the reference electrode, and colour coded as a function of distance from the reference electrode. In the figure, 1 unit of Lag represents $50\mu s$. **b.** The peak of the cross-correlation plotted as a function of distance from the reference electrode. At 0 $\mu m$, there is high correlation, and is expected when performing a cross-correlation with the reference signal itself. Subsequent cross-correlation with neighbouring electrodes show a decline in correlation coefficient, that is also decreasing as a function of distance. This indicates that the signals are not correlated with one another even though they do show some similarities and synchronicity across the electrodes.

recordings from a single recording block configuration was made and shown in Figure 3–12(a). The number of spikes detected at a given time was plotted in Figure 3–12(b). These spike counts were further averaged at every 100 $ms$ to take into account the average delay between the microelectrodes during an AP propagation, thus resulting in a timeline of the rate of firing of the neurons (Figure 3–12(c)). The results indicate moments of high activity and periods of quiescence during the 40 $s$ recording. However, there were no obvious periodic firing patterns from the cells. The lack of periodicity could be attributed to the fact that neurons, unlike cardiomyocytes, do not exhibit consistent periodic firing behaviour.

## 3.3 Conclusion

In this chapter, the fundamentals of cellular signalling in electrogenic cells, specifically neurons and cardiomyocytes, are highlighted. Cellular signals contain a plethora of information which, till this day, remains a challenge to the scientific world to decode and truly understand the complexity of the information that is being transmitted. As a result, various electrophysiology tools and techniques have been developed over the years to improve the quality of signals collected by reducing the damage done to the biological sample, introducing experimental conditions which are close to the native environment, diversifying the types of measurements that can be made, etc. Here, we show that the CMOS-HDMEA is a powerful device that is able to record signals from multiple locations on cells while maintaining high spatial and temporal resolution. The ability to perform long term measurements on a group of cells allows for the discovery of information on cellular interaction and communication within a cellular network.

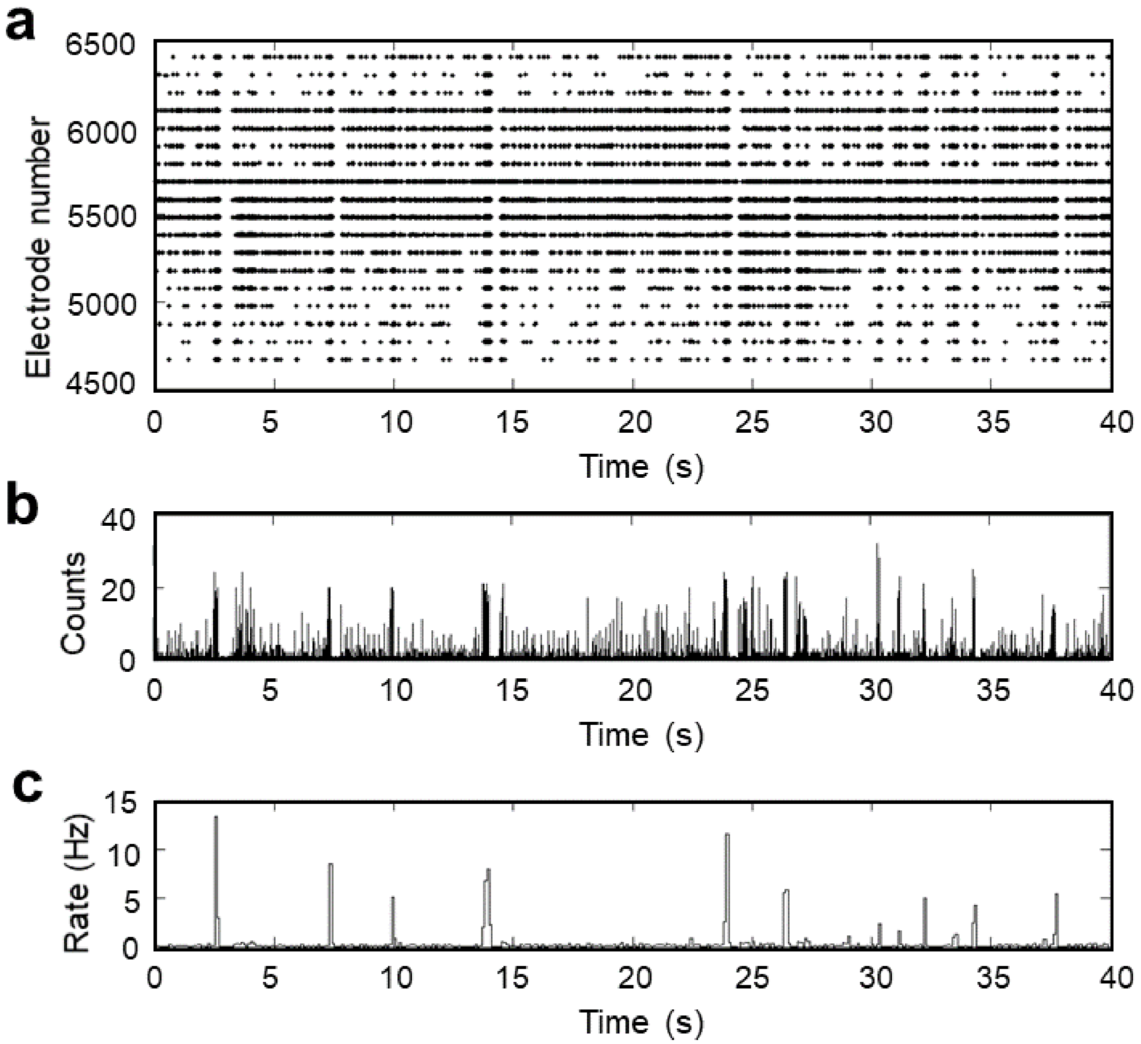

Figure 3–12: **Raster plot. a.** Spiking events plotted as dots for each electrode in a recording block. **b.** Sum of spiking events across the electrodes, plotted as a function of time. **c.** Rate of firing obtained by averaging the number of spike counts over a 100 $ms$ time frame.

# CHAPTER 4

# AFM AND CMOS-HDMEA INTEGRATED SETUP

## 4.1 Cellular changes accompanying action potentials

Action potentials are commonly referred to as an electrical phenomena. This comes to no surprise as one of the first models describing electrical behaviour of the surface membrane of a giant nerve fibre was the Hodgkin-Huxley model. This model, developed by Hodgkin and Huxley in 1952 (Figure 4–1), was based on the assumption that the electric nature of the AP was caused by charging of the membrane capacity or by ion fluxes through the membrane [Hodgkin and Huxley, 1952]. In the Hodgkin-Huxley model, the total membrane current density, $I$, is given by,

$$I = C_M \frac{dV}{dt} + I_i \tag{4.1}$$

where, $C_M$ is the membrane capacitance, $V$ is the change in membrane potential from its resting value, $t$ is time, and $I_i$ are the inward ionic currents. $I_i$ can be divided into three components; sodium ionic current ($I_{Na}$), potassium ionic current($I_K$), and small leakage currents ($I_l$) which arise from chloride and other ions, and is described as follows,

$$I_i = I_{Na} + I_K + I_l. \tag{4.2}$$

Each of the ionic currents can be further described by the general equation,

$$I_x = g_x(E - E_x) \tag{4.3}$$

where subscript $x$ represents the ions ($Na^+$, $K^+$, or leakage ions), $g_x$ is the conductance of the ionic channels, $E$ is the membrane potential, and $E_x$ is the equilibrium potential for the ion. Substituting Equation 4.3 for each ion type into Equation 4.1 results in,

$$I = C_M \frac{dV}{dt} + g_{Na}(E - E_{Na}) + g_K(E - E_K) + g_l(E - E_l). \tag{4.4}$$

It is important to take note that in the Hodgkin-Huxley model, the only variables that are functions of time and membrane potential are $g_{Na}$ and $g_K$, while all the other parameters are assumed to be constant. This assumption was made on the basis that action potential waveforms are formed by the initial transient influx of sodium ions and later a slow efflux of potassium ions, as discussed previously in Chapter 3 [Hodgkin and Huxley, 1952].

The Hodgkin-Huxley model has undeniably described the electrical dynamics of the membrane, however, further studies in this subject matter have shown that there are other cellular properties which change during action potential signalling.

### 4.1.1 Mechanical and thermal changes of neurons in response to voltage stimulation

The first observations indicating physical change in nerve fibres were from studies done by D. K. Hill in 1950 [Hill, 1950]. Upon studying the nervous system of *Sepia officinalis* (common cuttlefish), he noticed the nerve fibre swelling as a result of stimulation. Swelling of the fibre was thought to be a result of an increase in osmotic

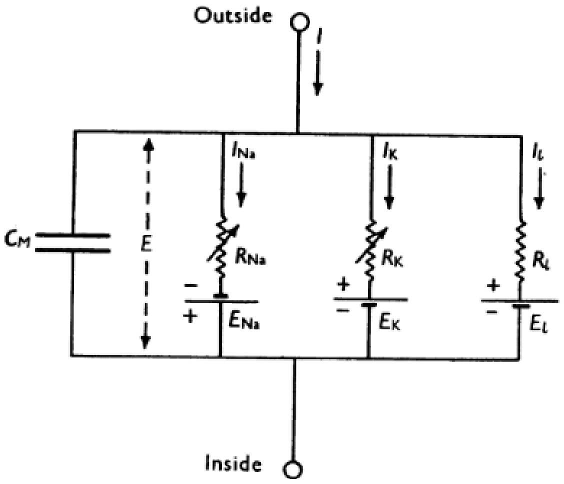

Figure 4–1: **Hodgkin-Huxley electrical circuit model of the membrane.** This model was developed to describe the electrical behavior of the membrane of a giant nerve fibre. The electrical resistances are defined as $R_{Na} = 1/g_{Na}$; $R_K = 1/g_K$; $R_l = 1/g_l$, where $g_{Na}$ is the sodium ion conductance, $g_K$ is the potassium ion conductance, $g_l$ is the leakage ion conductance made up by chloride and other ions. The rest of the symbols are as follow: $I_{Na}$, sodium ionic current, $I_K$, potassium ionic current, $I_l$, leakage ionic current, $E_{Na}$, equilibrium potential for sodium ions, $E_K$, equilibrium potential for potassium ion, $E_l$, equilibrium potential for leakage ions, $E$, membrane potential, and $C_M$, membrane capacitance. In this model, $R_{Na}$ and $R_K$ vary with time and membrane potential, consistent with the transient increase in sodium conductance and slow increase in potassium conductance when a membrane is depolarised. This figure was obtained with permission from *A quantitative description of membrane current and its application to conduction and excitation in nerve by A. L. Hodgkin and A. F. Huxley, 1952, The Journal of Physiology (117) p500-544, Copyright © 1990, Springer Nature.*

pressure inside the fibre due to the exchange of sodium, potassium, and sodium chloride across the cell membrane. Furthermore, he observed a change in length of the nerve fibre of giant *Loligo paelii* (squid) axons in relation to a change in volume and the tension applied to the nerve fibre. More specifically, when there was an increase in volume in the nerve fibre, the fibre lengthened when it was under low tension, and conversely shortened when the tension was higher [Hill, 1950].

After that, researchers began to publish results of detailed studies on mechanical changes in axons that were associated with action potential signalling. Starting with Hill et al. in 1977, they observed a change on the surface of the axon when an AP was travelling along the axon of the *Procambarus clarkii* crayfish. The surface displacement was reported to occur within 1 millisecond and approximately 18 angstroms in amplitude [Hill et al., 1977]. This result was confirmed by Iwasa and Tasaki in 1980, who also observed rapid and small displacements, on the order of 0.5 $nm$, on the surface of giant *Loligo paelii* axons following an action potential [Iwasa and Tasaki, 1980]. The duo continued investigating the time course and magnitude of the axon swelling phenomena using various optical and mechanoelectrical methods, all of which generated consistent results, i.e. an upward displacement of the nerve surface and an increase in pressure inside the nerve fibre during an action potential [Iwasa et al., 1980]. In 1982, Tasaki and Iwasa confirmed that the swelling of the axon does correspond to the action potential. Their findings also showed that burst of action potentials do not lead to additional swelling of the membrane, and that membrane swelling resulted in shortening of the axon [Tasaki and Iwasa, 1982]. Figure 4–2 (A) show the mechanical response of the olfactory nerve of the *Lepisosteus osseus* garfish in response to an electrical stimulation. The results also show that the peak of the swelling also coincides with the peak of the action potential (Figure 4–2 (B)), confirming the fact that the membrane displacement is not a mere coincidence or an act of a random event [Tasaki et al., 1989]. Finally, recent AFM recordings on giant axons of *Homarus americanus* lobsters show mechanical displacements on the order of 2 - 12 angstroms, in phase with voltage stimulation of the axon [Gonzalez-Perez et al., 2016]. In short, action potential signalling in neurons are not solely electrical in nature. Various studies on multiple types of axons have proven that there is indeed a mechanical displacement in the axon membrane, which accompanies the voltage change.

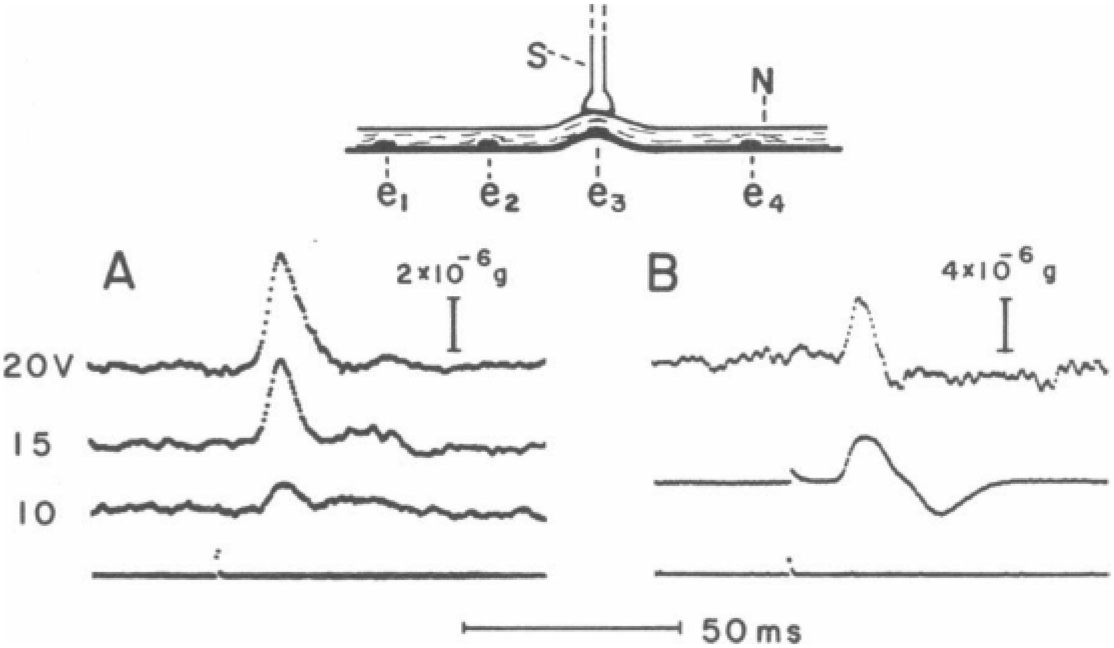

Figure 4–2: **Mechanical responses of a garfish olfactory nerve to voltage stimulation.** The labels $S$ represents the stylus used to detect mechanical changes in the nerve, and $N$ represents the nerve fibre. **A.** Mechanical displacements detected by the stylus in response to voltage pulses of 10, 15, and 20V. The voltage was applied to the nerve using electrodes $e_1$ and $e_2$, and are 0.5 $ms$ in duration. **B.** Mechanical response (top trace) and voltage response (bottom trace) of the nerve fibre. The results show the temporal relationship between the membrane displacement and the action potential. Electrodes $e_3$ and $e_4$ were used to record the voltage responses of the nerve fibre, and was observed to be $\approx 6\ mV$ in amplitude. This figure was obtained with permission from *Rapid mechanical and thermal changes in the garfish olfactory nerve associated with a propagated impulse by I. Tasaki, K. Kusano, and P. M. Byrne, 1989, Biophysical Journal, 55(6):1033–1040, Copyright © 1989, Tasaki, Kusano, and Byrne.*

In addition to mechanical changes, thermal responses were also observed in the nerve fibres following electrical stimulation. Using a voltage collision technique, illustrated in Figure 4–3 (a), and a heat-sensor fabricated with thick polyvinylidene fluoride film, Tasaki et al. were able to capture the thermal responses of the garfish olfactory nerve. Their results also show that the peak of the thermal response aligns with the peak of the action potential, and that the duration of the thermal change is similar to that of the action potential (Figure 4–3 (b)) [Tasaki et al., 1989]. The concept of thermal change during action potential signalling is not new, as heat production in non-medullated nerves of *Maia* spider crabs were previously observed by Abbott et al. in 1958. Following an impulse at $0°C$, the team first observed an increase in heat ($\approx 9\text{x}10^{-6}\ cal/g$) and later a slow reduction in heat ($\approx 7\text{x}10^{-6}\ cal/g$) [Abbott et al., 1958]. Similar observations of the initial positive and subsequent negative heat production was also observed in desheathed vagus nerves of rabbits [Howarth et al., 1968, Howarth, 1975].

There are several theories which attempt to explain the thermal and mechanical changes in neurons during action potential signalling. The initial positive heat production is thought to be a result of the exchange of $Na^+$ and $K^+$ ions across the membrane, while the subsequent negative heat production is thought to be a product of certain endothermic chemical reactions [Abbott et al., 1958]. From another perspective, the mechanical and thermal responses were hypothesised to be linked to the release and re-binding of $Ca^{2+}$ ions in the axon during an action potential [Tasaki et al., 1989]. Recent studies using a high bandwidth AFM suggest that the mechanical changes are associated with water entry into the cell, hypothesised as a result of $Na^+$ influx during action potential signalling [Kim et al., 2007]. In summary, the alignment of thermal and mechanical responses in neurons to action potentials, suggest that these processes are linked to voltage changes in the membrane. However, the exact mechanisms are relatively unknown.

### 4.1.2 Modelling the mechanical and thermal changes of neurons during an action potential

While detailed studies have been focused on verifying and quantifying the mechanical and thermal changes in neurons, very little has been done to model these phenomena. El Hady and Machta presented one of the few models that describe mechanical changes in neuronal membranes [El Hady and Machta, 2015]. In their model, the

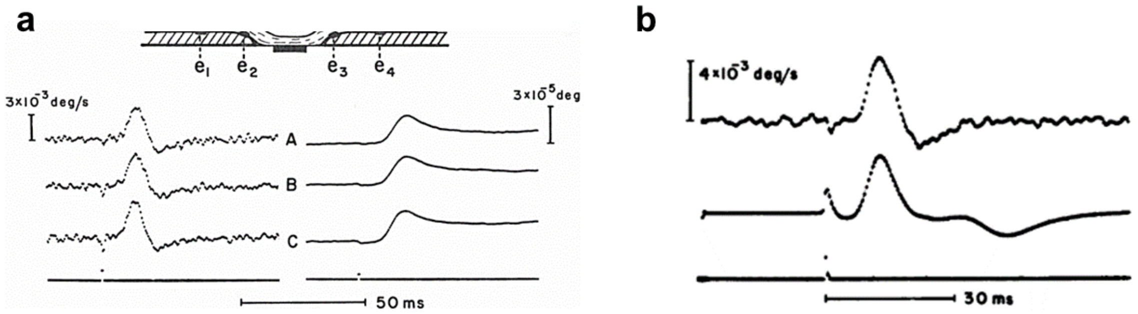

Figure 4–3: **Thermal response of the garfish olfactory nerve in response to voltage stimulation. a.** (Top) Illustration of the experimental setup used to generate a voltage collision and to record thermal responses of the nerve. Electrode pairs $e_1$ and $e_2$, and pair $e_3$ and $e_4$ were used to deliver voltage pulses simultaneously from opposite ends of the heat sensor (middle bottom plate). (Bottom) Thermal responses recorded when: A. a short voltage pulse was delivered to the nerve fibre from one end of the heat-sensor (the exact end of the heat-sensor was not specified in the paper), B. a short voltage pulse was delivered to the nerve fibre from the other end of the heat-sensor, C. two short voltage pulses were delivered from both ends of the heat-sensor simultaneously. **b.** Thermal response (top trace) and action potential (bottom trace), $\approx 8\ mV$ in amplitude, of the nerve fibre. The thermal response was recorded using the collision technique described above. The results show that the peak of the thermal response coincides with the peak of the action potential. This figure was obtained with permission from *Rapid mechanical and thermal changes in the garfish olfactory nerve associated with a propagated impulse by I. Tasaki, K. Kusano, and P. M. Byrne, 1989, Biophysical Journal, 55(6):1033–1040, Copyright © 1989, Tasaki, Kusano, and Byrne.*

axon is an elastic and dielectric tube, filled with and enclosed in viscous fluid. An illustration of the mechanical wave model is shown in Figure 4–4 (a). When the neuron is depolarised, an action potential is sent down the axon. Ensuing that is a change in the charge separation across the axonal membrane, which subsequently changes the surface forces that govern the geometry of the membrane. Displacements of the membrane resulting from the changes in surface forces is termed action waves (AW). In the absence of displacement, the axon has a tube radius of $r_0$ and extends infinitely in the $z$ direction, as shown in Figure 4–4 (a). Assuming that through non-slip boundary conditions, the displacement field carries the axonal surface along with it, the distortions of the axonal surface can be described by $\Delta$; the relative height field, $h$,

$$h(z,t) = \Delta_\rho((r_0), z, t)/r_0 \tag{4.5}$$

and the lateral stretch field, $l$,

$$l(z,t) = \frac{\partial}{\partial z}\Delta_z(r_0, z, t). \tag{4.6}$$

In El Hady and Machta's mechanical wave model, change in the membrane potential causes the mechanical responses seen in the axon membrane. Figure 4–5 shows simulation results of their model. The electrical component of the action potential, shown in Figure 4–5 (a), is described as a travelling wave with the equation,

$$V(z,t) = \mathcal{V}(x) \tag{4.7}$$

where $x = z - C_{AP}t$ is the moving coordinate and $C_{AP}$ is the propagation speed of the action potential. The driving force, shown in Figure 4–5 (b), that induces the mechanical changes in the axon surface is expressed as,

$$F^h(z,t) = \mathcal{F}(x) = 2\pi r_0 C_0 \mathcal{V}_m^2(x). \tag{4.8}$$

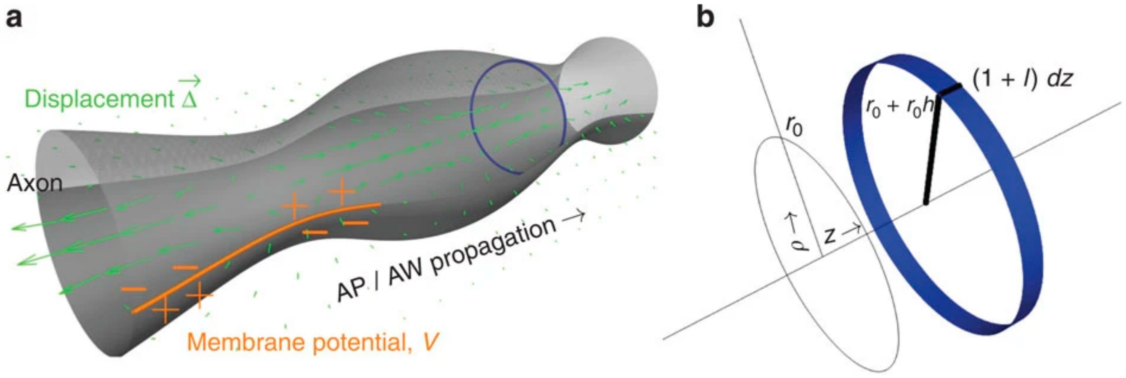

Figure 4–4: **Mechanical wave model. a.** Illustration of the mechanical wave model. The action potential (AP) and action wave (AW) are shown to travel down the axon together. The axonal membrane (grey tube) is being depolarised from left to right in the illustration. Changes in the membrane potential (V) is shown in orange (+ and − signs). In this model, the mechanical surface wave consists of a change in the geometry of the surface of the axon, and displacements of the axoplasmic and extracellular fluid, shown as, $\vec{\Delta}$ green arrows, in the illustration. **b.** Without displacement, the axonal tube has a radius of $r_0$, and extends infinitely in the $z$ direction. Distortions of the surface can be described by the relative height field, $h$, and the lateral stretch field, $l$. This figure was obtained with permission from *Mechanical surface waves accompany action potential propagation by A. El Hady and B. Machta, 2015, Nature Communications,6:1–7, Copyright © 2015, Springer Nature.*

The two mechanical responses of the axon are shown in Figure 4–5 (c,e) for the membrane displacement, given by the term,

$$2\mathcal{D}_{\rho}(r_0, x) \tag{4.9}$$

and in Figure 4–5 (d,f) for the average lateral displacement inside the axon, given by the term,

$$\bar{\mathcal{D}}_z(\rho < r_0, x) = 1/\pi r_0^2 \int_0^r 2\pi\rho d\rho \mathcal{D}_z(\rho, x). \tag{4.10}$$

Two sub-cases are shown, where $\alpha$, a Reynolds-like number, is $\alpha \ll 1$, and $C_{pr}$, the propagation velocity, is $C_{pr} > C_{AP}$ in Figure 4–5 (c,d) and $C_{pr} < C_{AP}$ in Figure 4–5 (e,f). The mechanical wave model simulation results show that there is a rise in membrane displacement, indicating axonal swelling, that is inline with the peak of the action potential, and a negative displacement following that. Additionally, the results show a shortening of the axonal tube during the action potential. The mechanical responses return to 'rest' configurations as soon as the action potential passes [El Hady and Machta, 2015]. The results of the mechanical wave model are in agreement with previously reported values on squid giant axons and garfish olfactory nerve fibres [Tasaki and Byrne, 1988, Tasaki, 1988, Tasaki et al., 1989, Tasaki and Byrne, 1990, Tasaki and Byrne, 1992, Tasaki and Byrne, 1982, El Hady and Machta, 2015]

In addition to mechanical responses, El Hady and Machta also studied the thermal responses of the axon, where two sources of heat that accompanied the action potential propagation were considered. The first is electrostatic heat, derived from heat production from the influx of $Na^+$ ions and heat absorption from the efflux of $K^+$ ions from the cell. The second is mechanical heat, derived from heat production from the distortion of the axonal membrane when the action wave passes. Results of their model simulation show an initial rise in temperature, aligning with the onset of the action potential, and a decrease in temperature following that [El Hady and Machta, 2015].

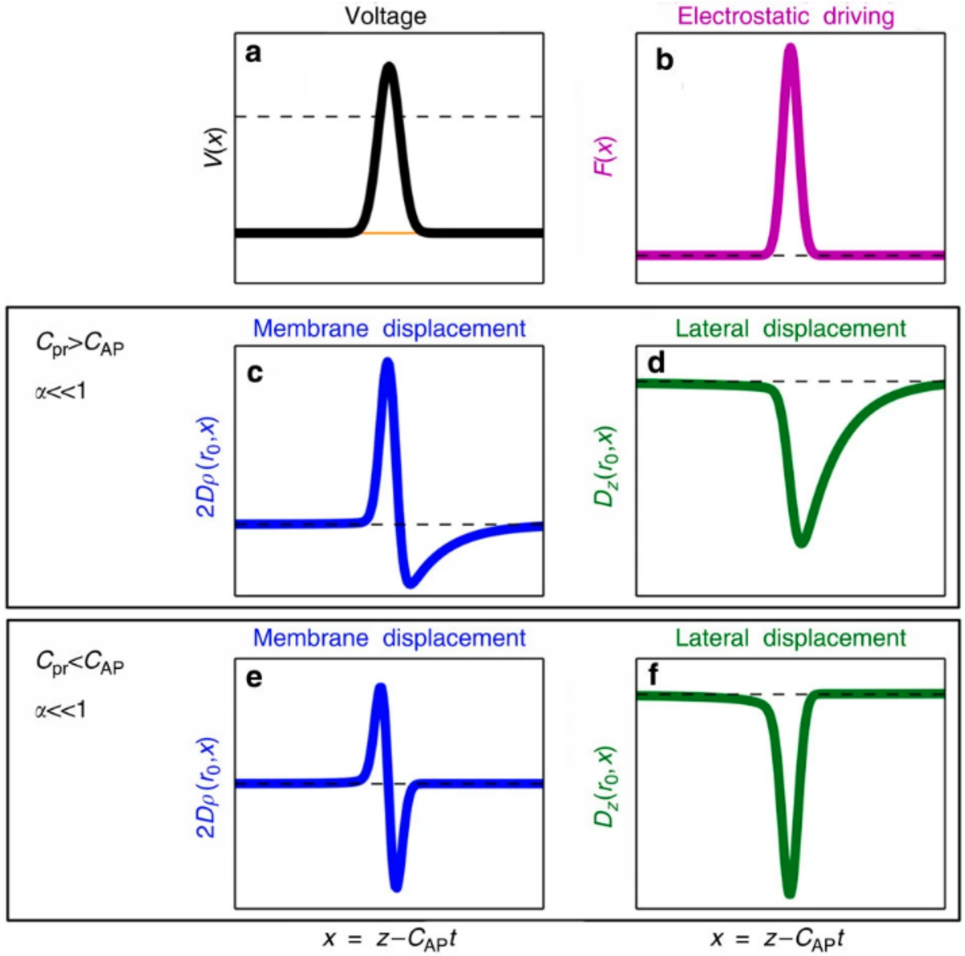

Figure 4–5: **Membrane and lateral displacements caused by an electrical driving force. a.** Electrical component of the action potential, with a Gaussian waveform, shown in black. The resting membrane potential ($\Delta\psi$) is shown in orange. **b.** The driving force that results in mechanical changes in the axon. **(c,e)** Radial membrane displacements of the axonal tube. **(d,f)** Average lateral displacement inside the axon. The conditions imposed are $\alpha \ll 1$ and $C_{pr} > C_{AP}$ for **(c,d)**, and $\alpha \ll 1$ and $C_{pr} < C_{AP}$ for **(e,f)**. This figure was obtained with permission from *Mechanical surface waves accompany action potential propagation by A. El Hady and B. Machta, 2015, Nature Communications,6:1–7, Copyright © 2015, Springer Nature.*

The mechanical wave model presented by El Hady and Machta shows how a mechanical and thermal responses accompany action potentials. They have brought forth a more physiologically accurate model representation of the action potential, which is an improvement from the classic Hodgkin-Huxley model, and have paved the way to better understand neuronal or cellular signalling in general.

## 4.2 Modern techniques to measure mechanical changes during action potential signalling

In order to expand our understanding of the physical responses of electrogenic cells in response to electric stimulation, new and improved methodologies or techniques are required, to obtain recordings with higher spatial and temporal resolution or to perform more complex and elaborate experiments. One such example of this is the replacement of the piezoceramic benders by AFMs to record mechanical displacements in nerve fibres. AFM, as mentioned in previous chapters, is a highly sensitive instrument which can record changes on the subnano-metre scale. Therefore, allowing the user to capture minute cellular changes which may be crucial in the understanding of certain cellular processes. For instance, Gonzalez-Perez et al. were able to detect mechanical displacements, ranging from 2 - 12 angstroms, in giant *Homarus americanus* lobster nerves. Observations of mechanical displacements of this order was only made possible by the sensitivity of the AFM. Further expanding on this concept, the AFM or similar advanced tools would be the only means of recording mechanical changes in mammalian axons, which can be as small as 1 $\mu m$ in diameter [Magdesian et al., 2012]. Figure 4–6 shows the AFM and nerve chamber set up used by Gonzalez-Perez et al.. The exposed medial and lateral giant axons were placed on a nerve chamber, where pairs of electrodes could stimulate and record electrical signals from the axons. At the same time, a tipless AFM cantilever is positioned on top of the axons to record mechanical displacements that occurred during the collision experiments (i.e. when opposite ends of the axon are stimulated at the same time) in the nerve chamber. In addition to recording mechanical displacements of the axon during the collision experiments, the team also observed that colliding action potentials tended to pass through one another without cancelling one another out [Gonzalez-Perez et al., 2016].

Moreover, technological advancements in optical microscopy techniques, have paved the way for measuring mechanical displacements in cells without the addition

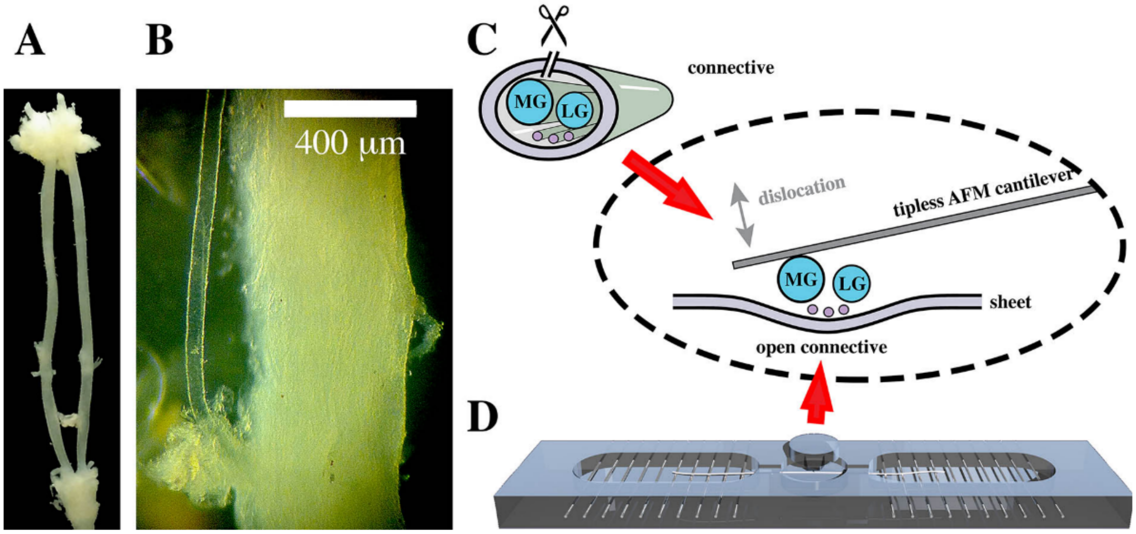

Figure 4–6: **AFM-Nerve chamber setup.** **A.** Image of the lobster connective tissues. **B.** Close up image of the lateral giant axon. **C.** Illustration of the lobster connective nerve fibre, containing the medial giant (MG) axon and the lateral giant (LG) axon. The sheath of the connective tissue is cut open in the longitudinal direction, to expose the MG and LG axons. The exposed axons are placed on the nerve chamber (D), where pairs of electrodes are used to stimulate and record signals from the axon. Additionally, a tipless AFM cantilever is positioned on top of the MG and LG axons to measure mechanical displacements during electrical stimulation. **D.** Image of the nerve chamber used to perform collision experiments on the axons. This figure was obtained with permission from *Solitary electromechanical pulses in Lobster neurons by Gonzalez-Perez A. et al., 2016, Biophysical Chemistry, 216(15):51–59, Copyright © 2016, Elsevier.*

of dyes which could interfere with and alter the cytoskeletal properties of the cell. Such signals, termed “intrinsic optical signals”, are true to the cell being studied. By measuring the change in transmission of light through the axon and utilising image subtraction analysis, Douglas Fields et al. was able to show the microscopic swelling in cultured mouse DRG axons that accompany action potentials [Douglas Fields, 2012]. In the same year, Oh et al. reported a low-coherence interferometric microscopy technique, which enabled them to detect changes in the cell structure of HEK 293 mammalian cells during electrical stimulation [Oh et al., 2012]. More recently, a similar study by Yang et al. observed mechanical displacements in the range of 0.2 to 0.4 $nm$ in mammalian cells, using a combined optical imaging and patch-clamp set up [Yang et al., 2018]. Swelling of the axonal membrane is attributed to transmembrane exchange of ions and water and electrostriction effects of the membrane during an action potential [Douglas Fields, 2012, Oh et al., 2012]. It is important to point out that optically imaging changes in the neuron membrane is very challenging as mammalian cells are optically transparent and very small in dimension, with the added problem of changes in refractive index due to changes in ion concentration which could mimic a false change in dimension of the neuron. To known knowledge, these are the first few reported results of mechanical responses in mammalian cells using optical methods paired with electrical stimulation methods.

The first attempt at a fully non-invasive set up was by Shenai et al. in 2004., who introduced the first AFM-MEA set up. Using the AFM-MEA set up, they observed a 30%-40% decrease in neurite cross-section of cultured neuroblastoma cells shortly after electrical stimulation [Shenai et al., 2004]. Shenai’s AFM-MEA set up served as a proof of concept for a device of this kind. In 2011, Cogollo et al. improved upon the AFM-MEA set up by combining a commercial AFM and planar MEA (Figure 4–7). The planar MEA consists of 60 microelectrodes fabricated on a glass substrate, which is extremely beneficial, as the transparency of the MEA substrate allows the cardiomyocyte and AFM tip to be accessed optically. Utilising this AFM-MEA set up, Cogollo et al. were able to perform precise measurements of mechanical and electrical responses from living cardiomyocytes.

An example AFM-MEA recording on two different cardiomyocytes are shown in Figure 4–8. The AFM tip, kept in place on top of the cell by applying a constant force of 0.5 $nN$, was able to reflect the mechanical displacements of the cardiomyocytes.

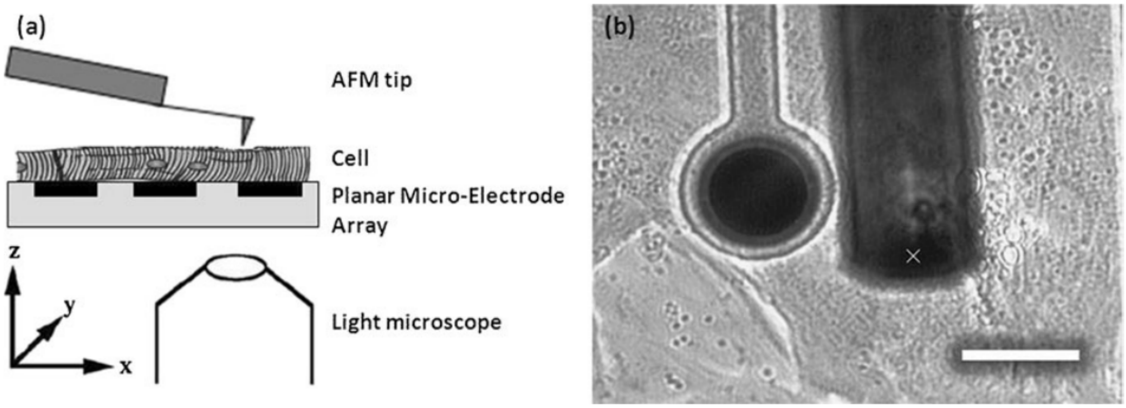

Figure 4–7: **AFM-MEA set up. a.** Illustration of the combined AFM-MEA set up. Cells are cultured directly on the planar MEA surface, while the AFM tip probes and measures mechanical displacements of the beating cardiomyocytes. Inverted optical access is possible since the MEA platform is made of a transparent substrate. **b.** Image of the AFM cantilever next to a microelectrode. The AFM tip (marked 'x') is indenting a beating cardiomyocyte. The scale bar measures 30 $\mu m$ in the figure. This figure was obtained with permission from *A new integrated system combining atomic force microscopy and micro-electrode array for measuring the mechanical properties of living cardiac myocytes by J. Cogollo. et al., 2011, Biomedical Microdevices, 13(4):613–621, Copyright © 2011, Springer Nature.*

Through these experiments, Cogollo et al. were able to monitor the contraction-relaxation cycle of cardiomyocytes, as well the associated mechanical changes. The results also show clearly the synchronicity between the action potentials and the mechanical changes in the cardiomyocytes [Cogollo et al., 2011]. In a very similar experiment, Tian et al. reported a very similar experimental AFM-MEA setup to detect electromechanical activities in cardiomyocytes [Tian et al., 2017].

Amongst all the modern methodologies mentioned, the AFM-MEA set up seems to be the most adaptable and versatile option with the most potential for complex experiments. Both Cogollo and Tian have proved that precise and accurate measurements can be made on cardiomyocytes with this set up. One can only imagine the potential that this set up has for studying mechanical responses in neurons.

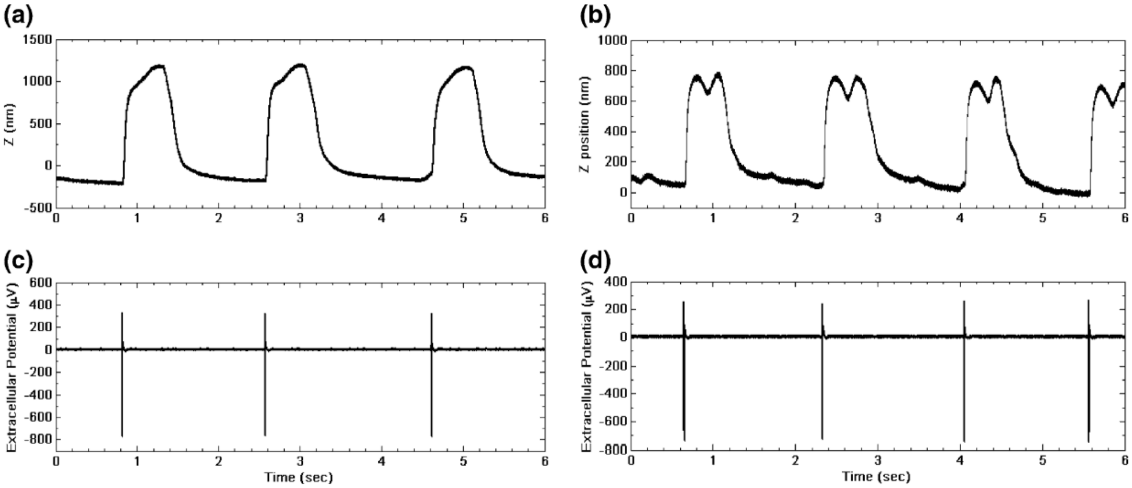

Figure 4–8: **Simultaneous mechanical and electrical recordings from cardiomyocytes.** Recordings taken from two different cardiomyocytes, (a,c) and (b,d), after 3 days in-vitro. **(a,b)** AFM deflections corresponding to mechanical deflections of the cardiomyocytes. The AFM tip was kept in contact with the cell by applying a constant force of 0.5 $nN$. **(c,d)** Electrical signals of the cardiomyocytes measured by the MEA. This figure was obtained with permission from *A new integrated system combining atomic force microscopy and micro-electrode array for measuring the mechanical properties of living cardiac myocytes by J. Cogollo. et al., 2011, Biomedical Microdevices, 13(4):613–621, Copyright © 2011, Springer Nature.*

## 4.3 Development of the AFM and CMOS-HDMEA integrated setup

Motivated by the AFM-MEA set up to perform simultaneous mechanical and electrical measurements on electrogenic cardiomyocytes, we were inspired to build a similar set up, utilising the commercial AFM and CMOS-HDMEA available to our lab. This combined AFM and CMOS-HDMEA set up would, with hope, be used to study neurons in the near future.

### 4.3.1 Proposed setup

For this project, we attempted to combine the Bioscope II AFM (Veeco, Plainview, NY, USA) with the CMOS-HDMEA featuring 11,011 microelectrodes (Department of Biosystems Science and Engineering of Eidgenössische Technische Hochschule (ETH) Zürich, Switzerland). An illustration of the proposed combined AFM and CMOS-HDMEA set up is shown in Figure 4–9. Electrogenic cells, such as neurons, would be cultured directly on the active surface of the CMOS-HDMEA. From there, the MEAs would record spontaneous activity of the cells, or be used to send a voltage pulse to the cell to incite depolarisation of the cell and subsequently record the electrical responses of the cell. The AFM would then be positioned on top of the cell membrane of interest. The cantilever would reflect intrinsic mechanical responses of the cell during signalling, or could be used to apply calculated forces to the cell.

There are plenty of experiments that one could perform with the high sensitivity, spatial, and temporal resolution capabilities of the AFM and CMOS-HDMEA set up. Some ideas for the types of experiments that one could possibly achieve with this AFM and CMOS-HDMEA set up include:

- quantifying the membrane displacement of the cell during AP signalling, and relating the displacement results with changes in the cytoskeletal structure of the cell if possible.

- measuring the changes in the elastic modulus of the cell during an action potential event, which could provide us with a clue of the structural changes that occur in the cell during such an event.

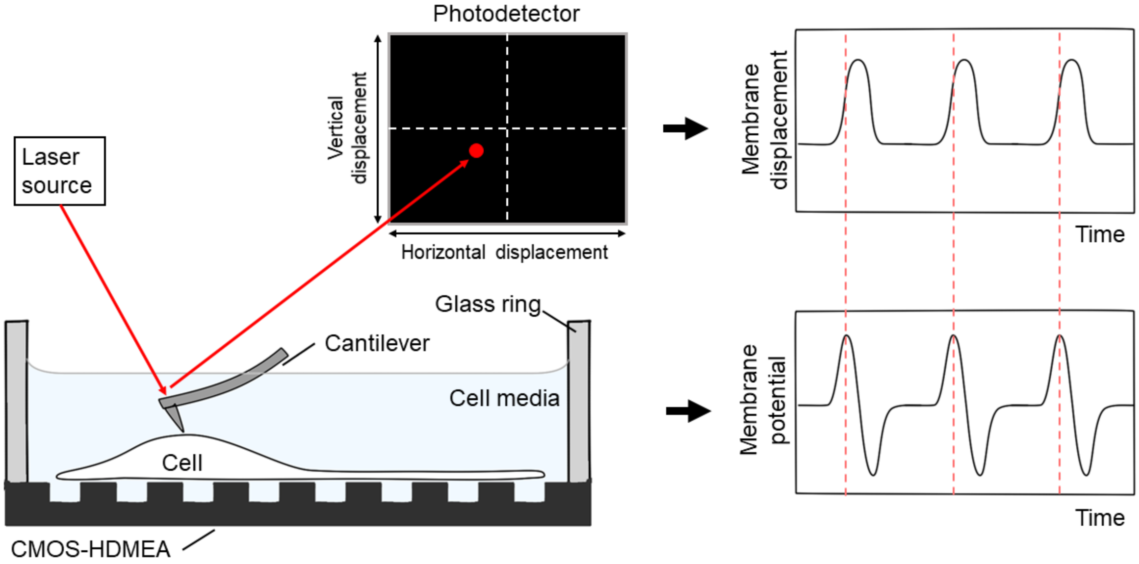

Figure 4–9: **Proposed AFM and CMOS-HDMEA set up.** Electrogenic cells are cultured on the surface of the CMOS-HDMEA. Voltage stimulation and electrical activity from the cells can be recorded through the microelectrodes. The AFM cantilever, positioned on top of the cell, detects mechanical responses of the cell. Results of the membrane displacement and membrane potential can be compared and analysed post recording.

- measuring the effects that compressive forces have on the electrical activity of the cell. This experiment could provide one with an indication of the implications of physical damage to the nerve on neuronal signalling (e.g. in the case of a brain concussion), as well as information about the physical limitations of neurons before the cell loses proper functionality.

- measuring the evolution of electrical signals as a neurite is being extended by using the AFM tip. This experiment would only be made possible by the high density MEAs which allow the signals from the entire length of the neuron and neurite to be recorded from. Additionally, one can verify the functionality and perhaps inherent structure of the extended neurite by analysing the quality of signals passing through that extension.

- studying the effects that drugs have on the mechanical and electrical responses of cells.

- studying synapse related neurodegenerative diseases.

The main improvement of this AFM and CMOS-HDMEA set up would be the drastic increase in number of electrodes on the MEA, when compared to the 60-electrode MEAs that Cogollo and Tian used for their AFM-MEA set up. Only with a HDMEA, would one be able to measure electrical signals from multiple positions along the axon, or from multiple cells at once, a measurement that would have been impossible with Cogollo and Tian's AFM-MEA set up.

For the rest of this thesis chapter, detailed steps pertaining to the AFM and CMOS-HDMEA set up will be discussed.

### 4.3.2 Challenge I: Geometrical incompatibilities

While the concept of combining these two machines is seemingly straight-forward, several complications and challenges did not fail to present themselves in this journey.

Figure 4–10 (a) shows the initial AFM and CMOS-HDMEA configuration. There was not much room for manoeuvring considering the individual designs of the AFM stage and CMOS-HDMEA set up. Once the AFM head was secured and positioned

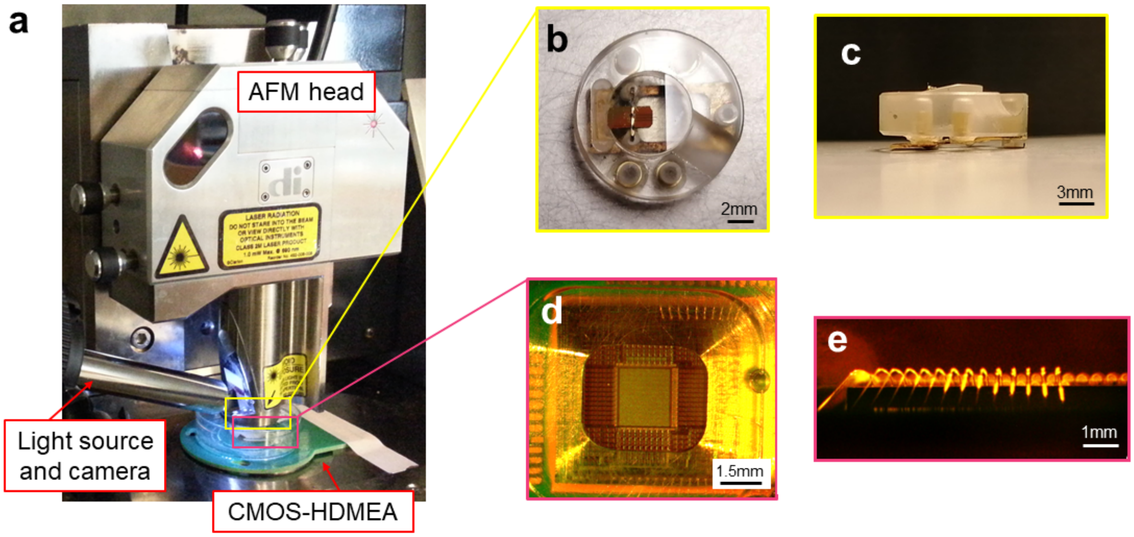

Figure 4–10: **Geometrical incompatibilities of the AFM and CMOS-HDMEA set up. a.** Image of the AFM and CMOS-HDMEA set up. **b.** Close up of the AFM cantilever holder from the top. **c.** Side view of the AFM cantilever holder. **d.** Close up of the CMOS-HDMEA active surface area from the top. **e.** Side view of the bond wires surrounding the active CMOS-HDMEA area. From observations of the side profiles of the AFM cantilever holder and the CMOS-HDMEA, the main challenge arises from trying to fit the flat AFM cantilever holder to the relatively narrow and deep well of the CMOS-HDMEA.

on top of the CMOS-HDMEA, we found out shortly after that it was impossible for the AFM to descent sufficiently and make contact with the active MEA surface. Upon further investigation on the architecture of the devices, we find stark differences between the AFM cantilever holder and the packaged CMOS-HDMEA. From Figure 4–10 (b,c), the AFM cantilever holder is relatively wide and flat, understandably so, as the surfaces being probed using the AFM are usually 'flat'. From the close up images, we see that the cantilever holder itself is a circular block, measuring $\approx 12.7$ *mm* in diameter. The main feature of this cantilever holder is the raised angled platform, where the actual cantilever is clamped into position. This angled platform is $\approx 0.8$ *mm* in height, and measures $\approx 6.35$ *mm* in diameter. Looking at the close up images of the packaged CMOS-HDMEA in Figure 4–10 (d,e), the well of the packaged chip is relatively small and deep. The opening of the active MEA area measures 3 x 3 $mm^2$, a small opening to reduce the eventuality of liquid leakage and electrical shortening of the CMOS chip. Additionally, the bond wires surrounding the active MEA area are $\approx 0.3$ *mm* in height, when measured from the surface of the MEA platform, implying that the epoxy layer has to be at least above the height of the bond wires.

The original designs of the AFM cantilever holder and packaged CMOS-HDMEA result in an impossible configuration for the cantilever to descend low enough to the surface of the active MEA area.

#### 4.3.2.1 Modified chip packaging protocol, Version 1

The first solution to improving the clearance between the AFM cantilever holder and the CMOS-HDMEA was to improve the chip packaging protocol. During the CMOS chip packaging, a bio-compatible PDMS stamp is placed on the active MEA surface to keep the active microelectrode area clear of epoxy (Figure 4–11 (a,d)). The epoxy well, basically, takes after the shape of the PDMS stamp.

Step one in the process of improving the geometrical clearance was to lower the depth of the epoxy well by reducing the amount of epoxy used for the packaging. The height of the PDMS stamp governs the depth of the well, since surface tension of the uncured epoxy (i.e. in liquid form) tends to wrap around the walls of the PDMS stamp. Therefore, the new PDMS stamp design had a fixed height of 0.5 *mm*, with the intention to minimally cover the height of the bond wires on the MEA

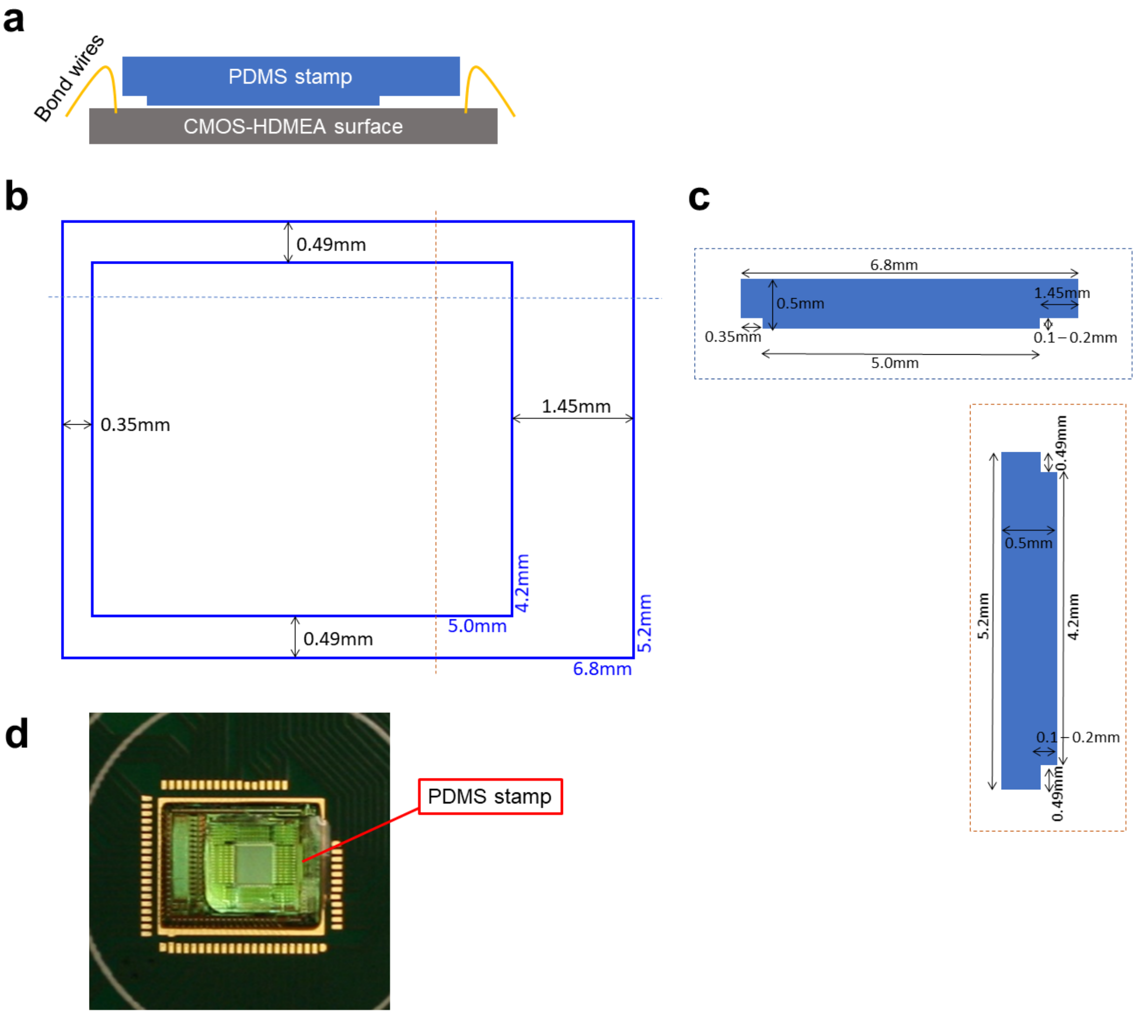

Figure 4–11: **PDMS stamp dimensions a.** Schematic of the PDMS stamp placement on the CMOS-HDMEA surface. The PDMS stamp was designed to have an opening that is as wide as possible at the surface of the MEA, and a low enough height to reduce the overall depth of the epoxy well but high enough to cover the exposed bond wires. **b.** Dimensions of the PDMS stamp from the top. **c.** Dimensions of the PDMS stamp from two side profiles. **d.** Image of the PDMS stamp on a CMOS-HDMEA chip.

Figure 4–12: **CMOS-HDMEA damage. a.** Images showing water marks on the bond pads of the CMOS-HDMEA. This occurrence happens when the epoxy coverage lifts and creates a tiny gap for water to seep to the bond pads and bond wires, which should otherwise be protected from liquid. **b.** Further indication of damage on the microelectrodes.

surface. The second step of the process involved expanding the area surrounding the active MEA surface from previously measured 3 x 3 $mm^2$ to 5.0 x 5.2 $mm^2$. The expanded area would provide more space for the round AFM cantilever holder to descend closer towards the surface of the active MEA area, in addition to providing more leeway for the AFM manoeuvrability. Full dimensions of the PDMS stamp can be found in Figure 4–11 (b,c).

The PDMS stamp solution was short-lived as the CMOS chips kept facing electrolysis. The problem was later alluded to the opening of the active MEA area being too wide. As a result, exposed bond pads that should otherwise be covered were damaged by exposure to the cell medium, resulting in electrical damage and death of the CMOS chip (Figure 4–12 (a)). Instead of redesigning and re-machining the PDMS stamp template (a process with an average of 6 months wait period), we experimented with a quick and easy way of modifying the existing PDMS stamps by cutting the edges of the stamp by hand. This process resulted in PDMS stamps measuring on average 3.0 x 3.5 $mm^2$ with a an unchanged height of 0.5 $mm$. This quick and easy solution proved to be successful at solving the electrolysis problem corresponding to exposed bond pads on-chip.

Concurrently, we were facing a problem with electrolysis of the CMOS chip due to epoxy lift-off, which was related to a separate step in the CMOS-HDMEA packaging protocol. Before bio-compatible epoxy is poured into the CMOS chip, a ring has to be glued onto the chip to create a containing barrier for the epoxy. The suggested method was to use 35 *mm* coverslip, whereby the glass bottom had been removed, as the epoxy containing barrier. Unfortunately, the lifetime of the CMOS chips was severely shortened due to electrolysis. Identifying the cause of the problem was a challenge, as extra caution had been made to ensure that all the bond pads and wires were completely covered with epoxy. Upon closer inspection of the CMOS-HDMEA chip, we noticed a thin layer of water between the MEA surface and the epoxy layer (Figure 4–12 (a)), and, additionally, physical damage on the microelectrodes itself (Figure 4–12 (b)). Further examination lead us to believe that the source of the problem was the coverslips that we had used as the epoxy containing barrier. Since the bottom of the coverslip was not perfectly flat or flush to the surface of the MEA, this provided an opportunity for a thin layer of air pocket to be trapped during the packaging process. Consequently, uneven thermal expansion of the air pockets, coverslip, and epoxy layer would cause the epoxy to lift-off the surface of the MEA, therefore, causing water to seep in and damage the chip. The solution to this challenge was to utilise plastic rings, that were precisely cut, as the epoxy containing barrier. Challenges involving the CMOS chip packaging were solved for the moment. A detailed explaination of the chip packaging process will be explained in (Section 4.3.3.1 and Figure 4–19).

#### 4.3.2.2 Extended cantilevers

Modifying the CMOS-HDMEA packing procedure only alleviated one half of the challenge with respect to geometrical limitations of the combined AFM and CMOS-HDMEA set up. Lowering of the MEA well was still insufficient for the AFM cantilever to make contact with the surface of the MEA. At this point, the only other modification that could be made was on the side of the AFM. Proposed by fellow lab mate, Matt Rigby, the cantilever substrate could be ‘extended’ or made longer (in the z-axis) by stacking several cantilever substrates together.

In order to understand this process, detailed illustrations are provided in Figure 4–13. Under ordinary circumstances, the cantilever is positioned and mounted on the cantilever holder as shown in Figure 4–13 (a). A spring loaded clamp holds the cantilever firmly in place. As can be observed from the illustration (not to scale) and recalling the dimensions of the cantilever holder, the dimensions where the cantilever

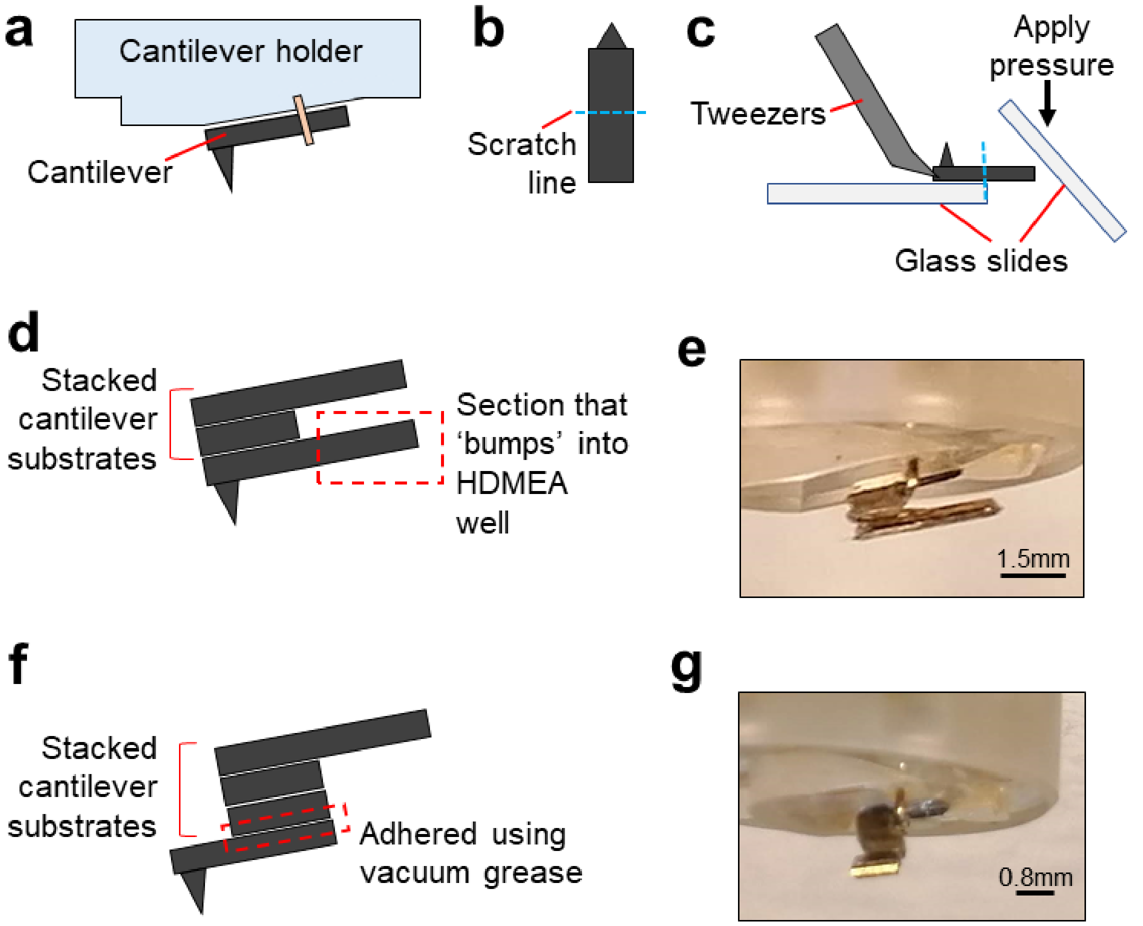

Figure 4–13: **Extended cantilever.** **a.** Illustration of where the AFM cantilever is positioned and clamped on the cantilever holder. **b.** Location of where the scratch line would be made on the cantilever using a diamond scratch pen. **c.** Two glass slides are used to break off the excess cantilever substrate, while a pair of tweezers is used to secure the AFM cantilever during the process. **d.** Illustration of the first prototype of extended cantilevers. Cantilever substrates are stacked and glued atop the AFM cantilever to be used. The red box shows the section of the cantilever substrate that 'bumps' into the sides of the CMOS-HDMEA well. **e.** Image of the first prototype of extended cantilever mounted on the cantilever holder. **f.** Illustration of the second and third prototype of extended cantilevers. The stacked cantilever substrates are significantly shorter and shifted away from the tip of the cantilever, to allow for more room for the AFM laser pathway. The back end of the cantilever substrate of the AFM cantilever to be used was also broken off to avoid 'bumping' into the sides of the CMOS-HDMEA well. In the second prototype, all the cantilever substrates were adhered by glue, thus, switching AFM cantilevers was impossible. In the third prototype, the AFM cantilever to be used was adhered using vacuum grease, therefore, allowing the AFM cantilevers to be switched out whenever necessary. **g.** Image of the second and third extended cantilever prototype mounted on the cantilever holder.

is held is rather wide and flat. As a result of this feature, the AFM cantilever is unable to physically lower itself any closer to the MEA surface. There were two approaches to this problem; firstly by manufacturing a new cantilever holder that is in agreement with the dimensions of the MEA well, and secondly by modifying the cantilevers that we use. As the former option would be costly time-wise and financially, the latter option was what we opted for, owing to the fact that the only materials required were a dash of creativity and the materials that we already had at our disposal.

The process of constructing an extended cantilever was straightforward. Cantilever substrates would first be marked and scratched using a diamond scratch pen (Figure 4–13 (b)). The cantilever substrates were then snapped off using glass slides, while a pair of tweezers held the section with the AFM tip in place (Figure 4–13 (c)).

The first prototype of extended cantilever is shown in Figure 4–13 (d,e). The cantilever involves stacking several cantilever substrates that are held together with a strong adhesive (e.g. Loctite 454 Instant Adhesive, Henkel Adhesives Technologies, Canada). The stacked cantilevers provided an additional $\approx 1\ mm$ extra vertical height to the cantilever. The extended cantilever, being smaller and narrower (i.e. measuring 3.5 x 1.5 $mm^2$ in length and width) than the cantilever holder with the added vertical height, enabled the cantilever tip to descend all the way to the surface of the MEA. Modifications to the cantilever substrate removed most of the geometrical incompatibilities, however, this solution was still flawed. The two problems that stood out were; 1. the stacked cantilever substrate got in the way of the AFM laser pathway, and 2. the AFM could not access half of the active MEA area as the back of the cantilever substrate kept colliding with the wall of the HDMEA (red box in Figure 4–13 (d)). Not being able to align the laser on the cantilever tip rendered the AFM useless, while not having access to more than half of the active MEA area meant that the effective working range has been drastically limited.

With those two new challenges at hand, the second extended cantilever prototype was developed, and is shown in Figure 4–13 (f,g). This time, the cantilever substrates were significantly shorter and positioned away from the cantilever tip. In doing so, the AFM was able to scan the entire MEA area without restrain, and the AFM laser pathway was not obstructed. However, utilising a super adhesive for the extended cantilever meant that the cantilever to be used is fixed permanently to the cantilever substrate. As a result, minor adjustments in the position of the cantilever

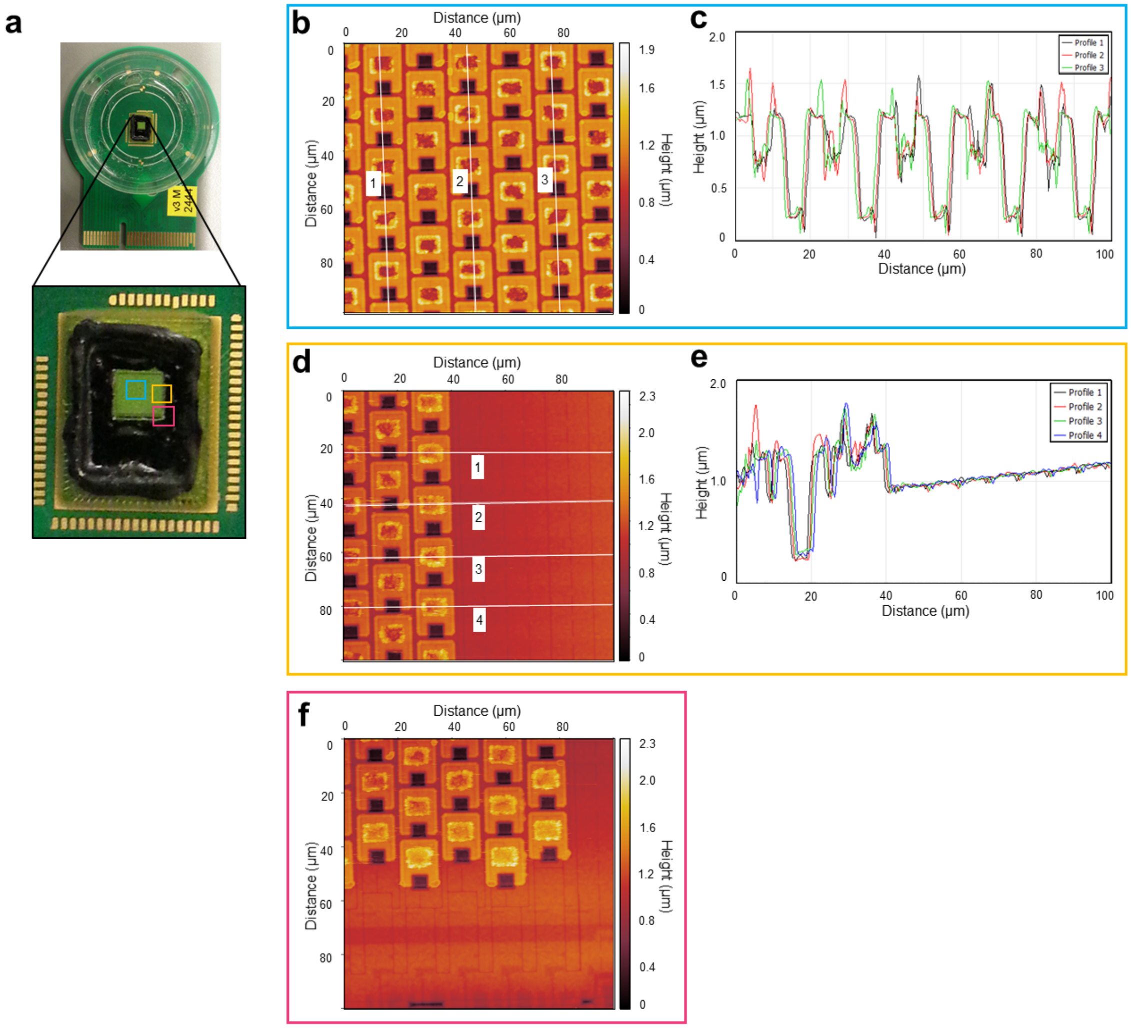

Figure 4–14: **AFM topography of the CMOS-HDMEA surface using the extended cantilever. a.** Close up image of the scan areas on the CMOS-HDMEA; middle scan (blue), side scan (orange), and edge scan (pink). **b.** Topography image of the middle of the active MEA area. **c.** Line traces of the topography scan, highlighting the features of the microelectrodes. **d.** Topography image of the side of the active MEA area. **e.** Line traces of the topography scan, capturing the microelectrodes and the flat MEA substrate. **f.** Topography image of the edge of the active MEA area, proving the accessibility of the AFM cantilever on the active sensing area of the CMOS-HDMEA.

that had to be made in order to focus the laser on the cantilever tip, or changing out a worn out cantilever tip, became impossible without having to take apart or remake the entire set up. In short, the extended cantilever solution is not yet perfect, and a better solution had to be thought of.

The third prototype was made identical to the second prototype, with only one change. The cantilever to be used was adhered to the extended cantilever substrate using vacuum grease, instead of super adhesive (red box in Figure 4–13 (f)). A small amount of vacuum grease allowed the cantilever to be secured to the stacked substrate, and allowed the cantilever position to be adjusted or to be switched out freely.

To confirm that the extended cantilever functions as intended, several AFM topography scans were performed on different locations on the active MEA area. The locations of the scans are presented in Figure 4–14 (a). The AFM successfully scanned the middle (Figure 4–14 (b,c)), side (Figure 4–14 (d,e)), and bottom edge that was previously inaccessible (Figure 4–14 (f)). Along with the topographic images, are the line traces reflecting the features of the microelectrodes and surface of the MEA. The AFM images conclude that both lowering the wells of the CMOS-HDMEA and extending the cantilever substrate solved the geometrical incompatibilities of the AFM and CMOS-HDMEA set up.

#### 4.3.2.3 Extended tip cantilevers

*Is there a better solution?*

Inspired by former lab member, Lynda Cockins, who fabricated a high-aspect ratio metal tip by attaching a metal wire to the cantilever [Cockins et al., 2007], we thought that it might be a good idea to explore alternatives to the extended cantilever idea. The idea behind the extended tip cantilever was to keep the AFM configuration the same but achieve the vertical height extension through the increased length of cantilever tip. Instead of attaching a metal wire, an electrically inert and sharp glass pipette tip would be used, for reasons that will be explained later in this chapter. There are several reasons why this might be the preferred method. Firstly, keeping the AFM configuration the same avoids problems with tip and laser alignment. The AFM laser pathway is set and is focused at a specific distance on the cantilever holder (*Disclaimer: This statement was made with regards solely to the commercial Bioscope II AFM. It may not be applicable to other AFM machines.*). Therefore, when the tip of the cantilever is shifted from the focus point of the laser, as in the case of the extended cantilevers, the intensity of the laser reduces significantly. The extended tip cantilever avoids that problem altogether since the cantilever is mounted on the cantilever holder as intended by the manufacturer. Secondly, extending the cantilever tip meant that the AFM has the freedom to probe any corner of the MEA surface, since the cantilever tip is narrow and takes up significantly less space than a cantilever substrate.

An illustration of the extended tip cantilever mounted on a cantilever is shown in Figure 4–15 (a). Firstly, the glass pipettes are made using a pipette puller, to form long and thin pipette tips. After that, the glass pipette tips are isolated using the set up shown in Figure 4–15 (b). The glass pipette is placed on a glass slide, and the tip of the pipette is secured with a piece of wet paper. Using a razor blade, pressure is applied at the break off point, to break the glass pipette. The wet piece of paper secures the pipette tip well, through surface tension of water, and prevents the small and fragile glass tip from 'flying away' during the breaking process. Following that, the glass slide with the pipette tip is secured to one of the micromanipulators in Figure 4–15 (d). Two micromanipulators and a camera are used to align and attach the glass pipette tip to the cantilever. The AFM cantilever is mounted on a cantilever holder that is attached to the second micromanipulator. Once the cantilever tip and glass pipette tip positions are roughly aligned, a droplet of super adhesive is placed on the flat end of the glass pipette tip. After which, the cantilever tip is aligned and lowered to make contact with the glass pipette tip. Further adjustments are made before the wet paper towel is carefully removed using a pair of tweezers. The view from the top of the cantilever as seen from the camera is shown in Figure 4–15 (e). It is easy to see that the glass pipette tip is attached to the cantilever at the centre. Side view of the extended tip cantilever detaching from the glass slide is shown in Figure 4–15 (f), and the finished product in Figure 4–15 (g). The glass pipette tip hangs at a 90° from the tip of the cantilever due to gravity.

While this solution appeared to be promising, the success rate of of making one of these cantilevers was low. For one, the glass pipette tips are extremely small and the breakage point of the glass pipette is not always perfectly flat. Not having a flat surface to work with causes the cantilever tip to be attached at an angle, that is not

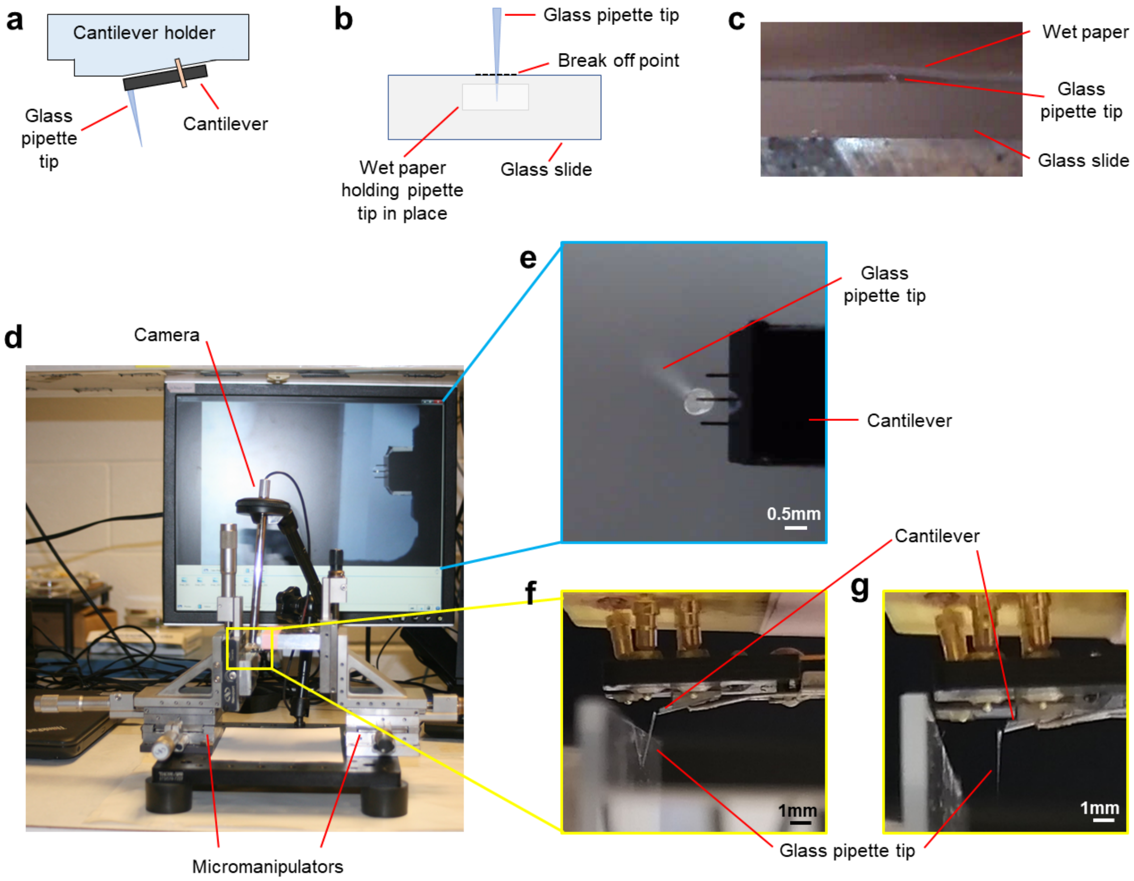

Figure 4–15: **Extended tip cantilever.** **a.** Illustration of the cantilever mounted on the cantilever holder. A glass pipette is attached to the tip of the AFM cantilever. **b.** Breaking the tip of the glass pipette. The tip of the glass pipette is placed on the glass slide and secured with a piece of wet paper. Using a razor blade, the pipette is broken off at the break off point shown. **c.** Image of the glass pipette after being broken off. The wet paper secures the pipette tip from 'flying away' during the break off process. Besides that, the wet paper is easily removed once the cantilever tip has been secured to the pipette tip. **d.** Image showing the tools used to make the extended tip cantilever. Two micromanipulators are used; one to mount the AFM cantilever and move the cantilever tip towards the glass pipette, and one to move the glass pipette tip. A camera is used to aid with visualising and aligning the cantilever tip and pipette tip. **e.** Image of the cantilever after attaching the glass pipette tip to the middle cantilever. With the help of gravity, the pipette tip falls downwards at approximately 90° from the surface of the cantilever. **f.** Side view image showing the glass pipette tip about to be released from the glass slide. **g.** Side view image of the finished extended tip cantilever.

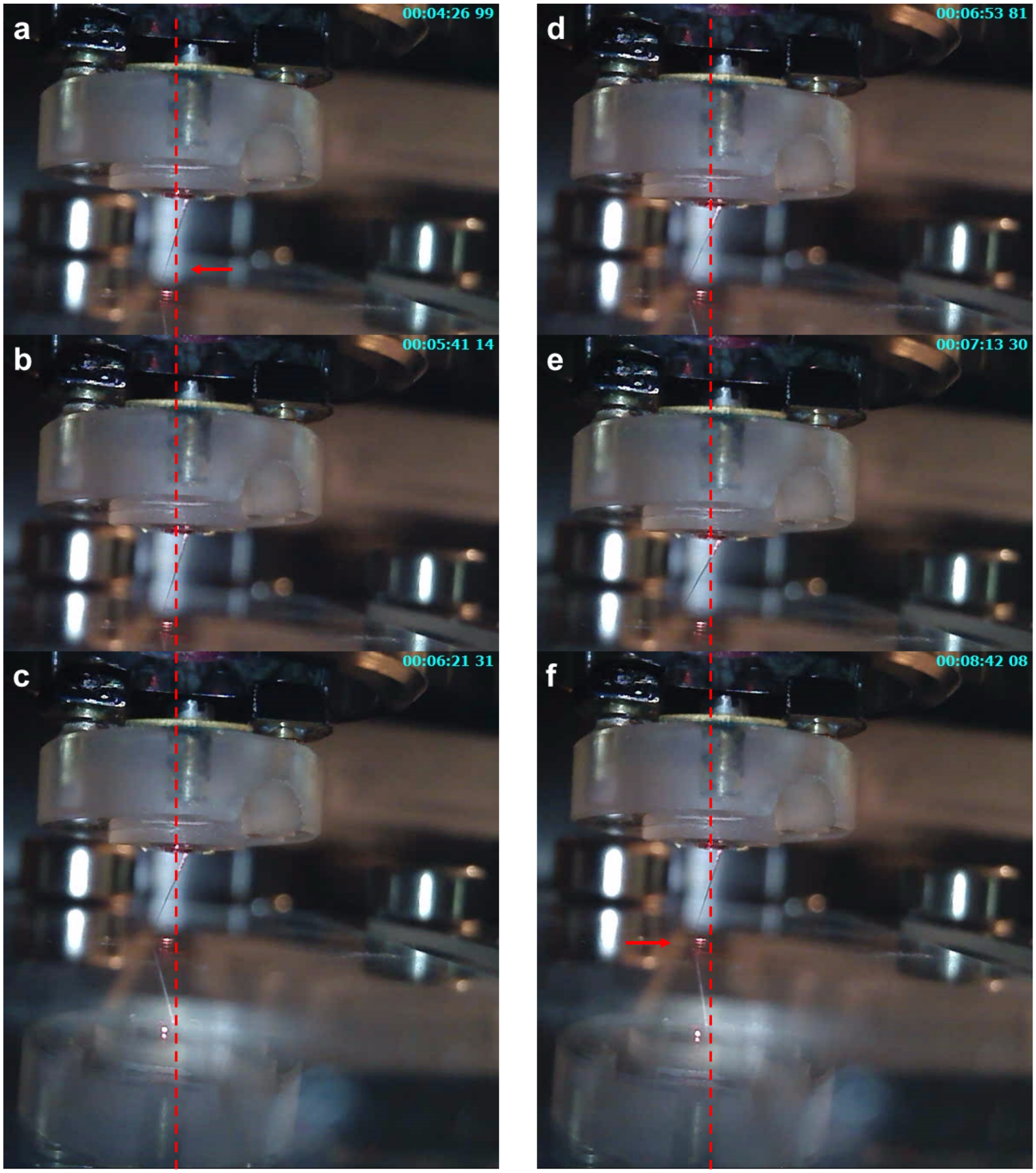

Figure 4–16: **Extended tip cantilever descending on a glass slide.** Sequential images of the AFM approaching the surface of a glass slide, in order from **(a-f)**. As the AFM head pushes the extended tip cantilever lower onto the surface, the tip is seen to slide to the left **(a-e)**. As the AFM head is raised, the tip slides back to the right **(f)**. Time stamps of the images are shown in blue on the top right corner of each image.

perpendicular to the cantilever tip, therefore, rendering the cantilever impractical. A solution to this problem was to flatten off the edge of the glass pipette by sanding it down, however, the glass pipette was too small and fragile. Any additional handling and manipulation lead to the destruction of the pipette tip itself. Nevertheless, there were a few successful attempts, and we decided to test them out. Figure 4–16 shows a series of images taken of an extended cantilever attempting to make contact with the surface of a glass slide. From the images, the cantilever tip is seen to slide to the side as the AFM head gradually lowers itself (Figure 4–16 (a-e)). The cantilever tip slides back into position as the AFM head is gradually lifted off the surface Figure 4–16 (f)). This incident was thought to be due to torque on the tip, leading to sideways deflection.

In the end, the extended tip cantilever was deemed impractical to increase the vertical height of the AFM cantilever space. The better solution ended up being utilising the extended cantilever substrate.

#### 4.3.2.4 Extension cable

Solving the geometrical clearance problem between the AFM and the CMOS-HDMEA was just one part of this journey. We now had to figure out the optimal position for both the AFM and CMOS-HDMEA on the AFM stage. Recalling the set up for the CMOS-HDMEA, the CMOS chip has to be plugged into a custom-printed circuit board, which is then connected through a low-voltage differential signalling (LVDS) cable to the FPGA board. However, based on the current design of the Bioscope AFM stage, the custom-printed circuit board does not fit the tight space beneath the AFM head. In order to alleviate that problem, an extension cable had to be made to allow the CMOS chip to be connected to the custom-printed circuit board that is placed at the corner of the AFM stage. This extension cable was made by connecting two custom-printed peripheral component interconnect express (PCIE) board with connecting wires, shown in Figure 4–17 (a,b). The AFM and CMOS-HDMEA set up including the extension cable connecting the additional CMOS-HDMEA circuitry is shown in Figure 4–17 (c,d). The extension cable accomplished its goal of creating more room for the placement of the CMOS chip beneath the AFM head while maintaining connectivity and functionality of the CMOS chip itself. Besides that, the flexible nature of the connecting cable meant that mechanical vibrations on the

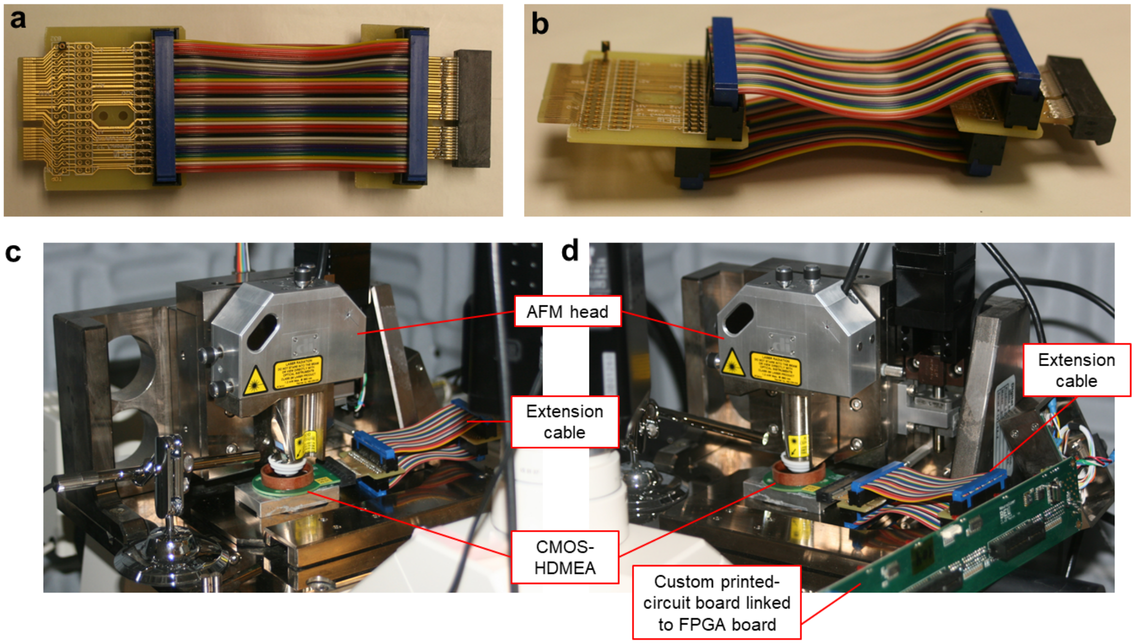

Figure 4–17: **Extension cable for the AFM and CMOS-HDMEA set up. (a,b)** Top and side profile of the extension cable. The extension cable was made by connecting two custom-printed PCIE boards with connecting wires. **(c,d)** Images of the AFM and CMOS-HDMEA set up, with the extension cable connecting the CMOS chip to another custom-printed circuit board which connects to the FPGA board through a LVDS link.

AFM stage would not be picked up by custom-printed circuit board, and would not be translated into noise in the MEA recordings.

### 4.3.3 Challenge II: Noise

While challenges with geometrical incompatibilities of the AFM and CMOS-HDMEA set up have been resolved, we had yet to test the functionality of the combined set up together. The next few sections detail the process of identifying the different sources of noise and the approaches to eliminate them.

#### 4.3.3.1 Modified chip packaging protocol, Version 2

The first noise source measured by the CMOS-HDMEA originated from the AFM laser. The laser beam, used to reflect off the back of the tip of the cantilever, seemed to interfere strongly with the signals recorded by the microelectrodes. Owing to the sensitivity of the transistors of the CMOS chip, the slightest exposure to light contributes to added noise in the signals recorded. In the case of the AFM, the high intensity laser beam oversaturates the transistors and consequently drives the signals out of the recording range of the microelectrodes. As such, null signals are observed and recorded (Figure 4–18 (a)).

Initially, we attempted to recover the 'lost' signals by subtracting the offset electronically. This method managed to recover signals from several microelectrodes, however, most of the microelectrodes stayed the same in reporting null signals (Figure 4–18 (b)). Moreover, the signals that were recovered often showed an increase in noise level and periodic noise fluctuations that could be directly linked to the AFM laser. This was not a good sign and we had to find a better solution.

Remembering that CMOS transistors are light-sensitive, the idea to cover the on-chip circuitry, apart from the microelectrodes, came to mind. Using a black Sharpie marker on hand, the area surrounding the microelectrodes were 'blacked out', as a quick and easy makeshift solution. And, much to our delight, the Sharpie marks did the trick of returning all the signals on the CMOS-HDMEA to 'normal'. Evidently, a more robust and permanent solution had to be developed. One of the main reasons being, Sharpie marks are not permanent and they dissolve in liquid over time to release toxic substances that will kill cultured cells. For this, an opaque and bio-compatible epoxy (Epotek 320, Epoxy Technology Inc., MA) was opted for as a cover for the region surrounding the microelectrodes. Figure 4–18 (c) shows the MEA area after application of the epoxy. Since the amplifiers are located very closely to the microelectrodes and to avoid the hassle of designing and manufacturing a PDMS stamp that fits the MEA active area perfectly and that is very shallow, the epoxy layer was applied by hand. Like any form of art, the process is slow in the beginning and the final product does not always turn out great. Nevertheless, with a smidgen of patience and practice, the application process becomes easier. Signals recorded by the microelectrodes after having the surrounding on-chip components covered in epoxy, are presented in Figure 4–18 (d). All of the signals from every microelectrode

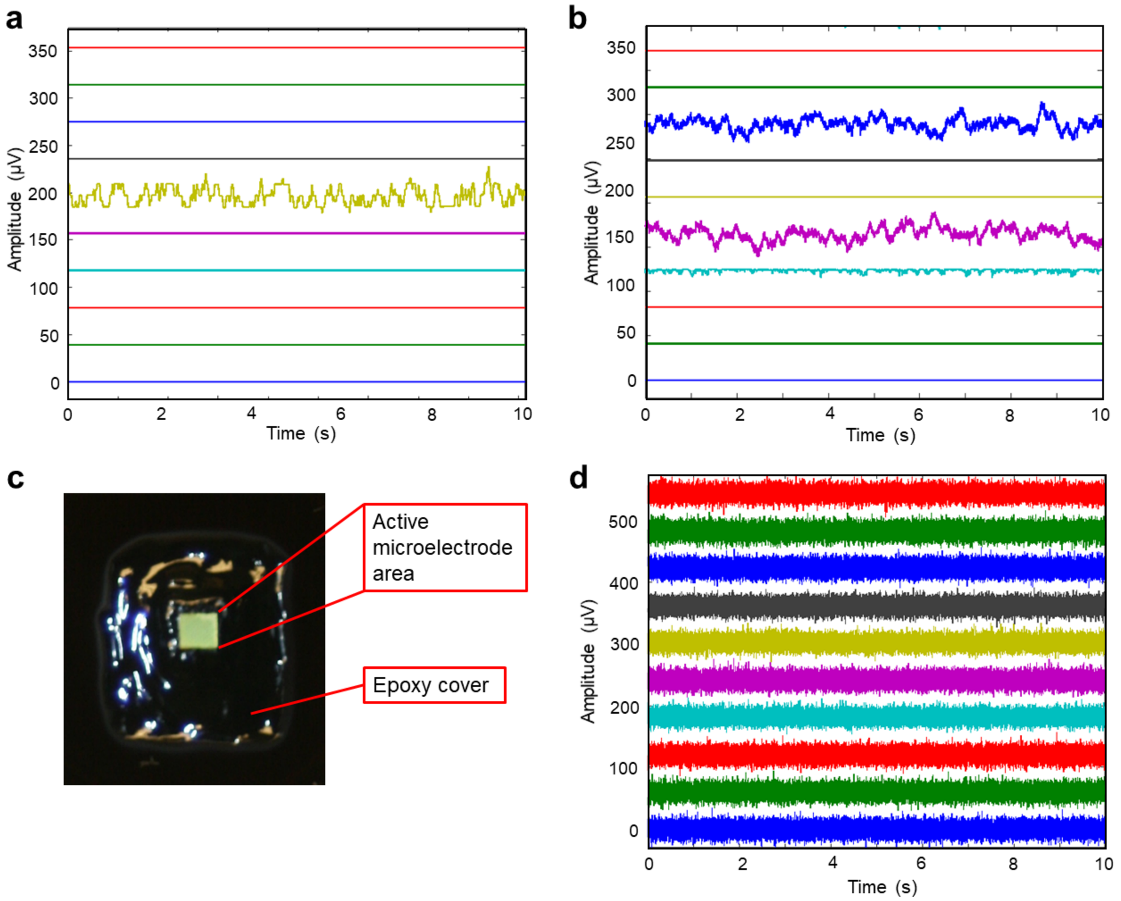

Figure 4–18: **Out of range signals recorded by the CMOS-HDMEA. a.** Signal recordings obtained from the microelectrodes when exposed to the AFM laser. Almost all of the signals were out of range, resulting in the microelectrodes recording null signals. **b.** Signal recordings after attempting to recover the out of range signals, by subtracting the signal offset. Most of the signals were still out of range. **c.** Image showing the covered amplifiers on the MEA surface. A thin and opaque bio-compatible epoxy was painted around the active microelectrode area, to cover all the on-chip electronics from light. **d.** Signal recordings from a chip after covering all the on-chip electrodes except for the active microelectrode sensing area. All of the signals were successfully recovered.

are present with low noise levels, therefore, making the epoxy painting process worth the while.

### Finalised CMOS-HDMEA packaging protocol.

To summarise the modifications that have been made to the CMOS-HDMEA chip packaging protocol, which helped alleviate some geometrical incompatibilities and noise, the complete procedure will be presented here (Figure 4–19). Before proceeding with the following steps, the handler has to be grounded using an anti-static wrist strap, to prevent chip damage by electrostatic discharge.

First, the PDMS stamps (Sylgard 184 Silicone Elastomer, Dow Chemical Company, USA) are made and cured as recommended by the manufacturer. Next, the edges of the PDMS stamps are cut to achieve blocks measuring 3.0 x 3.5 $mm^2$ by 0.5 $mm$ height (Figure 4–19 (a)). At the same time, the unpackaged CMOS-HDMEA chips are cleaned in a plasma $O_2$ asher at $200W$, $200mT$, and $80°C$ with an $O_2$ flow of $20sccm$ for 5 minutes (Figure 4–19 (b)). The plasma treatment not only removes impurities and debris, the process also makes the MEA surface more hydrophilic. Therefore, enabling the PDMS stamp to adhere well to the MEA surface, in the following step (Figure 4–19 (c)). Using a pair of tweezers, the PDMS stamp is gently pressed down to remove any pockets of air bubbles that may have been trapped. Removing the air bubbles is crucial to ensure a tight seal between the PDMS stamp and the MEA surface, to avoid epoxy from leaking into the microelectrodes.

Next, Epotek 353ND-T (Epoxy Technology Inc., MA) is piped around the edges of the PDMS stamp using a 1 $ml$ syringe with a size 20 syringe needle, and cured according to the manufacturer's instructions (Figure 4–19 (d)). The Epotek 353ND-T ring forms the inner well of the MEA. After curing the epoxy, a 35 $mm$ plastic ring is adhered to the CMOS chip using an adhesive like Loctite 454. Pressure is applied to the entire ring from the top to ensure the ring adheres well and that there are no trapped air bubbles. The plastic ring also serves as the outer epoxy containing barrier (Figure 4–19 (e)). While waiting for the glue to set, Epotek 353ND (Epoxy Technology Inc., MA) is prepared and degassed well in a vacuum chamber. It is crucial to remove as much air bubbles as possible, to avoid uneven thermal expansion during experimentation which could ultimately lead to the epoxy layer lifting off the surface of the MEA again. Using a 10 *ml* syringe with a size 18 syringe needle, the well degassed Epotek 353ND solution is carefully piped into the remaining area of the MEA (Figure 4–19 (f)). At this stage, all the on-chip electronics should be covered well with the epoxy layer. Careful care is taken not to pipe over the Epotek 353ND-T well and the PDMS stamp.

Once the Epotek 353ND has been cured as per manufacturer's instructions, the PDMS stamp is carefully removed with a pair of tweezers. Extra caution is made to avoid scratching or damaging the MEA surface with the tweezers. Finally, Epotek 320 (Epoxy Technology Inc., MA) is prepared to cover the remaining on-chip electronics surrounding the active microelectrode sensing area. This application process is performed under a standard dissection microscope. With a toothpick and a pulled pipette (for finer lines), the Epotek 320 is carefully painted onto the chip. A thin layer is spread over the Epotek 353ND-T well to create an extra barrier against liquid leakages into the chip. Once the MEA surface looks as shown in (Figure 4–19 (g)), the chip is once again cured according to manufacturer's instructions and is ready for the next phase of chip testing.

It is critical that each step be taken seriously and perfected, as one fault will lead to the demise of the CMOS chip and eventually failure of the experiment.

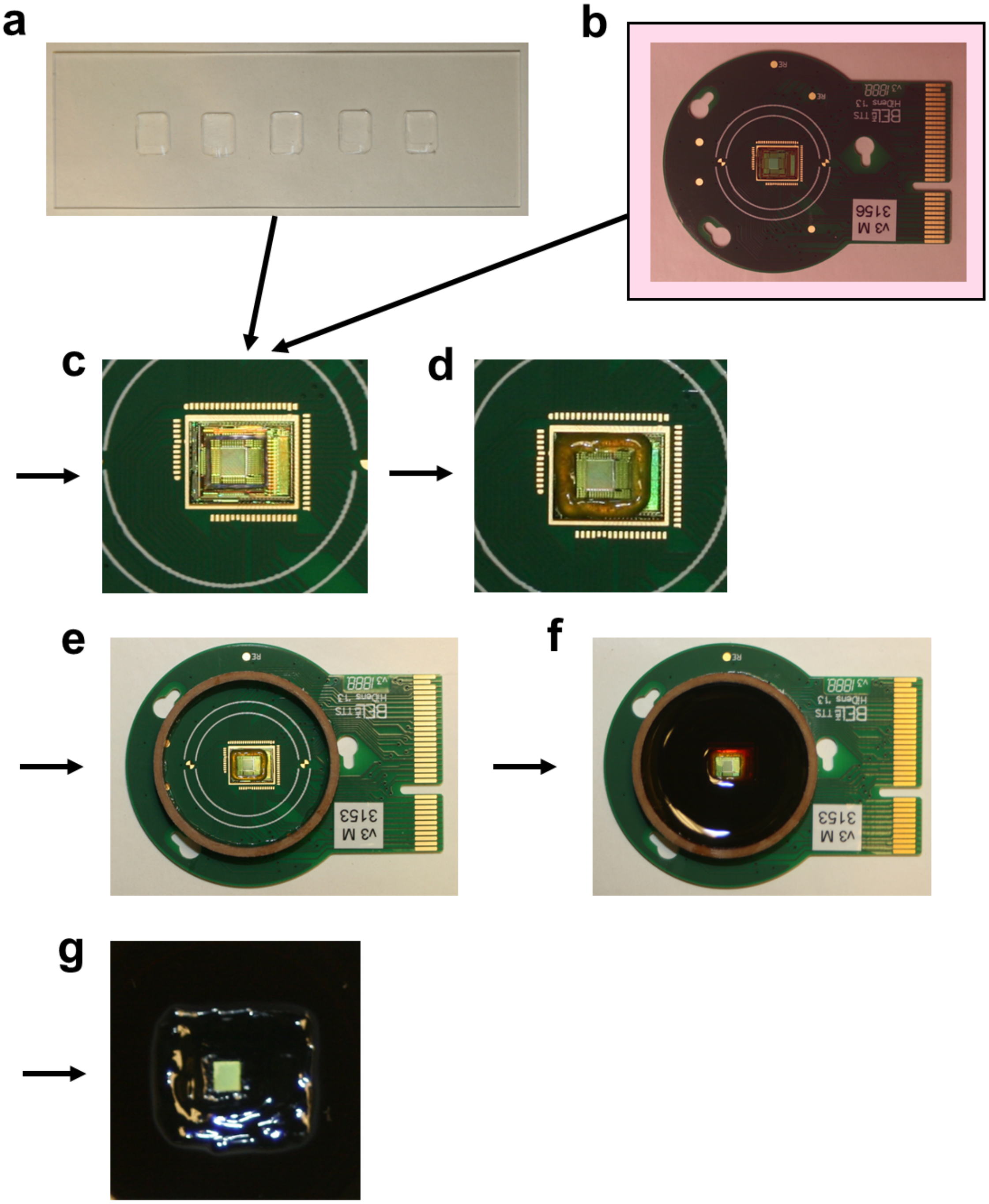

Figure 4–19: **CMOS-HDMEA packaging protocol.**

Figure 4–19: **CMOS-HDMEA packaging protocol.*****(continuation)*** **a.** PDMS stamps that were prepared and trimmed to shape. **b.** Cleaning of the CMOS chip in a plasma $O_2$ asher. **c.** PDMS stamp is placed on top of the active microelectrode sensing area. The PDMS stamps were pressed down firmly to remove air bubbles. **d.** Epotek 353ND-T is piped around the PDMS stamp using a 1 $ml$ syringe and size 20 syringe needle. The epoxy was cured in the oven as per instructions from the manufacturer. **e.** A plastic ring is glued onto the surface of the chip. This ring forms the epoxy containing barrier. **f.** Once the plastic ring is glued in place, Epotek 353ND is used to fill the surrounding MEA surface using a 10 $ml$ syringe with a size 18 syringe needle. Careful care was taken not to pipe epoxy over the PDMS stamp. The epoxy is cured in the oven as per instructions from the manufacturer. **g.** After curing and once the chip has cooled down to room temperature, the PDMS stamp is removed, with caution to avoid scratching or damaging the MEA surface. Epotek 320 is applied onto the surrounding MEA components. Extra care is taken not to put epoxy over the microelectrodes.

#### 4.3.3.2 Bioscope AFM modification

Owing to the sensitivity and complexity of each device, the combination of the AFM and CMOS-HDMEA generated noise originating from cross-talk between the two systems or ground loops (Figure 4–20 (a)). By process of elimination, one of the components of the Bioscope II AFM, namely the extender module, was generating unexplained noise that was detected by the CMOS-HDMEA. The simplest solution was to disconnect and remove the extender module from the AFM set up. We discovered shortly after that the AFM was rendered inoperable, as the custom circuit boards of the commercial AFM relied on the presence of the extender module to function. Since sourcing for a replacement part from an antiquated microscope was to no avail, we decided to take apart the commercial AFM and run it externally using a Gnome X Scanning Microscopy (GXSM) module. Details of the change can be found in Supplementary Material S5.

Modifying the Bioscope II AFM reduced some of the noise that was observed, however, the ground loop problem was still prevalent. Periodic signals with a frequency of 60 $Hz$ (and higher harmonics) were still being detected by the microelectrodes, implying a grounding problem between the AFM and the CMOS-HDMEA was present. After a series of trial and errors (which will not be detailed here), two

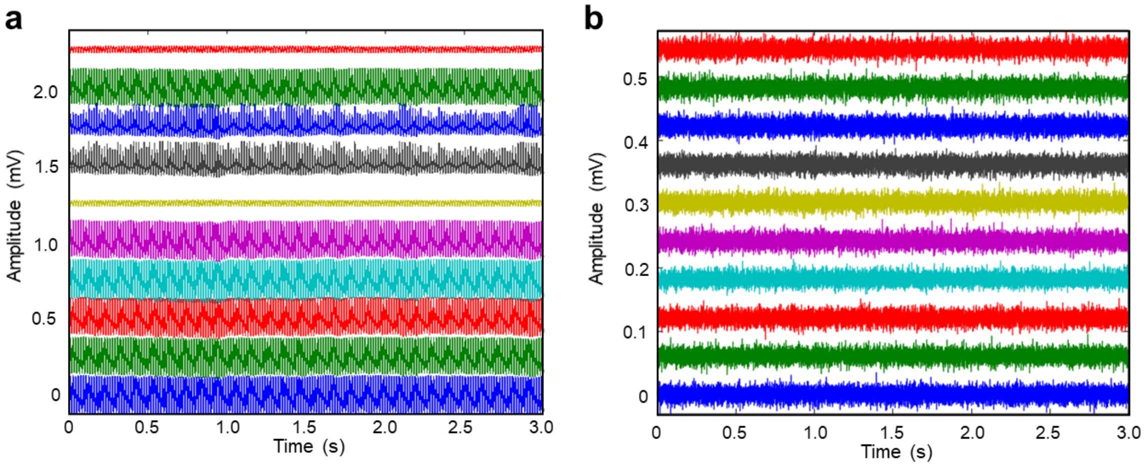

Figure 4–20: **Noise as observed by the CMOS-HDMEA. a.** Signals recorded by the CMOS-HDMEA with the original Bioscope II AFM set up. The noise levels are noticeably high and the periodic nature indicates the prescence of ground loops. **b.** Signals recorded after removing the extender module and switching over to a GXSM run AFM. The noise levels are significantly lower.

solutions that seemed to solve the problem were developed. Firstly, the AFM had to be electrically isolated from the CMOS-HDMEA. This is not a trivial solution as this AFM and CMOS-HDMEA set up is meant to perform experiments on biological cells, which have to be contained in cell media for survival. The cell media is a pool of ions which will conduct electricity. Therefore, non-conducting cantilevers could only be used (i.e. using an inert glass pipette tip instead of a metal wire for the extended tip cantilever). To increase isolation of the AFM system, insulating tape was placed between the AFM head and the cantilever holder, to reduce chances of cross-talk between the systems. Secondly, a silver chloride reference electrode was used to connect the liquid bath in the CMOS-HDMEA to the reference electrode pin connected to the CMOS chip.

These two measures succeeded in reducing the noise problems faced by the combined AFM and CMOS-HDMEA set up, and is shown in Figure 4–20 (b).

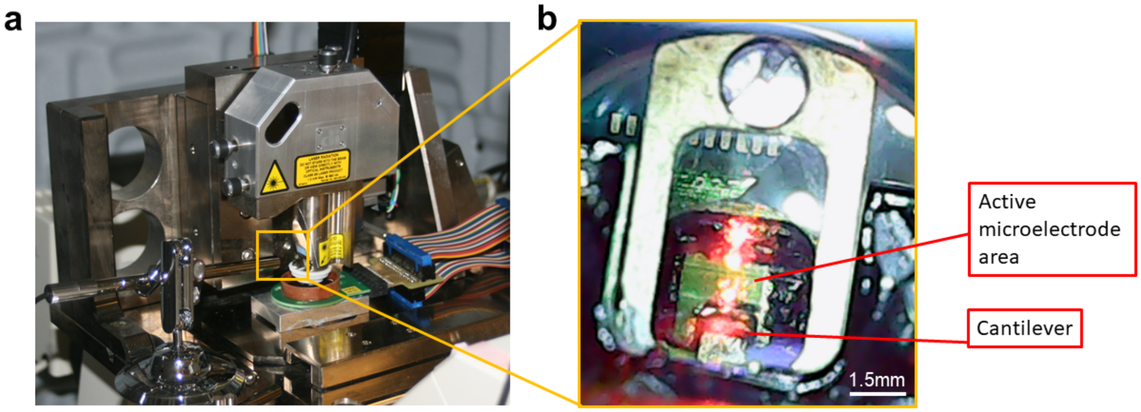

Figure 4–21: **Optical access on the AFM and CMOS-HDMEA set up. a.** Image showing the combined AFM and CMOS-HDMEA set up. A camera is used to view the reflection of the AFM cantilever on the MEA surface. **b.** Image as seen from the camera. The active MEA area is the green square that is surrounded by the black epoxy layer. The cantilever tip is positioned approximately in the centre of the MEA area.

### 4.3.4 Challenge III: Reduced optical access

Now that we have solved the geometrical and noise issues, we have yet one more challenge to tackle. Unlike the MEAs used by Cogollo and Tian [Cogollo et al., 2011, Tian et al., 2017], the CMOS-HDMEAs that we have are not fabricated on a transparent substrate like glass. The densely packed microelectrodes and materials used for fabrication, which allow for low noise and high bandwidth capabilities, make the CMOS-HDMEAs very opaque. Under normal circumstances, an upright microscope would be used to view the MEAs from the top. And in the case of the AFM, an inverted microscope is used to view the cantilever and biological samples from below. By combining these two systems together, we have eliminated any chance of optical access.

*How, then, would one position the AFM cantilever on the MEA?* Lucky for us, the Bioscope II AFM head has a mirror that reflects off onto the top of the cantilever. This mirror is usually used to illuminate the region surrounding the tip of the cantilever. We chanced upon this opportunity by using a camera to transmit images that were reflected off the mirror (Figure 4–21 (a)). The view as seen from the camera is shown in Figure 4–21 (b). We can clearly see the active MEA region, surrounded by the black epoxy layer. Additionally, we can estimate the position of the cantilever tip by looking at the position of the cantilever substrate and the laser spot.

For now, approximating the location of the AFM tip on the MEA is possible. However, these optical images are insufficient for locating smaller structures (such as biological samples, which are also optically transparent) on the MEA surface.

### 4.3.5 AFM and CMOS-HDMEA functionality

*Now, does the combined AFM and CMOS-MEA set up work?*

The finalised combined AFM and CMOS-HDMEA set up is shown in Figure 4–22 (a,b). And, there was only one way to find out if they could function harmoniously with each other. Simultaneous recordings were performed in a phosphate buffer saline solution (Thermo Fisher Scientific, MA, USA) at room temperature. The AFM performed a contact mode topography scan of the surface of the active MEA area, while the microelectrodes performed a block scan recording configurations to capture any spontaneous activity on-chip. The AFM topography image is shown in Figure 4–22 (c). Disregarding the non-linearities that arise from AFM piezoelectric hysteresis, the features of the MEA were well captured. This implies that the AFM has successfully made contact with the microelectrodes and is unaffected by the microelectrodes that are recording right beneath the AFM tip. Signal recordings from the MEA is shown in Figure 4–22 (d). From the results, the noise levels of the electrodes were low and no major activity was detected by the microelectrodes, as expected, since the AFM scan is not inducing any change in current or voltage. There were, however, a few instances where an unexplained noise pattern is seen (e.g. red signal at 200 $\mu V$ in Figure 4–22 (d)). This occurrence is possibly a result of cross-talk from the AFM, which is not surprising, considering the AFM system is not perfectly isolated from the CMOS-HDMEA system.

In the end, yes, the combined AFM and CMOS-HDMEA function together. Needless to say, the full capabilities of this set up have not yet been tested and that

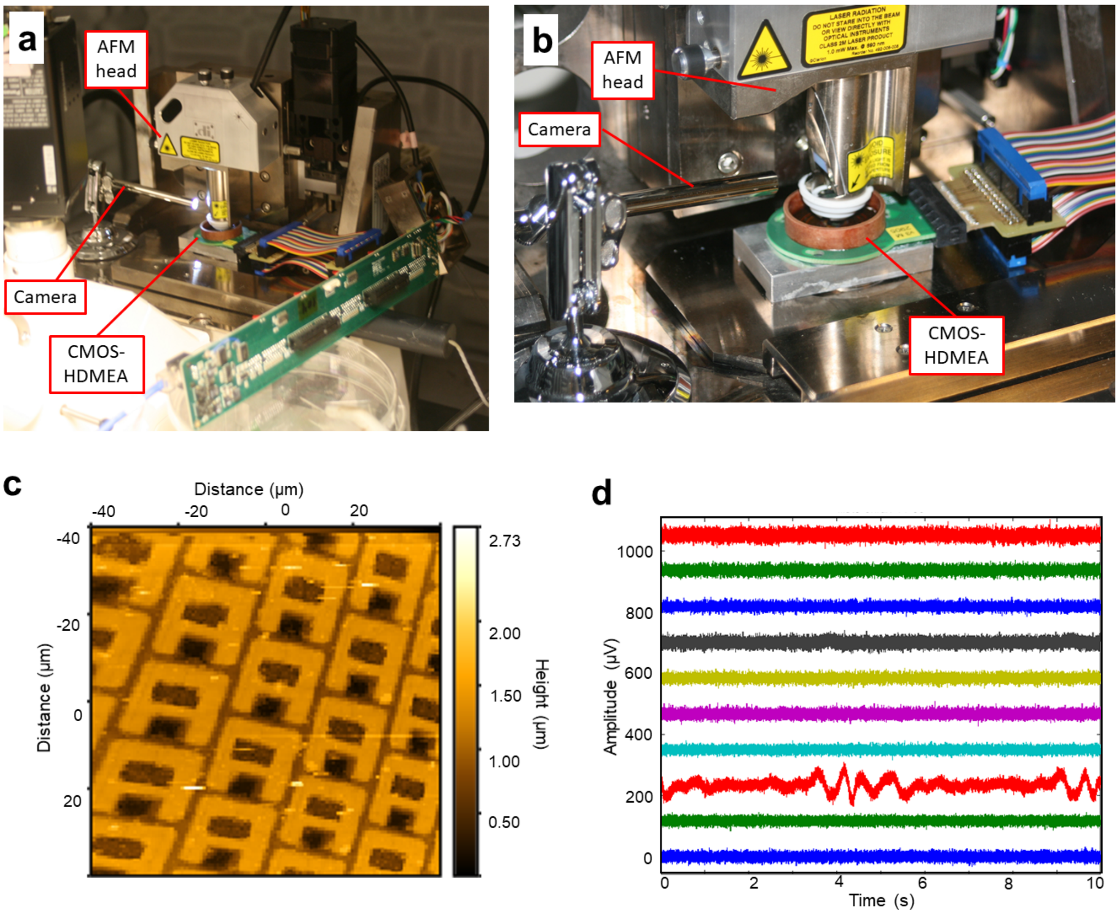

Figure 4–22: **AFM and CMOS-HDMEA functionality. a.** Final configuration of the AFM and CMOS-HDMEA. **b.** Close up of the AFM head and the CMOS chip. Simultaneous measurements were made with this set up. **c.** AFM topography scan of the MEA surface. Non-linearities in the scan result from the piezoelectric hysteresis. **d.** Signal recordings from the microelectrodes. Most of the signals appear quiescent since there was no current or voltage change during the AFM scan. On several ocassions, there will be traces of unexplained noise (red signal at 200 $\mu V$), possibly due to cross-talk with the AFM system.

there is a lot of room for improvement. We have, however, demonstrated that in principle a combined AFM and CMOS-HDMEA system is possible.

## 4.4 Conclusion

This chapter shows that a change in membrane potential is not the only process that is happening in an electrogenic cell during action potential signalling. Studies have shown similar mechanical and thermal responses across different types of neurons. Our understanding of these phenomena is gradually deepening, as methodologies to measure changes in the cell are improving in line with technological advancements. Our lab has taken on the challenge to develop a combined AFM and CMOS-HDMEA, in hopes of offering a new platform to perform more complex experiments to uncover more information about electrogenic cells. Initial testings show that the AFM and CMOS-HDMEA set up that we have function, however, the results are very preliminary and there is definitely plenty of room for improvement.

# CHAPTER 5

# NEURONAL STIMULATION AND RECORDING

In this chapter, steps taken to incorporate live biological cells on the combined AFM and CMOS-HDMEA set up will be detailed. Instead of diving straight into placing cells on the HDMEA, it was imperative to master the cell dissection and cultures before attempting to experiment on them.

## 5.1 Sharp electrode recording on Aplysia neurons

The first cell type of choice were neurons from the Aplysia californica sea slug as the neurons are significantly larger than rat neurons. Figure 5–1 shows an image of the Aplysia californica sea slug and a neuron that was isolated from the pleural-pedal ganglia. From the image, the cell body itself measures $\approx 100\ \mu m$ in diameter and the axon $\approx 10\ \mu m$ in diameter. Recalling the lack of optical access in the combined AFM and CMOS-HDMEA set up, utilising a larger specimen would be highly advantageous as a first experiment. As the project further develops, the end goal would be to incorporate rat neurons, which are morphological and genetically more similar to human neurons, for the study.

Aplysia neurons are commonly used in studies regarding learning and memory, and the most commonly used method to record signals from these neurons is

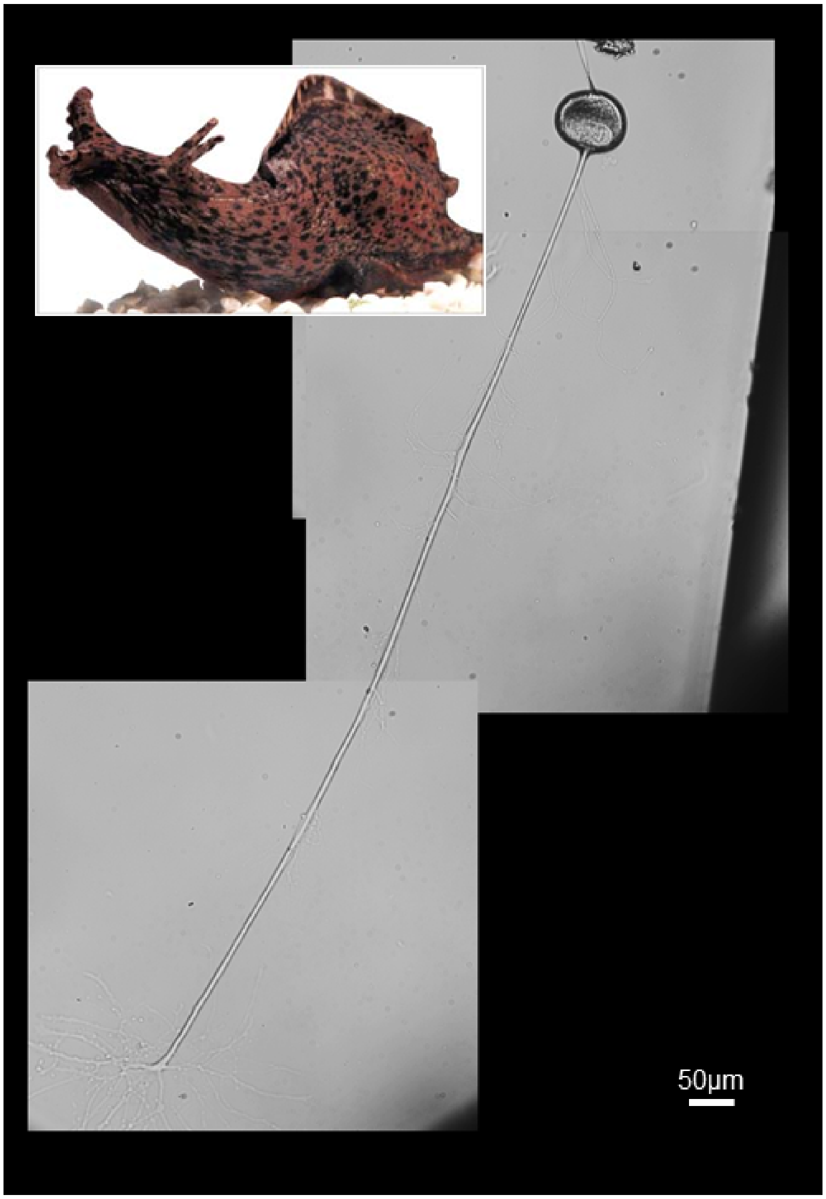

Figure 5–1: **Aplysia californica sea slug and a neuron.** Top left inset is an image of an Aplysia californica sea slug. Next to it is a bright-field image of a neuron extracted from the pleural-pedal ganglia of the sea slug. The Aplysia californica figure was obtained with permission from *Eric Kandel and Aplysia californica: their role in the elucidation of mechanisms of memory and the study of psychotherapy by M. Robertson and G. Walter, 2014, Copyright © 2010 John Wiley.*

the intracellular 'sharp' microelectrode recording technique (previously mentioned in Chapter 3.2.1.1). Before incorporating the neurons onto the HDMEA platform, we first had to record signals from the neurons using known methods. In doing so, we were also verifying the viability of the neuron cell cultures as well as understand the type of signals that one would expect from these cells.

### Cell culture

Aplysia californica sea slugs are obtained from the National Institutes of Health National Resource for Aplysia mariculture facility at the University of Miami (Miami, Florida, USA). Pleural-pedal ganglia are isolated from the animal and digested in L-15 media with added protease (Invitrogen, Life Technologies Inc., Ontario, Canada) for 20 hours at room temperature. $35mm$ glass-bottom dishes (MatTex, Ashland, MA) are coated with 1 $mg/mL$ poly-L-lysine solution (Sigma-Aldrich, St. Louis, MO) for at least 2 hours before plating the cells. After that, the poly-L-lysine solution is removed and replaced with L-15 media supplemented with salts (Invitrogen, Life Technologies Inc., Ontario, Canada) adjusted to match the haemolymph of the Aplysia. Individual neurons are isolated from the ganglia and carefully transferred to the glass-bottom dish. The neurons are left aside at room temperature for approximately 18 hours, to ensure proper adhesion of the neuron on the dish. More details about the cell culture process can be found at [Dunn et al., 2012, Dunn and Sossin, 2013].

### Sharp microelectrode recording

Prior to recording from the neuron, sharp pipettes are made using a Sutter P89 (Sutter Instruments, Novato, CA) pipette puller and back-filled with 2 $M$ potassium sulphate solution. The sharp pipette is attached to an Axopatch 200A patch clamp amplifier (Axon Instruments, Molecular Devices, San Jose, CA) and moved towards the cell body of the neuron using a micromanipulator. The sharp pipette was checked for air bubbles or breakage at the tip before attempting to impale the neuron. Once the neuron has been successfully impaled, a negative current is applied to hold the membrane potential at approximately -60 $mV$. A positive current is later applied to

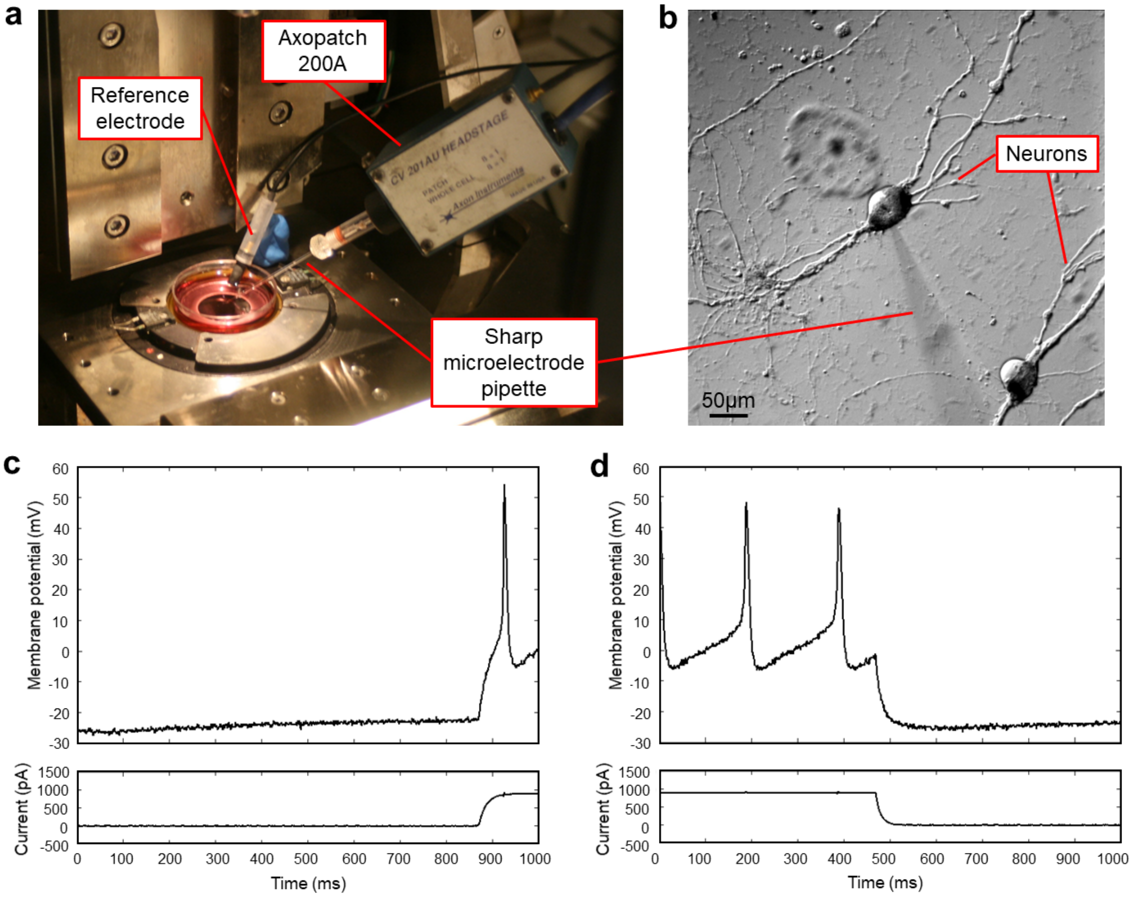

Figure 5–2: **Intracellular 'sharp' microelectrode recording on Aplysia neurons. a.** Sharp microelectrode recording set up on the AFM stage. **b.** Bright field image of the Aplysia neurons on the glass dish. A sharp microelectrode pipette has impaled one of the neurons. **(c,d)** Sequential frames showing the action potentials recorded from an Aplysia neuron. In this case, the neuron was firing spontaneously and had a resting membrane potential of ≈ -25 $mV$.

depolarise and record the action potentials of the neuron. Note that since a patch clamp amplifier was used, no bridge balancing could be done, therefore, the absolute values recorded by the microelectrode are not accurate. More details about the intracellular sharp microelectrode recording procedure can be found at [Dunn et al., 2012, Dunn and Sossin, 2013].

The sharp microelectrode recording set up mounted on the AFM stage is shown in Figure 5–2 (a), while an image of the neuron after being impaled by the sharp microelectrode pipette is shown in Figure 5–2 (b). After several attempts at dissecting the Aplysia ganglia, we were finally able to consistently isolate and culture healthy cells. On occasions, we would get a neuron that was spontaneously active. Figure 5–2 (c,d) show the recordings from a neuron that fired spontaneously. The resting membrane potential for that neuron was ≈ -25 $mV$. When given a positive current injection, the neuron fired action potentials.

The results of this section prove that the Aplysia neurons that were cultured are healthy and viable.

## 5.2 External stimulation of Aplysia neurons

The next step of the process was to identify if the Aplysia neurons were excitable externally, and if so, the range of voltages that the neurons respond to. To do so, we incorporated a concentric bipolar microelectrode (CBARC) (FHC Inc, Maine, USA) to the current intracellular ‘sharp’ microelectrode set up, to induce external voltage stimulation to the neurons. The set up on the AFM stage is shown in Figure 5–3 (a,b). The CBARC microelectrode is attached to and moved using a second micromanipulator.

After many attempts, the most effective way to probe the neuron is by first aligning the CBARC microelectrode and sharp microelectrode pipette close to the cell body before impaling the neuron. Minimising major movements reduces the chances of physically damaging the neuron. Once the viability and activity of the neuron has been verified with the sharp microelectrode, the membrane potential of the cell is reduced to its holding potential at ≈ -70 $mV$. Utilising the second micromanipulator, the CBARC is carefully moved closer towards the cell body, taking care not to generate any movements that will cause a tear in the cell membrane

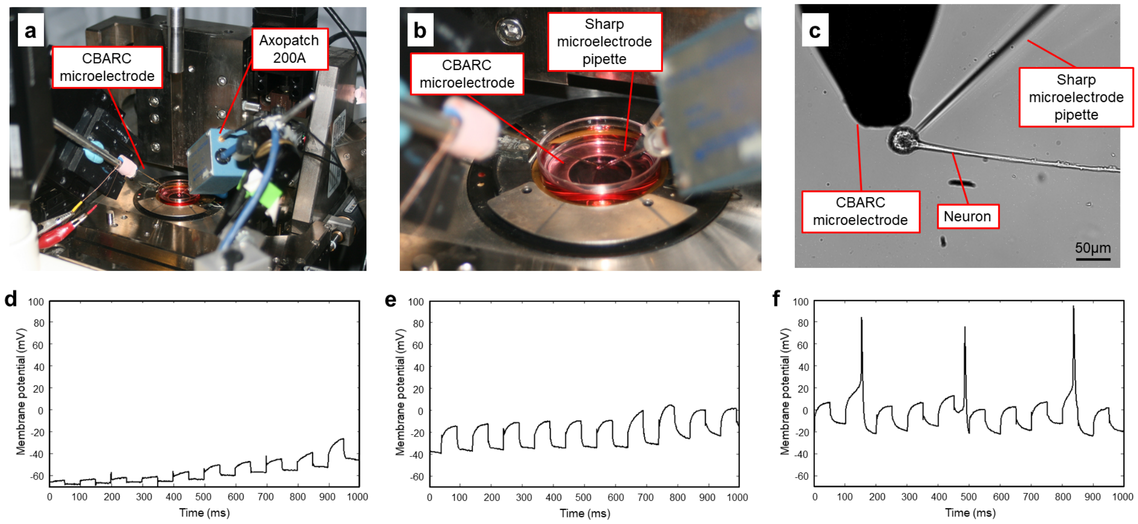

Figure 5–3: **External stimulation of the Aplysia neuron. a.** Set up showing the CBARC stimulation electrode and sharp microelectrode connected to the Axopatch patch clamp amplifier. **b.** Close up of both electrodes probing a neuron in the glass-bottom dish. **c.** Image of an Aplysia neuron after being impaled by the sharp microelectrode pipette, and being stimulated by the CBARC electrode next to the cell body. **(d,e,f)** Sequential frames showing the change in membrane potential as the neuron is being stimulated externally by the CBARC electrode. **(f)** Action potentials were successfully generated once the membrane potential reached the threshold for firing action potentials.

by the sharp microelectrode pipette. A close up image of the positioning of both the microelectrodes on an Aplysia neuron is shown in Figure 5–3 (c). Once the CBARC microelectrode is close to the cell body, an increasing voltage stimulation is directed at the neuron. Sequential images showing the rise in membrane potential as the voltage is being ramped up is shown in Figure 5–3 (d-f). At a membrane potential of $\approx 20\ mV$, action potentials were generated. On average, the Aplysia neurons responded to a $20\ mV_{pp}$ external stimulus when the CBARC electrode is situated $\approx 15\ \mu m$ from the cell body of the neuron. Take note that these values are not absolute as bridge-balancing was not performed for the sharp microelectrode recordings. In addition to that, the response of the neuron to the external stimulation differs from cell to cell and is largely affected by the quality of the poke by the sharp microelectrode pipette. As we know, impaling the neuron subjects the cell to physical damage, and a less than ideal poke could lead to higher levels of ionic leakage from the external environment. Moreover, the actual membrane potential of the undamaged neuron is most likely different from the one after impalement by the sharp microelectrode pipette due to influence from ion leakages across the membrane.

The results of this section show that the Aplysia neurons do respond to external stimulation, and should react to stimulation from the CMOS-HDMEA.

## 5.3 CMOS-HDMEA recordings

Now that we were able to confirm the viability of the cell cultures and the minimum requirements to stimulate and record signals from the cells, it was time to test the neurons out on the CMOS-HDMEA.

Firstly, we have to address the challenge of positioning the isolated Aplysia neurons on top of active MEA. Unlike dissociated rat cultures, Aplysia neurons are hand-picked from the ganglia and transferred to the MEA. As we recall, the active MEA area measures only $2.00 \times 1.75\ mm^2$. As such, there exists a challenge to strategically place the neurons on the small area. When the neurons are pipetted into the MEA dish, there was a tendency for the cells to drift away from the active MEA area, as shown in Figure 5–4 (a). Not being on the microelectrodes meant that signals could not be recorded from the neurons. Initially, we tried to ‘confine’ the neuron in the active MEA region by pipetting a small droplet of cell culture media, just enough to cover the active MEA region. However, this method was susceptible to

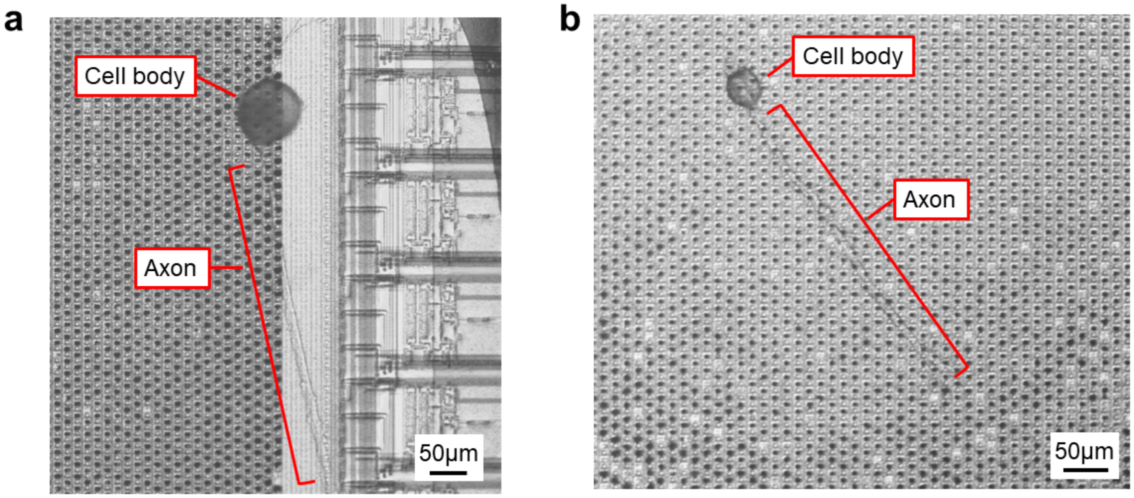

Figure 5–4: **Aplysia neurons on the CMOS-HDMEA surface. a.** Image of a neuron that drifted away from the active MEA region. Only part of the cell body and axon are lying on some of the microelectrodes. **b.** Image of a neuron that is on the active MEA region. One can barely see the translucent axon.

severe evaporation that lead to the neurons drying out and dying. The other method that seemed to work was to keep the volume of the cell media the same ($\approx 2\ ml$) in the MEA dish, but to pipette the isolated neurons as slowly and as closely as one could to the surface of the MEA. To increase the success of having at least a neuron in that region, at least 6 isolated neurons were placed in each dish. On fortunate occassions, we would have a neuron resting in the centre of the active MEA area for experimenting (Figure 5–4 (b)). From the microscopic images, it is easy to see the cell body on the MEA. However, the axons are relatively small and transparent. Therefore, adding to the optical limitations that one has with this combined AFM and CMOS-HDMEA set up. Nevertheless, this section shows that we were able to culture Aplysia neurons on the MEA itself.

### 5.3.1 Recording from Aplysia neurons

At first, we attempted to record the spontaneous activity of the Aplysia neurons to identify the location of the neurons on the CMOS-HDMEA. However, after multiple attempts, there were no recorded neural activity and we concluded that these neurons do no fire spontaneously. Besides that, perfusion of KCl into the dish did not incite any activity from the neurons. Not being able to identify the location of the Aplysia neurons electrically brought us to our next idea.

#### Optical stimulation of the Aplysia neurons

We explored the possibility of identifying the exact location of the neuron on the MEA by overlaying the map of the electrodes on top of a microscope image of the MEA surface. To do so, several images were taken under an upright microscope and stitched together to form an image as shown in Figure 5–5 (a). From the image, only two cell bodies of the Aplysia neurons were clearly visible, but knowing that was enough for us to obtain a rough idea of where the neurons were located. To obtain the exact coordinate where the neurons were located on the MEA, an electrode map was plotted on top of the microscopic images (Figure 5–5 (b)). Once the images were properly aligned, the microelectrodes beneath the cell body of interest were selected. Figure 5–5 (c) shows 3 microelectrodes that were selected beneath the cell body of the bigger neuron. Voltage pulses (ranging from 100 - 200 $mV$) were sent to the microelectrodes, and the responses of the neurons were recorded directly after. An activity map of the signals recorded is shown in Figure 5–5 (d), and the location where the electrodes were stimulated is shown as the bright spot in the map. However, no activity from the neurons were detected. After numerous attempts, we failed at recording electrical activity from the Aplysia neurons, no matter the methodology used. There are a few assumptions as to why the Aplysia neurons were not responding. Perhaps, the neurons were not located close enough to the microelectrodes, therefore changes in membrane potentials were not detected. Perhaps the Aplysia neurons are not as viable as the ones cultured on a flat glass-bottom dish, or that these neurons simply do not respond well to external stimulation and recording procedures like that.

### 5.3.2 Recording from cardiomyocytes

Having run out of options with the Aplysia neurons, we decided to take a turn and try a different cell type. As a proof of concept, we would just like to to show that simultaneous mechanical and electrical signals were possible using the integrated

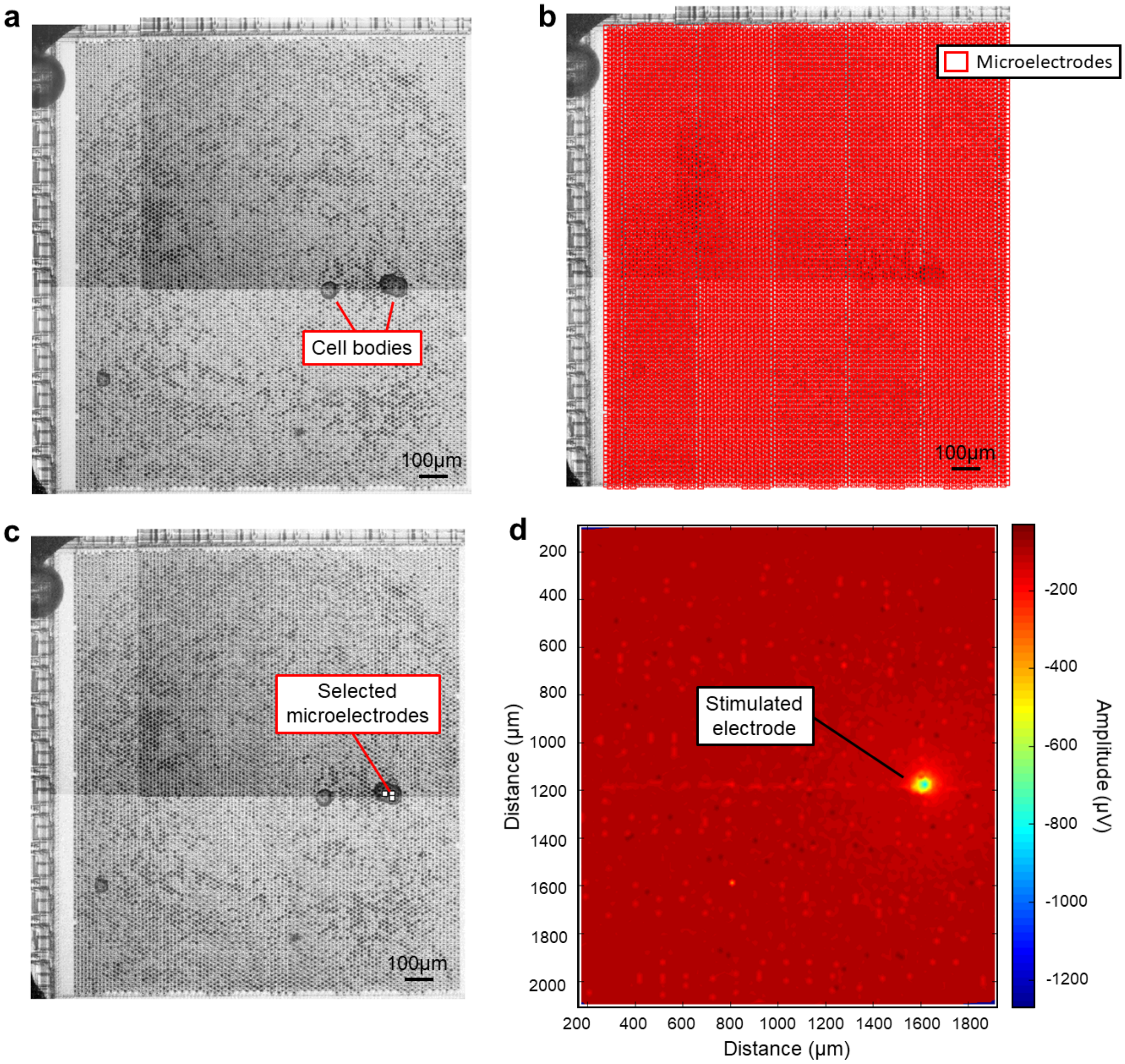

Figure 5–5: **Optical stimulation of neurons on the CMOS-HDMEA. a.** Image of the Aplysia neurons on the microelectrodes. Only the cell bodies are visible from this image. **b.** An overlay of the microelectrodes on the image. Each red rectangle represents a single microelectrode. **c.** Selection of the microelectrodes that are directly below the cell bodies of interest. **d.** Voltage stimulation pulse are sent to the selected microelectrodes, in hopes of stimulating the Aplysia neurons.

AFM and CMOS-HDMEA set up. For that reason, cardiomyocytes were the perfect candidate, as these cells are spontaneously active mechanically and electrically.

### Cell cultures

Human cardiomyocytes obtained from induced pluripotent stem (iPS) cells (FUJIFILM Cellular Dynamics International, Wisconsin, USA) were used. The cell cultures were performed according to the iCell Cadiomyocytes$^2$ user's guide from Cellular Dynamics International. Thawed cardiomyocytes were plated on a MEA chip that was precoated with poly-L-lysine (Sigma-Aldrich, St. Louis, MO) at least 1 hour before cell plating. Four hours after plating the cells, the medium was aspirated and replaced with culture media consisting of Dulbecco's Modified Eagle Medium supplemented with 10% fetal bovine serum and 1% penicillin-streptomycin (Invitrogen, Life Technologies Inc., Ontario, Canada). The cardiomyocytes were stored in a cell culture incubator at $37°C$ with 5% $CO_2$ for four days before experimenting. Recordings of the cardiomyocytes were performed according to procedures described in Section 3.2.3.2.

### Reviewing the CMOS-HDMEA signals

Spontaneous activity from cardiomyocytes were recorded by the CMOS-HDMEA in an incubator at $37°C$ with 5% $CO_2$ a week after the cells were plated. Figure 5–6 shows signals from 10 randomly selected electrodes. Spiking activity is seen and in some occasions, the spikes are synchronised across the electrodes. To further analyse the signals that we obtained, the spikes were detected using the amplitude thresholding method described in Section 3.2.3.3. The detected spikes are plotted in grey in Figure 5–7 (a). The waveform of the spikes were strangely triangular and do not resemble action potentials that originate from cardiomyocytes. Additionally, the spikes were sorted according to the amplitude and width at FWHM of the spikes. A scatter plot of the results (Figure 5–7 (b)) indicate that there is only one cluster of spikes that have very short amplitudes. When compared to the results obtained in Section 3.2.3.3 with the rat cortical neurons (Figure 3–9 (b)), it is evident that the spikes detected do not originate from the cultured cardiomyocytes.

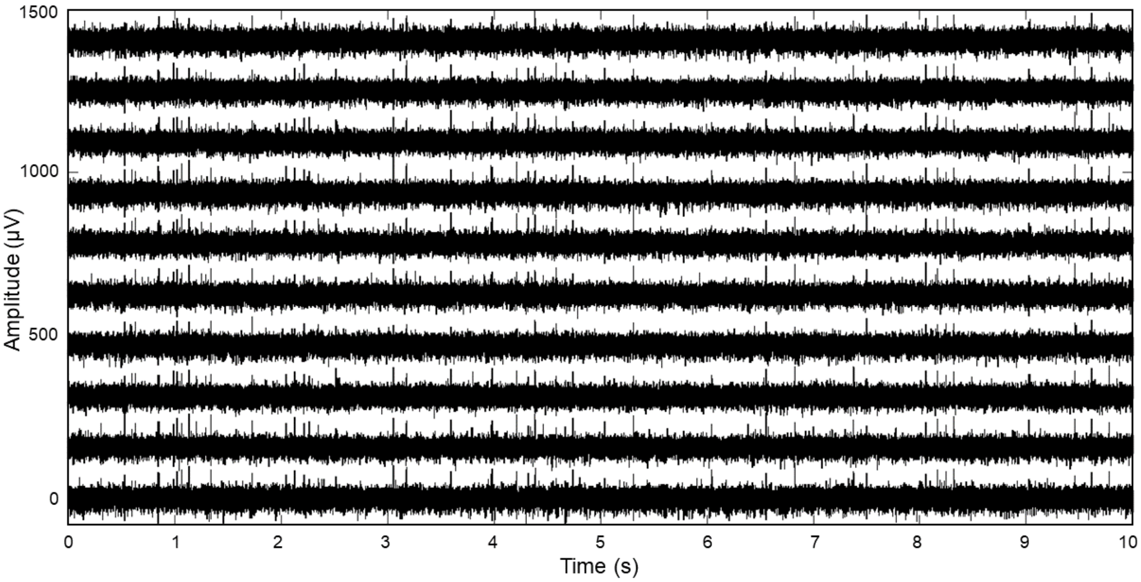

Figure 5–6: **Individual cardiomyocytes signals.** Figure shows electrical signals from 10 randomly selected electrodes from the same recording block. The signals are plotted at a constant offset from one another.

In conclusion, the signals recorded were not from the cardiomyocytes and it is not known where these spikes were originating from. Further attempts at the measurements were stopped due to lab closure as a result of the on-going pandemic.

## 5.4 Conclusion

This section sums up our attempts at incorporating biological samples onto the combined AFM and CMOS-HDMEA set up. Unfortunately, we failed at recording electrical signals from neurons and cardiomyocytes using the CMOS-HDMEA set up, and further attempts at this project had to end prematurely due to uncalled for circumstances.

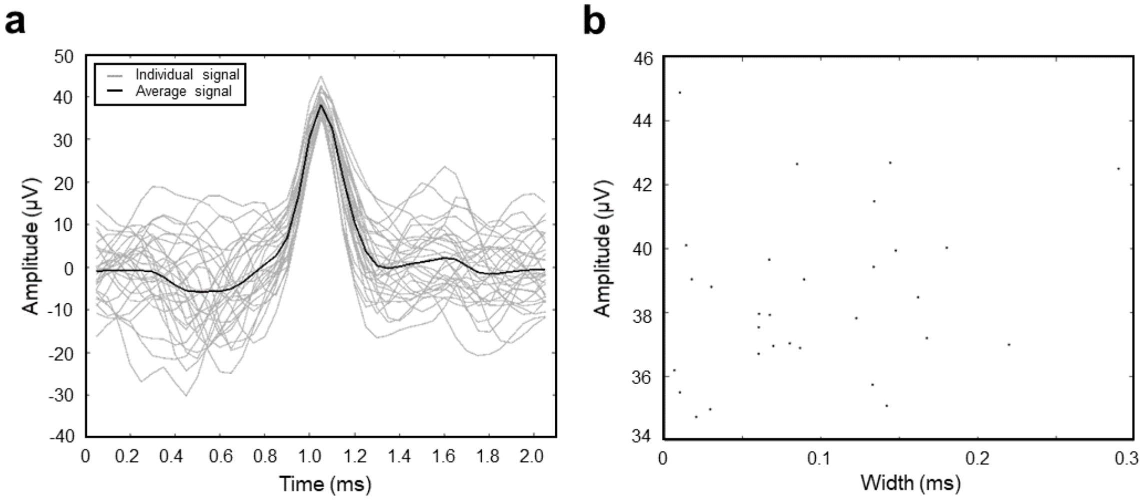

Figure 5–7: **Amplitude threshold spike detection and spike sorting. a.** Spikes were detected using the amplitude threshold method based on Equation 3.5. Individual spikes are plotted in grey, while the black line represents the average of all the spikes that were detected. The waveform of the spikes do not seem to resemble an action potential, which is an implication that the spikes may not be cellular in origin. **b.** Categorising the detected spikes by amplitude and width (FWHM). There seems to be only one cluster of spikes, with a rather small amplitude.

# CHAPTER 6

# CONCLUSION AND OUTLOOK

This thesis has been a journey attempting to develop an integrated experimental platform allowing simultaneous force and electrophysiological measurements on biological cells, through the integration of an AFM and a CMOS-MEA device. First, we showed the causes and the impact that neurological dysfunction have on the physical ability of a person. And, we highlight the importance of research to gain a better understanding of the physical properties and mechanical processes in cells, and how mechanical damage can lead to physical impairment in cells.

Chapter 2 focused on the importance of the evolving field of mechanobiology and how imperative it is for different fields of science to collaborate and develop tools and techniques which enable us to obtain more thorough and accurate measurements of biological properties. In particular, we explored popular AFM techniques to obtain elastic modulus values of cells and showed that there were stark discrepancies in the reported values, depending on the contact mechanics model that was being utilised albeit probing the same cell. Therefore, accurately modelling the topography of the cell at the point of contact is crucial to obtaining an accurate estimation of the intrinsic property of the cell. The knowledge of the elastic modulus of a cell is crucial to understanding the underlying properties and mechanisms that maintain a cell's shape, and assist in cellular processes such as cell proliferation, migration, and differentiation. To improve upon the elastic modulus measurements, one should first attempt to culture cells in a way that mimics their native growth environment closely. For instance, culturing neurons on a neuro microfluidic device (Ananda Devices, Laval, QC) to ensure the growth of axons of neurons are organised in a similar fashion to that in the brain or spinal cord. From there, a combination of AFM topology images and finite element modelling should be utilised to accurately model the morphology of the cell being probed and to accurately determine the height of the cell. Having an accurate visualisation of the cell composition is extremely valuable in determining the exact amount of force or depth that one can probe with before being influenced by other components within the cell. Or, knowing the exact compositional layer of the cell, one could utilise this information to probe the mechanical properties or to measure the direct effects that certain drugs have on these cytoskeletal components within the cell.

Chapter 3 explored the fundamentals of cellular signalling in electrogenic cells. Understanding how action potentials are generated was the first step to deciphering cellular communication. In neurons, for instance, the language of communication in a neural network, the messages that are transmitted through the frequency of firing, number of spikes, or bursts of action potentials, are still relatively poorly understood. The tools and methodology to measure electrical signals from electrogenic cells, are constantly evolving and improving, in hopes of bettering our ability to capture and understand these messages that cells are conveying. We showed a sample recording of spontaneous neural activity on a CMOS-HDMEA in this thesis. While the attempt shown here is simple, there is a plethora of experiments that one could do with this device. As an example, one could imagine culturing several non-connected neural populations on the same CMOS-HDMEA chip using co-culture microfluidic devices (similar to those from Ananda Devices, Laval, QC), and manually reconnecting these neural populations according to techniques developed by [Magdesian et al., 2016] and [Magdesian et al., 2017]. With the spatio and temporal recording capabilities of the CMOS-HDMEA, one could monitor the progression of the extended neurite and the connection that is being made between the separate neuronal populations by observing the electrical signals. Perhaps, with these signals, one would have an insight as to how a functional neurite is made and an understanding of how initial neural networks are formed.

Chapter 4 brings light to the fact that there exist a relationship between electrical signalling and physical changes in biological cells. While the mechanisms by which electrical and physical properties influence each other is not adequately understood, this chapter focuses on the methodologies that have been or are in development, in attempts to capture this neuronal behaviour. The development of an integrated AFM and CMOS-HDMEA set up came to be the central focus of this thesis project, and was shown to work with very preliminary results. Needless to say, this integrated set up has much to be improved upon. For instance, the Bioscope II AFM only has one operation mode (i.e. contact mode) when in liquid. This implies that contact mode is used to perform a topography scan to identify the exact location of the neuron. Contact mode imaging is less than ideal as the tip is generally outlines the surface of the sample, and in the case of a soft biological cell, it is easy to cause damage or rupture the surface of the cell with the cantilever tip. To add to that, there is no known way to check the viability and integrity of the cell without optical access to the CMOS-HDMEA surface. Utilising a more up-to-date AFM with additional operational modes in liquid (e.g. force-volume mode, intermittent contact mode, tapping mode) would be beneficial to increase the number and varieties of experiments that could be performed on biological samples, while minimising the damage that would be incurred on the cells. Additionally, most modern AFMs come equipped with a built in camera that enables one to view the surface of the sample from the top. Having full optical access of the surface, provides the user with the freedom to identify cells on the MEA surface, to accurately position the AFM tip onto the cell surface, and perform precise manipulations of the cell without the fear of physically harming the live cell. Besides that, with the camera, one can also monitor the health of the cell throughout the entire duration of the experiment, a feature that would be have been impossible in the current combined AFM and CMOS-HDMEA set up. If the AFM comes with fluorescence imaging capabilities, one could perhaps study the effects of $Ca^{2+}$ ions on the electrical signalling and mechanical changes within the cell. One could also attempt to integrate a different type of MEA. For example, the successor of CMOS-HDMEAs used in this thesis boasts a total of 26,400 microelectrodes packed in a larger sensing area, measuring 3.85 x 2.10 $mm^2$, with 1024 low-noise readout channels [Müller et al., 2015]. Firstly, having a larger sensing area increases the scanning area of the AFM and reduces the chances of geometrical incompatibilities. Secondly, a higher density of microelectrodes means an improvement to the spatiotemporal resolution of the recordings, implying that one could potentially image the entire neuron to a degree of accurately identifying the components of the neuron without the need of relying on optical microscopy.

Finally, Chapter 5 detailed our failed attempts at incorporating biological samples to the combined AFM and CMOS-HDMEA set up. While it is a little premature to point out specific improvements that could be made since not many attempts were made at this stage (pre-pandemic), we can anticipate some challenges that one might face. Positioning neurons seemed to be a challenge, and one could potentially avoid that problem by creating a temporary well (perhaps out of bio-compatible PDMS), to contain the neurons within the active MEA sensing area. Additionally, the surface of the MEA is not perfectly flat, and should a cell decide to grow in the trenches between the electrodes, one would not be able to pick up electrical signals from the cell. To overcome that, perhaps a microfluidic device, similar to the neuro microfluidic device by Ananda Devices, Laval, QC, could be used to force the neurons or cells to grow within the space along the microelectrodes.

With an improved combined AFM and CMOS-HDMEA set up, one could attempt the list of experimental ideas from Section 4.3.1 and more, including the attempt to perform simultaneous force and electrical measurements on isolated single rat neurons.

# REFERENCES

[Abbott et al., 1958] Abbott, B. C., Hill, A. V., and Howarth, J. V. (1958). The positive and negative heat production associated with a nerve impulse. *Proceedings of the Royal Society of London. Series B, Biological sciences.*

[Aguayo et al., 1990] Aguayo, A. J., Bray, G. M., Rasminsky, M., Zwimpfer, T., Carter, D., and Vidal-Sanz, M. (1990). Synaptic connections made by axons regenerating in the central nervous system of adult mammals. *Journal of Experimental Biology*, 153:199–224.

[Ahmed et al., 2015] Ahmed, W. W., Fodor, É., and Betz, T. (2015). Active cell mechanics: Measurement and theory. *Biochimica et Biophysica Acta - Molecular Cell Research*, 1853(11):3083–3094.

[Amblard et al., 1996] Amblard, F., Yurke, B., Pargellis, A., and Leibler, S. (1996). A magnetic manipulator for studying local rheology and micromechanical properties of biological systems. *Review of Scientific Instruments.*

[Andolfi et al., 2014] Andolfi, L., Bourkoula, E., Migliorini, E., Palma, A., Pucer, A., Skrap, M., Scoles, G., Beltrami, A. P., Cesselli, D., and Lazzarino, M. (2014). Investigation of adhesion and mechanical properties of human glioma cells by single cell force spectroscopy and atomic force microscopy. *PLoS ONE.*

[Ashkin, 1970] Ashkin, A. (1970). Acceleration and Trapping of Particles by Radiation Pressure. *Physical Review Letters*, 24(4):156–159.

[Bakkum et al., 2013] Bakkum, D. J., Frey, U., Radivojevic, M., Russell, T. L., Müller, J., Fiscella, M., Takahashi, H., and Hierlemann, A. (2013). Tracking axonal action potential propagation on a high-density microelectrode array across hundreds of sites. *Nature Communications*, 4.

[Bannister and Langton, 2012] Bannister, N. and Langton, P. (2012). Patch Clamp Recording. In *Essential Guide to Reading Biomedical Papers*.

[Beirowski et al., 2010] Beirowski, B., Nógrádi, A., Babetto, E., Garcia-Alias, G., and Coleman, M. P. (2010). Mechanisms of axonal spheroid formation in central nervous system wallerian degeneration. *Journal of Neuropathology and Experimental Neurology*, 69(5):455–472.

[Bernick et al., 2011] Bernick, K. B., Prevost, T. P., Suresh, S., and Socrate, S. (2011). Biomechanics of single cortical neurons. *Acta Biomaterialia*, 7(3):1210–1219.

[Bernstein and Bernstein, 1971] Bernstein, J. J. and Bernstein, M. E. (1971). Axonal regeneration and formation of synapses proximal to the site of lesion following hemisection of the rat spinal cord. *Experimental Neurology*, 30(2):336–351.

[Beussman et al., 2016] Beussman, K. M., Rodriguez, M. L., Leonard, A., Taparia, N., Thompson, C. R., and Sniadecki, N. J. (2016). Micropost arrays for measuring stem cell-derived cardiomyocyte contractility. *Methods*.

[Bilodeau, 1992] Bilodeau, G. G. (1992). Regular pyramid punch problem. *Journal of Applied Mechanics, Transactions ASME*, 59(3):519–523.

[Binnig et al., 1986] Binnig, G., Quate, C. F., and Gerber, C. (1986). Atomic force microscope. *Physical Review Letters*.

[Bradke et al., 2012] Bradke, F., Fawcett, J. W., and Spira, M. E. (2012). Assembly of a new growth cone after axotomy: The precursor to axon regeneration. *Nature Reviews Neuroscience*, 13(3):183–193.

[Bronkhorst et al., 1995] Bronkhorst, P. J., Streekstra, G. J., Grimbergen, J., Nijhof, E. J., Sixma, J. J., and Brakenhoff, G. J. (1995). A new method to study shape recovery of red blood cells using multiple optical trapping. *Biophysical Journal*.

[Cappella and Dietler, 1999] Cappella, B. and Dietler, G. (1999). Force-distance curves by atomic force microscopy. *Surface Science Reports*, 34(1-3):1–3.

[Carter and Shieh, 2015] Carter, M. and Shieh, J. (2015). Chapter 4 – Electrophysiology. *Guide to Research Techniques in Neuroscience*, pages 89–115.

[Charras and Horton, 2002] Charras, G. T. and Horton, M. A. (2002). Single cell mechanotransduction and its modulation analyzed by atomic force microscope indentation. *Biophysical Journal*.

[Charras et al., 2001] Charras, G. T., Lehenkari, P. P., and Horton, M. A. (2001). Atomic force microscopy can be used to mechanically stimulate osteoblasts and evaluate cellular strain distributions. *Ultramicroscopy*, 86(1-2):85–95.

[Chen et al., 2011] Chen, J., Zheng, Y., Tan, Q., Zhang, Y. L., Li, J., Geddie, W. R., Jewett, M. A., and Sun, Y. (2011). A microfluidic device for simultaneous electrical and mechanical measurements on single cells. *Biomicrofluidics*, 5(1):1–11.

[Chew et al., 2012] Chew, D. J., Fawcett, J. W., and Andrews, M. R. (2012). *The challenges of long-distance axon regeneration in the injured CNS*, volume 201. Elsevier B.V., 1 edition.

[Chicurel et al., 1998] Chicurel, M. E., Chen, C. S., and Ingber, D. E. (1998). Cellular control lies in the balance of forces. *Current Opinion in Cell Biology*.

[Chighizola et al., 2019] Chighizola, M., Dini, T., Lenardi, C., Milani, P., Podestà, A., and Schulte, C. (2019). Mechanotransduction in neuronal cell development and functioning. *Biophysical Reviews*, 11(5):701–720.

[Cockins et al., 2007] Cockins, L., Miyahara, Y., Stomp, R., and Grutter, P. (2007). High-aspect ratio metal tips attached to atomic force microscopy cantilevers with controlled angle, length, and radius for electrostatic force microscopy. *Review of Scientific Instruments*, 78(11):113704–113707.

[Cogollo et al., 2011] Cogollo, J. F., Tedesco, M., Martinoia, S., and Raiteri, R. (2011). A new integrated system combining atomic force microscopy and microelectrode array for measuring the mechanical properties of living cardiac myocytes. *Biomedical Microdevices*, 13(4):613–621.

[Coleman, 2005] Coleman, M. (2005). Axon degeneration mechanisms: Commonality amid diversity. *Nature Reviews Neuroscience*, 6(11):889–898.

[Crick, 1982] Crick, F. (1982). Do dendritic spines twitch? *Trends in Neurosciences*, 5(C):44–46.

[Cross et al., 2007] Cross, S. E., Kreth, J., Zhu, L., Sullivan, R., Shi, W., Qi, F., and Gimzewski, J. K. (2007). Nanomechanical properties of glucans and associated cell-surface adhesion of Streptococcus mutans probed by atomic force microscopy under in situ conditions. *Microbiology*, 153(9):3124–3132.

[Danilowicz et al., 2005] Danilowicz, C., Greenfield, D., and Prentiss, M. (2005). Dissociation of ligand-receptor complexes using magnet tweezers. *Analytical Chemistry*.

[David and Aguayo, 1981] David, S. and Aguayo, A. (1981). Axonal elongation into peripheral nervous system "bridges" after central nervous system injury in adult rats. *Science*, 214(4523):931–933.

[Debanne et al., 2011] Debanne, D., Campanac, E., Bialowas, A., Carlier, E., and Alcaraz, G. (2011). Axon physiology. *Physiological Reviews*, 91(2):555–602.

[Derjaguin et al., 1975] Derjaguin, B. V., Muller, V. M., and Toporov, Y. P. (1975). Effect of contact deformation on the adhesion of elastic solids. *Journal of Colloid and Interface Science*, 53(2):314–326.

[Dimitriadis et al., 2002] Dimitriadis, E. K., Horkay, F., Maresca, J., Kachar, B., and Chadwick, R. S. (2002). Determination of elastic moduli of thin layers of soft material using the atomic force microscope. *Biophysical Journal*, 82(5):2798–2810.

[Domke et al., 1999] Domke, J., Parak, W. J., George, M., Gaub, H. E., and Radmacher, M. (1999). Mapping the mechanical pulse of single cardiomyocytes with the atomic force microscope. *European Biophysics Journal*, 28(3):179–186.

[Douglas Fields, 2012] Douglas Fields, R. (2012). Signaling by Neuronal Swelling. *Science Signaling*, 4(155):1–7.

[Dufrêne et al., 2017] Dufrêne, Y. F., Ando, T., Garcia, R., Alsteens, D., Martinez-Martin, D., Engel, A., Gerber, C., and Müller, D. J. (2017). Imaging modes of atomic force microscopy for application in molecular and cell biology. *Nature Nanotechnology*, 12(4):295–307.

[Duman et al., 2012] Duman, M., Neundlinger, I., Zhu, R., Preiner, J., Lamprecht, C., Chtcheglova, L. A., Rankl, C., Puntheeranurak, T., Ebner, A., and Hinterdorfer, P. (2012). *Atomic force microscopy*, volume 2.

[Dunn et al., 2012] Dunn, T. W., Farah, C. A., and Sossin, W. S. (2012). Inhibitory responses in Aplysia pleural sensory neurons act to block excitability, transmitter release, and PKC Apl II activation. *Journal of Neurophysiology*, 107(1):292–305.

[Dunn and Sossin, 2013] Dunn, T. W. and Sossin, W. S. (2013). Inhibition of the aplysia sensory neuron calcium current with dopamine and serotonin. *Journal of Neurophysiology*, 110(9):2071–2081.

[El Hady and Machta, 2015] El Hady, A. and Machta, B. B. (2015). Mechanical surface waves accompany action potential propagation. *Nature Communications*, 6:1–7.

[Eyckmans et al., 2011] Eyckmans, J., Boudou, T., Yu, X., and Chen, C. S. (2011). A Hitchhiker's Guide to Mechanobiology. *Developmental Cell*, 21(1):35–47.

[Federation et al., 1992] Federation, C. N. S., Coalition, C. B., Health, N., and Information, C. I. o. H. (1992). *The Burden of Neurological Diseases, Disorders and Injuries in Canada*, volume 47.

[Franks, 2005] Franks, W. A. (2005). *Towards monolithic CMOS cell-based biosensors*. PhD thesis.

[Frey, 2007] Frey, U. (2007). *High-Density Neural Interface and Microhotplate Gas Sensor in CMOS Technology*. PhD thesis, ETH Zurich, Switzerland.

[Frey et al., 2009a] Frey, U., Egert, U., Heer, F., Hafizovic, S., and Hierlemann, A. (2009a). Microelectronic system for high-resolution mapping of extracellular electric fields applied to brain slices. *Biosensors and Bioelectronics*, 24(7):2191–2198.

[Frey et al., 2009b] Frey, U., Egert, U., Jäckel, D., Sedivy, J., Ballini, M., Livi, P., Faraci, F., Heer, F., Hafizovic, S., Roscic, B., and Hierlemann, A. (2009b). Depth recording capabilities of planar high-density microelectrode arrays. *2009 4th International IEEE/EMBS Conference on Neural Engineering, NER '09*, 2:207–210.

[Frey et al., 2007] Frey, U., Sanchez-Bustamante, C. D., Ugniwenko, T., Heer, F., Sedivy, J., Hafizovic, S., Roscic, B., Fussenegger, M., Blau, A., Egert, U., and Hierlemann, A. (2007). Cell recordings with a CMOS high-density microelectrode array. *Annual International Conference of the IEEE Engineering in Medicine and Biology - Proceedings*, pages 167–170.

[Friedrichs et al., 2013] Friedrichs, J., Legate, K. R., Schubert, R., Bharadwaj, M., Werner, C., Müller, D. J., and Benoit, M. (2013). A practical guide to quantify cell adhesion using single-cell force spectroscopy. *Methods*, 60(2):169–178.

[Fromherz, 2003] Fromherz, P. (2003). Semiconductor chips with ion channels, nerve cells and brain. In *Physica E: Low-Dimensional Systems and Nanostructures*.

[Gandolfo et al., 2010] Gandolfo, M., Maccione, A., Tedesco, M., Martinoia, S., and Berdondini, L. (2010). Tracking burst patterns in hippocampal cultures with high-density CMOS-MEAs. *Journal of Neural Engineering*.

[Gavara, 2017] Gavara, N. (2017). A beginner's guide to atomic force microscopy probing for cell mechanics. *Microscopy Research and Technique*, 80(1):75–84.

[Goedecke et al., 2015] Goedecke, N., Bollhalder, M., Bernet, R., Silvan, U., and Snedeker, J. (2015). Easy and accurate mechano-profiling on micropost arrays. *Journal of Visualized Experiments*.

[Gonzalez-Perez et al., 2016] Gonzalez-Perez, A., Mosgaard, L. D., Budvytyte, R., Villagran-Vargas, E., Jackson, A. D., and Heimburg, T. (2016). Solitary electromechanical pulses in lobster neurons. *Biophysical Chemistry*, 216(15):51–59.

[Gosse and Croquette, 2002] Gosse, C. and Croquette, V. (2002). Magnetic tweezers: Micromanipulation and force measurement at the molecular level. *Biophysical Journal*.

[Grant, 2009] Grant, A. O. (2009). Cardiac ion channels. *Circulation: Arrhythmia and Electrophysiology*, 2(2):185–194.

[Hales et al., 2010] Hales, C. M., Rolston, J. D., and Potter, S. M. (2010). How to culture, record and stimulate neuronal networks on micro-electrode arrays (MEAs). *Journal of Visualized Experiments*.

[He and Jin, 2016] He, Z. and Jin, Y. (2016). Intrinsic Control of Axon Regeneration. *Neuron*, 90(3):437–451.

[Heer, 2005] Heer, F. (2005). *CMOS-based Microelectrode Array for Communication with Electrogenic Cells*. PhD thesis, Zurich.

[Heer et al., 2007] Heer, F., Hafizovic, S., Ugniwenko, T., Frey, U., Franks, W., Perriard, E., Perriard, J. C., Blau, A., Ziegler, C., and Hierlemann, A. (2007). Single-chip microelectronic system to interface with living cells. *Biosensors and Bioelectronics*.

[Hertz, 1882] Hertz, H. R. (1882). Uber die Beruhrung fester elastischer Korper und uber die Harte. *Verhandlung des Vereins zur Beforderung des GewerbefleiBes, Berlin*.

[Hierlemann et al., 2011] Hierlemann, A., Frey, U., Hafizovic, S., and Heer, F. (2011). Growing cells atop microelectronic chips: Interfacing electrogenic cells in vitro with CMOS-based microelectrode arrays. *Proceedings of the IEEE*.

[Hill et al., 1977] Hill, B., Schubert, E., Nokes, M., and Michelson, R. (1977). Laser interferometer measurement of changes in crayfish axon diameter concurrent with action potential. *Science*.

[Hill, 1950] Hill, D. K. (1950). The volume change resulting from stimulation of a giant nerve fibre. *The Journal of Physiology*.

[Hodgkin and Huxley, 1952] Hodgkin, A. L. and Huxley, A. F. (1952). A quantitative description of membrane current and its application to conduction and excitation in nerve. *The Journal of Physiology*, (117):500–544.

[Howarth, 1975] Howarth, J. V. (1975). Heat production non-myelinated nerves. *Philosophical transactions of the Royal Society of London. Series B, Biological sciences*.

[Howarth et al., 1968] Howarth, J. V., Keynes, R. D., and Ritchie, J. M. (1968). The origin of the initial heat associated with a single impulse in mammalian non-myelinated nerve fibres. *The Journal of Physiology*.

[Hutter and Bechhoefer, 1993] Hutter, J. L. and Bechhoefer, J. (1993). Calibration of atomic-force microscope tips. *Review of Scientific Instruments*, 64(7):1868–1873.

[Ingber, 1991] Ingber, D. (1991). Integrins as mechanochemical transducers. *Current Opinion in Cell Biology*.

[Ingber, 1997] Ingber, D. E. (1997). Tensegrity: the Architectural Basis of Cellular Mechanotransduction. *Annual Review of Physiology*, 59(1):575–599.

[Ingber, 2003] Ingber, D. E. (2003). Mechanobiology and diseases of mechanotransduction. *Annals of Medicine*, 35(8):564–577.

[Ito et al., 2013] Ito, D., Komatsu, T., and Gohara, K. (2013). Measurement of saturation processes in glutamatergic and GABAergic synapse densities during long-term development of cultured rat cortical networks. *Brain Research*.

[Iwasa and Tasaki, 1980] Iwasa, K. and Tasaki, I. (1980). Mechanical changes in squid giant axons associated with production of action potentials. *Topics in Catalysis*.

[Iwasa et al., 1980] Iwasa, K., Tasaki, I., and Gibbons, R. C. (1980). Swelling of nerve fibers associated with action potentials. *Science*.

[Iyer et al., 2009] Iyer, S., Gaikwad, R. M., Subba-Rao, V., Woodworth, C. D., and Sokolov, I. (2009). AFM Detects Differences in the Surface Brush on Normal and Cancerous Cervical Cells. *Nature Nanotechnology*, 4(6):389–393.

[Jäckel et al., 2012] Jäckel, D., Frey, U., Fiscella, M., Franke, F., and Hierlemann, A. (2012). Applicability of independent component analysis on high-density microelectrode array recordings. *Journal of Neurophysiology*, 108(1):334–348.

[Jacot et al., 2010] Jacot, J. G., Martin, J. C., and Hunt, D. L. (2010). Mechanobiology of cardiomyocyte development. *Journal of Biomechanics*, 43(1):93–98.

[Jansen et al., 2015] Jansen, K. A., Donato, D. M., Balcioglu, H. E., Schmidt, T., Danen, E. H., and Koenderink, G. H. (2015). A guide to mechanobiology: Where biology and physics meet. *Biochimica et Biophysica Acta - Molecular Cell Research*, 1853(11):3043–3052.

[Johnson, 1982] Johnson, K. L. (1982). One Hundred Years of Hertz Contact. *Proceedings of the Institution of Mechanical Engineers*.

[Johnson et al., 2013] Johnson, V. E., Stewart, W., and Smith, D. H. (2013). Axonal pathology in traumatic brain injury. *Experimental Neurology*, 246:35–43.

[Johnson, K. L., Kendall, K. & Roberts, 1971] Johnson, K. L., Kendall, K. & Roberts, A. D. (1971). Surface energy and the contact of elastic solids. *Proceedings of the Royal Society of London. A. Mathematical and Physical Sciences*, 324(1558):301–313.

[Johnston and Wu, 1995] Johnston and Wu (1995). *Foundations of cellular neurophysiology.*

[Kandel et al., 2000] Kandel, E. R., Schwartz, J. H., and Jessell, T. M. (2000). *Principles of Neural Science, fourth addition.*

[Kaneta et al., 2001] Kaneta, T., Makihara, J., and Imasaka, T. (2001). An "optical channel": A technique for the evaluation of biological cell elasticity. *Analytical Chemistry.*

[Kilinc et al., 2008] Kilinc, D., Gallo, G., and Barbee, K. A. (2008). Mechanically-induced membrane poration causes axonal beading and localized cytoskeletal damage. *Experimental Neurology*, 212(2):422–430.

[Kim et al., 2009] Kim, D.-H., Wong, P. K., Park, J., Levchenko, A., and Sun, Y. (2009). Microengineered Platforms for Cell Mechanobiology. *Annual Review of Biomedical Engineering*, 11(1):203–233.

[Kim et al., 2007] Kim, G. H., Kosterin, P., Obaid, A. L., and Salzberg, B. M. (2007). A mechanical spike accompanies the action potential in mammalian nerve terminals. *Biophysical Journal*, 92(9):3122–3129.

[Komarova et al., 2014] Komarova, S. V., Lopez-Ayon, G. M., Liu, H. Y., Xing, S., Maria, O. M., LeDue, J. M., Bourque, H., and Grutter, P. (2014). Local membrane deformation and micro-injury lead to qualitatively different responses in osteoblasts. *F1000Research.*

[Krieg et al., 2019] Krieg, M., Fläschner, G., Alsteens, D., Gaub, B. M., Roos, W. H., Wuite, G. J. L., Gaub, H. E., Gerber, C., Dufrêne, Y. F., and Müller, D. J. (2019). Atomic force microscopy-based mechanobiology. *Nature Reviews Physics*, 1(1):41–57.

[Kuznetsova et al., 2007] Kuznetsova, T. G., Starodubtseva, M. N., Yegorenkov, N. I., Chizhik, S. A., and Zhdanov, R. I. (2007). Atomic force microscopy probing of cell elasticity. *Micron*, 38(8):824–833.

[Ladjal et al., 2009] Ladjal, H., Hanus, J. L., Pillarisetti, A., Keefer, C., Ferreira, A., and Desai, J. P. (2009). Atomic force microscopy-based single-cell indentation: Experimentation and finite element simulation. In *2009 IEEE/RSJ International Conference on Intelligent Robots and Systems, IROS 2009*.

[Lamontagne et al., 2008] Lamontagne, C. A., Cuerrier, C. M., and Grandbois, M. (2008). AFM as a tool to probe and manipulate cellular processes. *Pflugers Archiv European Journal of Physiology*, 456(1):61–70.

[Lechasseur et al., 2011] Lechasseur, Y., Dufour, S., Lavertu, G., Bories, C., Deschênes, M., Vallée, R., and De Koninck, Y. (2011). A microprobe for parallel optical and electrical recordings from single neurons in vivo. *Nature Methods*, 8(4):319–325.

[Lekka et al., 2012] Lekka, M., Gil, D., Pogoda, K., Dulińska-Litewka, J., Jach, R., Gostek, J., Klymenko, O., Prauzner-Bechcicki, S., Stachura, Z., Wiltowska-Zuber, J., Okoń, K., and Laidler, P. (2012). Cancer cell detection in tissue sections using AFM. *Archives of Biochemistry and Biophysics*, 518(2):151–156.

[Lekka and Laidler, 2009] Lekka, M. and Laidler, P. (2009). Applicability of AFM in cancer detection. *Nature Nanotechnology*, 4(2):72.

[Li et al., 1999] Li, H., Alonso-Vanegas, M., Colicos, M. A., Jung, S. S., Lochmuller, H., Sadikot, A. F., Snipes, G. J., Seth, P., Karpati, G., and Nalbantoglu, J. (1999). Intracerebral adenovirus-mediated p53 tumor suppressor gene therapy for experimental human glioma. *Clinical Cancer Research*.

[Livi et al., 2010] Livi, P., Heer, F., Frey, U., Bakkum, D. J., and Hierlemann, A. (2010). Compact voltage and current stimulation buffer for high-density microelectrode arrays. *IEEE Transactions on Biomedical Circuits and Systems*, 4(6 PART 1):372–378.

[Maccione et al., 2012] Maccione, A., Garofalo, M., Nieus, T., Tedesco, M., Berdondini, L., and Martinoia, S. (2012). Multiscale functional connectivity estimation on low-density neuronal cultures recorded by high-density CMOS Micro Electrode Arrays. *Journal of Neuroscience Methods*.

[Magdesian et al., 2017] Magdesian, M. H., Anthonisen, M., Monserratt Lopez-Ayon, G., Chua, X. Y., Rigby, M., and Grütter, P. (2017). Rewiring neuronal circuits: A new method for fast neurite extension and functional neuronal connection. *Journal of Visualized Experiments*.

[Magdesian et al., 2016] Magdesian, M. H., Lopez-Ayon, G. M., Mori, M., Boudreau, D., Goulet-Hanssens, A., Sanz, R., Miyahara, Y., Barrett, C. J., Fournier, A. E., De Koninck, Y., and Grűtter, P. (2016). Rapid mechanically controlled rewiring of neuronal circuits. *Journal of Neuroscience*, 36(3):979–987.

[Magdesian et al., 2012] Magdesian, M. H., Sanchez, F. S., Lopez, M., Thostrup, P., Durisic, N., Belkaid, W., Liazoghli, D., Grütter, P., and Colman, D. R. (2012). Atomic force microscopy reveals important differences in axonal resistance to injury. *Biophysical Journal*, 103(3):405–414.

[Maia and Kutz, 2014] Maia, P. D. and Kutz, J. N. (2014). Compromised axonal functionality after neurodegeneration, concussion and/or traumatic brain injury. *Journal of Computational Neuroscience*, 37(2):317–332.

[Mariappan et al., 2010] Mariappan, Y. K., Glaser, K. J., and Ehman, R. L. (2010). Magnetic resonance elastography: A review.

[Martin et al., 2013] Martin, M., Benzina, O., Szabo, V., Végh, A. G., Lucas, O., Cloitre, T., Scamps, F., and Gergely, C. (2013). Morphology and Nanomechanics of Sensory Neurons Growth Cones following Peripheral Nerve Injury. *PLoS ONE*.

[Mishra and Majhi, 2019] Mishra, A. and Majhi, S. K. (2019). A comprehensive survey of recent developments in neuronal communication and computational neuroscience. *Journal of Industrial Information Integration*, 13(November):40–54.

[Müller et al., 2012] Müller, J., Bakkum, D., and Hierlemann, A. (2012). Submillisecond closed-loop feedback stimulation between arbitrary sets of individual neurons. *Frontiers in Neural Circuits*, 6(DEC):1–11.

[Müller et al., 2015] Müller, J., Ballini, M., Livi, P., Chen, Y., Radivojevic, M., Shadmani, A., Viswam, V., Jones, I. L., Fiscella, M., Diggelmann, R., Stettler, A., Frey, U., Bakkum, D. J., and Hierlemann, A. (2015). High-resolution CMOS MEA platform to study neurons at subcellular, cellular, and network levels. *Lab on a Chip*, 15(13):2767–2780.

[Mustata et al., 2010] Mustata, M., Ritchie, K., and McNally, H. A. (2010). Neuronal elasticity as measured by atomic force microscopy. *Journal of Neuroscience Methods*, 186(1):35–41.

[Nelson et al., 2008] Nelson, M. J., Pouget, P., Nilsen, E. A., Patten, C. D., and Schall, J. D. (2008). Review of signal distortion through metal microelectrode recording circuits and filters. *Journal of Neuroscience Methods*.

[Notbohm et al., 2012] Notbohm, J., Poon, B., and Ravichandran, G. (2012). Analysis of nanoindentation of soft materials with an atomic force microscope. *Journal of Materials Research*, 27(1):229–237.

[Obien et al., 2015] Obien, M. E. J., Deligkaris, K., Bullmann, T., Bakkum, D. J., and Frey, U. (2015). Revealing neuronal function through microelectrode array recordings. *Frontiers in Neuroscience*, 9(JAN):423.

[Obien et al., 2013] Obien, M. E. J., Hierlemann, A., and Frey, U. (2013). Blind Localization of a Stimulation Electrode Using a High-Density Microelectrode Array. *35th Annual International Conference of the IEEE EMBS*, page SaB08.8.

[Oh et al., 2012] Oh, S., Fang-Yen, C., Choi, W., Yaqoob, Z., Fu, D., Park, Y., Dassari, R. R., and Feld, M. S. (2012). Label-free imaging of membrane potential using membrane electromotility. *Biophysical Journal*, 103(1):11–18.

[Oudit and Backx, 2018] Oudit, G. Y. and Backx, P. H. (2018). *Voltage-Gated Potassium Channels*. Elsevier Inc., seventh ed edition.

[Parkington and Coleman, 2012] Parkington, H. C. and Coleman, H. A. (2012). Intracellular 'Sharp' Microelectrode Recording. In *Essential Guide to Reading Biomedical Papers*.

[Pine, 2006] Pine, J. (2006). A history of MEA development. In *Advances in Network Electrophysiology: Using Multi-Electrode Arrays*.

[Puig-De-Morales et al., 2001] Puig-De-Morales, M., Grabulosa, M., Alcaraz, J., Mullol, J., Maksym, G. N., Fredberg, J. J., and Navajas, D. (2001). Measurement of cell microrheology by magnetic twisting cytometry with frequency domain demodulation. *Journal of Applied Physiology.*

[Puttock and Thwaite, 1969] Puttock, M. J. and Thwaite, E. G. (1969). Elastic Compression of Spheres and Cylinders at Point and Line Contact. *National Standards Laboratory Technical Paper*, 25(25):64.

[Quiroga, 2012] Quiroga, R. Q. (2012). Spike sorting.

[Quiroga et al., 2004] Quiroga, R. Q., Nadasdy, Z., and Ben-Shaul, Y. (2004). Unsupervised spike detection and sorting with wavelets and superparamagnetic clustering. *Neural Computation*, 16(8):1661–1687.

[Radivojevic et al., 2016] Radivojevic, M., Jäckel, D., Altermatt, M., Müller, J., Viswam, V., Hierlemann, A., and Bakkum, D. J. (2016). Electrical Identification and Selective Microstimulation of Neuronal Compartments Based on Features of Extracellular Action Potentials. *Scientific Reports*, 6(July):1–20.

[Rajagopalan and Saif, 2011] Rajagopalan, J. and Saif, M. T. A. (2011). MEMS sensors and microsystems for cell mechanobiology. *Journal of Micromechanics and Microengineering.*

[Ramon y Cajal, 1928] Ramon y Cajal, S. (1928). *Degeneration and regeneration of the nervous system.* Clarendon Press, Oxford, England.

[Rico et al., 2007] Rico, F., Roca-Cusachs, P., Sunyer, R., Farré, R., and Navajas, D. (2007). Cell dynamic adhesion and elastic properties probed with cylindrical atomic force microscopy cantilever tips. In *Journal of Molecular Recognition.*

[Robinson, 1968] Robinson, D. A. (1968). The Electrical Properties of Metal Microelectrodes. *Proceedings of the IEEE.*

[Roduit et al., 2009] Roduit, C., Sekatski, S., Dietler, G., Catsicas, S., Lafont, F., and Kasas, S. (2009). Stiffness tomography by atomic force microscopy. *Biophysical Journal*, 97(2):674–677.

[Sarkar and Rybenkov, 2016] Sarkar, R. and Rybenkov, V. V. (2016). A Guide to Magnetic Tweezers and Their Applications. *Frontiers in Physics*, 4(December).

[Schwartz and Ramos, 2020] Schwartz, M. and Ramos, J. M. P. (2020). A 20-Year Journey from Axonal Injury to Neurodegenerative Diseases and the Prospect of Immunotherapy for Combating Alzheimer's Disease. *Journal of Immunology*, 204(2).

[Shenai et al., 2004] Shenai, M. B., Putchakayala, K. G., Hessler, J. A., Orr, B. G., Holl, M. M., and Baker, J. R. (2004). A novel MEA/AFM platform for measurement of real-time, nanometric morphological alterations of electrically stimulated neuroblastoma cells. *IEEE Transactions on Nanobioscience*.

[Simmons et al., 2011] Simmons, C. S., Sim, J. Y., Baechtold, P., Gonzalez, A., Chung, C., Borghi, N., and Pruitt, B. L. (2011). Integrated strain array for cellular mechanobiology studies. *Journal of Micromechanics and Microengineering*.

[Smith et al., 2005] Smith, B. A., Tolloczko, B., Martin, J. G., and Grütter, P. (2005). Probing the viscoelastic behavior of cultured airway smooth muscle cells with atomic force microscopy: Stiffening induced by contractile agonist. *Biophysical Journal*, 88(4):2994–3007.

[Sneddon, 1965] Sneddon, I. N. (1965). The relation between load and penetration in the axisymmetric boussinesq problem for a punch of arbitrary profile. *International Journal of Engineering Science*, 3(1):47–57.

[Sniadecki and Chen, 2007] Sniadecki, N. J. and Chen, C. S. (2007). Microfabricated Silicone Elastomeric Post Arrays for Measuring Traction Forces of Adherent Cells. *Methods in Cell Biology*, 83(07):313–328.

[Sokolov, 2007] Sokolov, I. (2007). Atomic Force Microscopy in Cancer Cell Research. *Cancer Nanotechnology – Nanomaterials for Cancer Diagnosis and Therapy*, 1:1–17.

[Spedden and Staii, 2013] Spedden, E. and Staii, C. (2013). Neuron biomechanics probed by atomic force microscopy. *International Journal of Molecular Sciences*, 14(8):16124–16140.

[Spedden et al., 2012a] Spedden, E., White, J. D., Kaplan, D., and Staii, C. (2012a). Young's modulus of cortical and P19 derived neurons measured by atomic force microscopy. In *Materials Research Society Symposium Proceedings*, volume 1420, pages 7–12. Cambridge University Press.

[Spedden et al., 2012b] Spedden, E., White, J. D., Naumova, E. N., Kaplan, D. L., and Staii, C. (2012b). Elasticity maps of living neurons measured by combined fluorescence and atomic force microscopy. *Biophysical Journal*, 103(5):868–877.

[Star et al., 2002] Star, E. N., Kwiatkowski, D. J., and Murthy, V. N. (2002). Rapid turnover of actin in dendritic spines and its regulation by activity. *Nature Neuroscience*.

[Stichel and Müller, 1998] Stichel, C. C. and Müller, H. W. (1998). Experimental strategies to promote axonal regeneration after traumatic central nervous system injury. *Progress in Neurobiology*, 56(2):119–148.

[Strick et al., 1996] Strick, T. R., Allemand, J. F., Bensimon, D., Bensimon, A., and Croquette, V. (1996). The elasticity of a single supercoiled DNA molecule. *Science*.

[Stylianou et al., 2018] Stylianou, A., Lekka, M., and Stylianopoulos, T. (2018). AFM assessing of nanomechanical fingerprints for cancer early diagnosis and classification: From single cell to tissue level. *Nanoscale*, 10(45):20930–20945.

[Suminaite et al., 2019] Suminaite, D., Lyons, D. A., and Livesey, M. R. (2019). Myelinated axon physiology and regulation of neural circuit function. *Glia*, 67(11):2050–2062.

[Tan et al., 2003] Tan, J. L., Tien, J., Pirone, D. M., Gray, D. S., Bhadriraju, K., and Chen, C. S. (2003). Cells lying on a bed of microneedles: An approach to isolate mechanical force. *Proceedings of the National Academy of Sciences of the United States of America*.

[Tasaki, 1988] Tasaki, I. (1988). A macromolecular approach to excitation phenomena: mechanical and thermal changes in nerve during excitation.

[Tasaki and Byrne, 1982] Tasaki, I. and Byrne, P. M. (1982). Tetanic contraction of the crab nerve evoked by repetitive stimulation. *Biochemical and Biophysical Research Communications*.

[Tasaki and Byrne, 1988] Tasaki, I. and Byrne, P. M. (1988). Large mechanical changes in the bullfrog olfactory bulb evoked by afferent fiber stimulation. *Brain Research*.

[Tasaki and Byrne, 1990] Tasaki, I. and Byrne, P. M. (1990). Volume expansion of nonmyelinated nerve fibers during impulse conduction. *Biophysical Journal*, 57(3):633–635.

[Tasaki and Byrne, 1992] Tasaki, I. and Byrne, P. M. (1992). Rapid Structural Changes in Nerve Fibers. *Biochemical and Biophysical Research Communications*, 188(2):559–564.

[Tasaki and Iwasa, 1982] Tasaki, I. and Iwasa, K. (1982). Further Studies of Rapid Mechanical Changes in Squid Giant Axon Associated with Action Potential Production. *The Japanese Journal of Physiology*, 32(4):505–518.

[Tasaki et al., 1989] Tasaki, I., Kusano, K., and Byrne, P. M. (1989). Rapid mechanical and thermal changes in the garfish olfactory nerve associated with a propagated impulse. *Biophysical Journal*, 55(6):1033–1040.

[Tator et al., 2007] Tator, C., Bray, G., and Morin, D. (2007). The CBANCH report - The burden of neurological diseases, disorders, and injuries in Canada. *Canadian Journal of Neurological Sciences*, 34(3):268–269.

[Taylor et al., 2010] Taylor, A. M., Dieterich, D. C., Ito, H. T., Kim, S. A., and Schuman, E. M. (2010). Microfluidic Local Perfusion Chambers for the Visualization and Manipulation of Synapses. *Neuron*.

[Thomas et al., 1972] Thomas, C. A., Springer, P. A., Loeb, G. E., Berwald-Netter, Y., and Okun, L. M. (1972). A miniature microelectrode array to monitor the bioelectric activity of cultured cells. *Experimental Cell Research*.

[Tian et al., 2017] Tian, J., Tu, C., Huang, B., Liang, Y., Zhou, J., and Ye, X. (2017). Study of the union method of microelectrode array and AFM for the recording of electromechanical activities in living cardiomyocytes. *European Biophysics Journal*, 46(5):495–507.

[Tran et al., 2018] Tran, A. P., Warren, P. M., and Silver, J. (2018). The biology of regeneration failure and success after spinal cord injury. *Physiological Reviews*, 98(2):881–917.

[Trivedi et al., 2006] Trivedi, A., Olivas, A. D., and Noble-Haeusslein, L. J. (2006). Inflammation and spinal cord injury: Infiltrating leukocytes as determinants of injury and repair processes. *Clinical Neuroscience Research*.

[Tyler, 2012] Tyler, W. J. (2012). The mechanobiology of brain function. *Nature Reviews Neuroscience*, 13(12):867–878.

[Venkatesh et al., 2013] Venkatesh, S. K., Yin, M., and Ehman, R. L. (2013). Magnetic resonance elastography of liver: Technique, analysis, and clinical applications.

[Viswam et al., 2018] Viswam, V., Obien, M., Frey, U., Franke, F., and Hierlemann, A. (2018). Acquisition of bioelectrical signals with small electrodes. *2017 IEEE Biomedical Circuits and Systems Conference, BioCAS 2017 - Proceedings*, 2018-Janua:1–4.

[Vogel, 2006] Vogel, V. (2006). Mechanotransduction Involving Multimodular Proteins: Converting Force into Biochemical Signals.

[Vogel, 2017] Vogel, V. (2017). Unraveling the Mechanobiology of Extracellular Matrix.

[Wang et al., 2019] Wang, L., Wang, L., Xu, L., and Chen, W. (2019). Finite Element Modelling of Single Cell Based on Atomic Force Microscope Indentation Method. *Computational and Mathematical Methods in Medicine*.

[Wickenden, 2014] Wickenden, A. D. (2014). Overview of electrophysiological techniques. *Current Protocols in Pharmacology*, (SUPPL.64):1–17.

[Yang et al., 2018] Yang, Y., Liu, X. W., Wang, H., Yu, H., Guan, Y., Wang, S., and Tao, N. (2018). Imaging Action Potential in Single Mammalian Neurons by Tracking the Accompanying Sub-Nanometer Mechanical Motion. *ACS Nano*.

[Yiu and He, 2003] Yiu, G. and He, Z. (2003). Signaling mechanisms of the myelin inhibitors of axon regeneration. *Current Opinion in Neurobiology*, 13(5):545–551.

[Yiu and He, 2006] Yiu, G. and He, Z. (2006). Glial inhibition of CNS axon regeneration. *Nature Reviews Neuroscience*, 7(8):617–627.

[Zaza, 2000] Zaza, A. (2000). The cardiac action potential. *An Introduction to Cardiac Electrophysiology*, pages 59–82.

[Zemła et al., 2018] Zemła, J., Danilkiewicz, J., Orzechowska, B., Pabijan, J., Seweryn, S., and Lekka, M. (2018). Atomic force microscopy as a tool for assessing the cellular elasticity and adhesiveness to identify cancer cells and tissues. *Seminars in Cell and Developmental Biology*, 73:115–124.

# KEY TO ABBREVIATIONS

ADC: Analog-to-digital conversion . . . 47

AFM: Atomic force microscope . . . 3

AP: Action potential . . . 38

AW: Action waves . . . 74

CBARC: Concentric bipolar microelectrode . . . 115

CMOS: Complementary metal oxide semiconductor . . . 46

CMOS-HDMEA: Complementary metal oxide semiconductor based high density microelectrode array . . . 48

CMOS-MEA: Complementary metal oxide semiconductor microelectrode array 3

CNS: Central nervous system . . . 3

CSPG: Chondroitin sulphate proteoglycans . . . 5

DAC: Digital-to-analog conversion . . . 54

DC: Direct current . . . 54

DMT: Derjaguin-Müller-Toporov . . . 19

DRG: Dorsal root ganglion . . . 22

ECM: Extracellular matrix . . . 10

EM: Elastic modulus 20

FD: Force distance 18

FPGA: Field-programmable gate array 55

FWHM: Field-width half-maximum 61

GXSM: Gnome X scanning microscopy 105

HDMEA: High density microelectrode array 46

iPS: Induced pluripotent stem 121

JKR: Johnson-Kendall-Roberts 19

LG: Lateral giant 79

LVDS: Low-voltage differential signalling 98

MEA: Multielectrode array 8

MG: Medial giant 79

MRE: Magnetic resonance elastography 13

MRI: Magnetic resonance imaging 13

PCB: Printed circuit board 55

PCIE: Peripheral component interconnect express 98

PDMS: Polydimethysiloxane 23

Pt: Platinum 47

Pt-black: Platinum-black 56

SNR: Signal-to-noise ratio 47

# SUPPLEMENTARY MATERIAL

## S1 Chapter 2: Derivation of the sphere on a sphere contact mechanics model

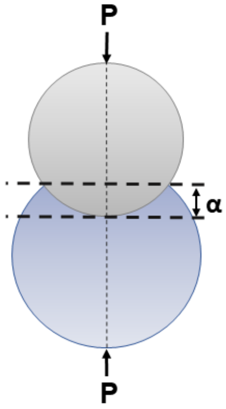

Figure S1: **Illustration of two spheres in contact.**

Definition of symbols and suffixes:

- $_1$: Suffix for sphere 1, i.e. the cell
- $_2$: Suffix for sphere 2, i.e. the bead
- $P$: Total force applied
- $\alpha$: Total elastic compression at the point of contact
- $D$: Diameter of the sphere
- $E$: Young's modulus of the sphere
- $\sigma$: Poisson's ratio of the sphere

- $V$: $(1-\sigma^2)/\pi E$
- $M$: Slope of the line of best fit
- $b$: Constant from the line of best fit

Starting with the general case given by [Puttock and Thwaite, 1969], we have

$$\alpha = \frac{(3\pi)^{\frac{2}{3}}}{2} \cdot P^{\frac{2}{3}} \cdot (V_1 + V_2)^{\frac{2}{3}} \cdot \left( \frac{1}{D_1} + \frac{1}{D_2} \right)^{\frac{1}{3}}. \tag{VI.1}$$

First, $V$ is replaced with $(1-\sigma^2)/\pi E$, to obtain

$$\alpha = \frac{(3\pi)^{\frac{2}{3}}}{2} \cdot P^{\frac{2}{3}} \cdot \left( \frac{1-\sigma_1^2}{\pi E_1} + \frac{1-\sigma_2^2}{\pi E_2} \right)^{\frac{2}{3}} \cdot \left( \frac{1}{D_1} + \frac{1}{D_2} \right)^{\frac{1}{3}}. \tag{VI.2}$$

Solving for $P$, we get

$$P = \frac{(2\alpha)^{\frac{2}{3}}}{3} \cdot \frac{1}{\left( \frac{1-\sigma_1^2}{E_1} + \frac{1-\sigma_2^2}{E_2} \right) \cdot \left( \frac{1}{D_1} + \frac{1}{D_2} \right)^{\frac{1}{2}}}. \tag{VI.3}$$

The line of best fit is given by $P = \alpha^{\frac{3}{2}} \cdot M + b$, where the expression for $M$ is

$$M = \frac{\sqrt{8}}{3} \cdot \frac{1}{\left( \frac{1-\sigma_1^2}{E_1} + \frac{1-\sigma_2^2}{E_2} \right) \cdot \left( \frac{1}{D_1} + \frac{1}{D_2} \right)^{\frac{1}{2}}}. \tag{VI.4}$$

Solving for $E_1$, we will get the equation for the elastic modulus of the cell:

$$\boldsymbol{E_1 = \frac{1 - \sigma_1^2}{\frac{\sqrt{8}}{3M\cdot\left(\frac{1}{D_1}+\frac{1}{D_2}\right)^{\frac{1}{2}}} - \frac{1-\sigma_2^2}{E_2}}} \tag{VI.5}$$

## S2 Chapter 2: Derivation of the sphere on a plane contact mechanics model

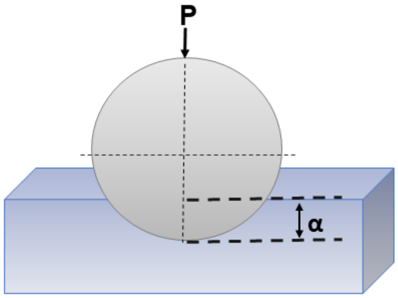

Figure S2: **Illustration of a sphere in contact with a plane.**

Definition of symbols and suffixes:

- $_1$: Suffix for the plane, i.e. the cell
- $_2$: Suffix for the sphere, i.e. the bead
- $P$: Total force applied
- $\alpha$: Total elastic compression at the point of contact
- $D$: Diameter of the sphere
- $E$: Young's modulus of the sphere or plane
- $\sigma$: Poisson's ratio of the sphere
- $V$: $(1-\sigma^2)/\pi E$
- $M$: Slope of the line of best fit
- $b$: Constant from the line of best fit

Starting with the general case given by [Puttock and Thwaite, 1969], we have

$$\alpha = \frac{(3\pi)^{\frac{2}{3}}}{2} \cdot P^{\frac{2}{3}} \cdot (V_1 + V_2)^{\frac{2}{3}} \cdot \left(\frac{1}{D}\right)^{\frac{1}{3}}. \tag{VI.6}$$

$V$ is replaced with $(1-\sigma^2)/\pi E$, to obtain

$$\alpha = \frac{(3\pi)^{\frac{2}{3}}}{2} \cdot P^{\frac{2}{3}} \cdot \left(\frac{1-\sigma_1^2}{\pi E_1} + \frac{1-\sigma_2^2}{\pi E_2}\right)^{\frac{2}{3}} \cdot \left(\frac{1}{D}\right)^{\frac{1}{3}}. \tag{VI.7}$$

Solving for $P$, we arrive to

$$P = \frac{(2\alpha)^{\frac{2}{3}}}{3} \cdot \frac{1}{\left(\frac{1-sigma_1^2}{E_1} + \frac{1-sigma_2^2}{E_2}\right) \cdot \left(\frac{1}{D}\right)^{\frac{1}{2}}} \tag{VI.8}$$

The line of best fit is given by $P = \alpha^{\frac{3}{2}} \cdot M + b$, where the expression for $M$ is

$$M = \frac{\sqrt{8}}{3} \cdot \frac{1}{\left(\frac{1-sigma_1^2}{E_1} + \frac{1-sigma_2^2}{E_2}\right) \cdot \left(\frac{1}{D}\right)^{\frac{1}{2}}} \tag{VI.9}$$

Solving for $E_1$, we will get the equation for the elastic modulus of the cell:

$$\boldsymbol{E_1 = \frac{1-\sigma_1^2}{\frac{\sqrt{8D}}{3M} - \frac{1-sigma_2^2}{E_2}}} \tag{VI.10}$$

# S3 Chapter 2: Derivation of the sphere on a cylinder contact mechanics model

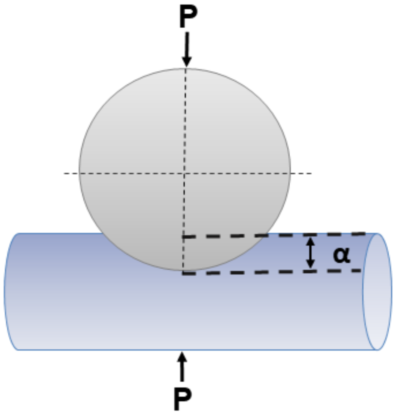

Figure S3: **Illustration of a sphere in contact with a cylinder.**

Definition of symbols and suffixes:

- $_1$: Suffix for the sphere
- $_2$: Suffix for the cylinder
- $P$: Total force applied
- $\alpha$: Total elastic compression at the point of contact
- $D$: Diameter of the sphere or cylinder
- $E$: Young's modulus of the sphere or cylinder
- $\sigma$: Poisson's ratio of the sphere or cylinder
- $V$: $(1-\sigma^2)/\pi E$
- $M$: Slope of the line of best fit
- $b$: Constant from the line of best fit
- $K$ and $-\frac{1}{e}\frac{dE}{de}$: Complete elliptic integrals of the first and second class with modulus $e$

Firstly, the ratio of $\frac{A}{B}$ and $\frac{1}{A}$ have to be calculated from the following equations:

$$\frac{A}{B} = \frac{\frac{1}{D_1}}{\frac{1}{D_1} + \frac{1}{D_2}} \tag{VI.11}$$

$$\frac{1}{A} = D_1 \tag{VI.12}$$

Following that, the values of $K$ and $-\frac{1}{e}\frac{dE}{de}$ were obtained and substituted into the general case equation given by [Puttock and Thwaite, 1969],

$$\alpha = \frac{2QP}{a} \cdot K \tag{VI.13}$$

where,

$$a = \left(\frac{2QP}{A} \cdot -\frac{1}{e}\frac{dE}{de}\right)^{\frac{1}{3}} \tag{VI.14}$$

Subbing in the expression for $a$, $Q = \frac{3}{4}(V_1 + V_2)$, and $V = \frac{1-sigma^2}{\pi E}$, into the general equation, we get:

$$\alpha = \frac{\left(\frac{11P}{4}\left(\frac{1-\sigma_1^2}{\pi E_1} + \frac{1-\sigma_2^2}{\pi E_2}\right)\right)^{\frac{2}{3}}}{\left(\frac{1}{A} \cdot -\frac{1}{e}\frac{dE}{de}\right)^{\frac{1}{3}}} \cdot K \tag{VI.15}$$

Solving for P,

$$P = \frac{\alpha^{\frac{3}{2}\left(\frac{1}{A}\cdot -\frac{1}{e}\frac{dE}{de}\right)^{\frac{1}{2}}}}{\frac{3}{2}K^{\frac{3}{2}}\left(\frac{1-\sigma_1^2}{\pi E_1} + \frac{1-\sigma_2^2}{\pi E_2}\right)} \tag{VI.16}$$

The line of best fit is given by $P = \alpha^{\frac{3}{2}} M + b$, where $M$ is

$$M = \frac{\left(\frac{1}{A} \cdot -\frac{1}{e}\frac{dE}{de}\right)^{\frac{1}{2}}}{\frac{3}{2}K^{\frac{3}{2}}\left(\frac{1-\sigma_1^2}{\pi E_1} + \frac{1-\sigma_2^2}{\pi E_2}\right)} \tag{VI.17}$$

Depending on the geometry of the cell and the cantilever tip, there are two sub-cases.

### Sub-case 1: Cantilever tip is spherical and the cell is cylindrical

Solving for $E_2$, the elastic modulus equation for the cell is given by

$$E_2 = \frac{1-\sigma_2^2}{\pi\left(\frac{2}{3} \cdot K^{-\frac{3}{2}} \cdot M^{-1} \cdot \left(\frac{1}{A} \cdot -\frac{1}{e}\frac{dE}{de}\right)^{\frac{1}{2}} - \frac{1-\sigma_1^2}{\pi E_1}\right)} \tag{VI.18}$$

### Sub-case 2: Cantilever tip is cylindrical and the cell is spherical

Solving for $E_1$, the elastic modulus equation for the cell is given by

$$E_2 = \frac{1-\sigma_1^2}{\pi\left(\frac{2}{3} \cdot K^{-\frac{3}{2}} \cdot M^{-1} \cdot \left(\frac{1}{A} \cdot -\frac{1}{e}\frac{dE}{de}\right)^{\frac{1}{2}} - \frac{1-\sigma_2^2}{\pi E_2}\right)} \tag{VI.19}$$

# S4 Chapter 3: CMOS-HDMEA standard operating procedures

**Connections:** The following shows the connections for the CMOS-HDMEA system, Figure S4. A DC power supply is used to power up the FPGA and LVDS circuit boards. The settings are $9.0V$ for the FPGA and $5.0V$. An ethernet cable connects the FPGA board to the laptop, which runs on CentOS 6. The LVDS board connects to the custom-printed circuit board via another ethernet cable. A CMOS-HDMEA chip can be plugged into any of the slots on the custom-printed circuit board.

**Start up commands:**

1. Verify that all the connections are as shown in Figure S4 and that the laptop is connected to the FPGA board.
2. Open up the terminal window and change directory to the recording folder of choice.
3. To start up, type

   ```
   mea_startup
   ```

   and press **Enter**. At this stage, all the control windows should be opened.
4. Find a terminal window that says **Neurolizer Linux 2.4.21 system**. In that window, type in the following and press **Enter**, in the following sequence:

   ```
   root

   ./run_lvds2.0.sh

   o

   a

   b

   a
   ```

5. Next, specify the port number:
   (a) a = Port 0

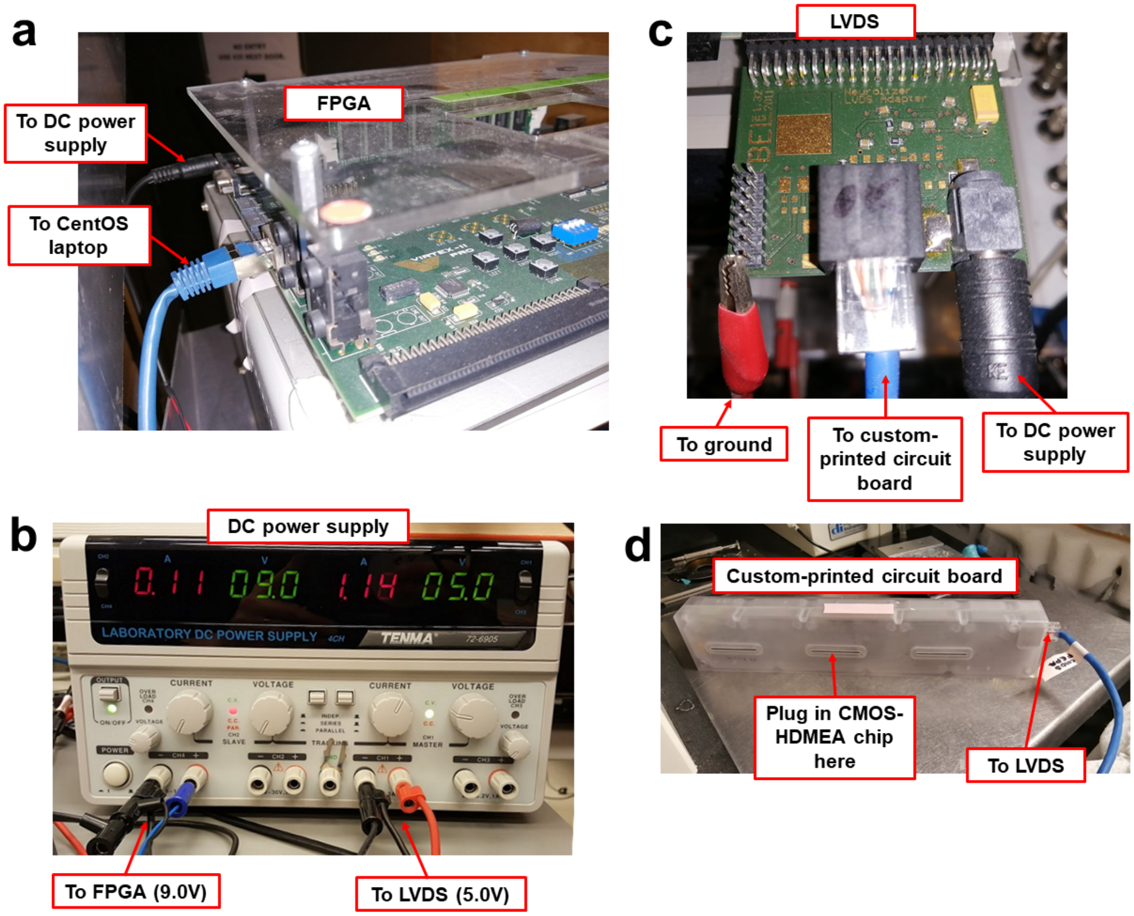

Figure S4: **CMOS-HDMEA system connections. a.** FPGA connection to a DC power supply and to the laptop. **b.** DC power supply connections and settings to the FPGA and LVDS sircuit boards. **c.** LVDS connections to the ground, DC power supply and custom-printed circuit board. **d.** Custom-printed circuit board showing the LVDS ethernet cable connection and plugs for the CMOS-HDMEA chips.

(b) b = Port 1
(c) c = Port 2
(d) d = Port 3
(e) e = Port 4 (This port is typically used for Pt-Black deposition.)

6. Set the reference voltage settings, the following is commonly used:

```
V2 160
```

7. Set the high pass cut off frequency, the following is commonly used:

```
M 1 1 255 ; M [port #] [enable = 1, disable = 0] [value 0 - 255]
```

8. Move over to **meabench** to adjust the parameters for the experiment.
9. To end and close the session, type in

```
CTRL + X
```

The following are common experimental settings in meabench.

**In HiDens Cmd Sender:**

- Check that the **Chip Addr:** corresponds to the plug where the chip is being plugged in in the custom-printed circuit board.
- In the **Amp** tab, set the gain settings, and click **send**.
- In the **Config** tab, locate the configuration file indicating the electrodes to be recorded from. Click **send** when the configuration has been loaded.
- In **Meabench** tab, under **Raw Stream**, click **start**, to start recording from the electrodes specified in the configuration.
- At this point, the signals should appear on the **Scope** window. If the signals are not there, select **True blue** from the drop window, select **Arrange**, and **Center**. Unchecking **Box** enables one to visualise the microelectrodes across the entire active MEA area.

## S5 Chapter 4: Bioscope II AFM modifications

Detailed below are the steps to run the Bioscope II AFM through GXSM-2.0 after removing the extender module. Firstly, hardware changes have to be made to the Bioscope II AFM and the resulting connections are as follows:

**Connections:**

1. Remove **Extender Module** from the main Bioscope II AFM circuitry and reconnect the system as follows, Figure S5.
   - Nanoscope Controller connects to the **NANOSCOPE CONTROLLER** pin in the Signal Access Module

   - **MICROSCOPE** pin from the Signal Access Module connects to the **CONTROLLER** pin in the Bioscope electronics box.
2. Connect the high voltage power supply to the Signal Access Module of the Bioscope II system and to the GXSM controller. Match up the corresponding connections according to Figure S6. Switch the toggels on the Signal Access Module from **Internal** to **External** when using with the GXSM controller.
3. Connect the deflection signal from the Signal Access Module to the GXSM controller and to an oscilloscope (optional). Deflection signal from the AFM cantilever can be extracted from channel **In0** of the Signal Access Module and transmitted to Channel Input **1** of the GXSM controller. An oscilloscope can be connected to either one of the channels to view the deflection signal in real time.
4. Connect the external stepper motor, as shown in Figure S9. A 5 pin cable from the original Bioscope II motor control box has to be removed and connected to a cable connected to the external stepper motor control box, Figure S9(a). The external stepper motor control box is then connected to the Signal Access Module **+15VDC** port, and connected to the GXSM controller in the **MOTOR** channel. Additionally, there is a switch labelled **UP** and **DOWN** on the external stepper motor control box to control the Z-direction of the AFM head. Check the direction of the stepper motor before running the AFM! An oscilloscope can be optionally connected to the **MOTOR** channel in the GXSM controller to visualise the stepper motor activity.

5. Connect the GXSM controller to the laptop via a USB cable, as shown in Figure S8.

**Standard operating procedures:**

1. Check that all the connections are properly wired and well connected.
2. Power up the Bioscope II and GXSM components.
3. Prepare the extended cantilever and load the cantilever onto the AFM head.
4. Using the Nanoscope software, align the laser beam onto the back of the cantilever tip. Try to obtain the highest sum possible.
5. Once the laser has been aligned, switch over to **IMAGE** mode in the Nanoscope software.
6. Switch over to GXSM controls.
7. In the terminal window, type

```
gxsm2
```

8. Set the experimental parameters in the **SR DSP Control** window according to the experiments to be performed.
9. To run the stepper motor, the following steps have to be performed in order.
10. Flip the directional switch on the external stepper motor box to **UP**, to avoid crashing the tip or AFM head into the sample.
11. In the **Mover Control** window, **Auto** tab, set the **GPIO** to **000Fh**, and click **Run**. At this point, red squares should appear at the bottom of the **PanView OSD** window.
12. Set the **GPIO** settings back to **000h**, and click **Run**. The red squares should turn black.
13. In the **Config** tab, set the **Curve Mode** to **Pulse positive**, and **Output on** to **X-MotorCH[7]**.
14. To set the step size for the stepper motor, return to the **Auto** tab, and set **Amplitude** to **3.00V**, **Duration** to **0.100 ms**, and **Max Steps** to **5000**.
15. The stepper motor can be made to run automatically by clicking the **GO** button. Be sure to flip the directional switch of the external stepper motor box before running.
16. Detailed information on GXSM 2 installation and software operations can be found at the Nanoscience and SPM Group page (https://spm.physics.mcgill.ca/links/gxsm-user-notes) or the GXSM discussion page (https://sourceforge.net/p/gxsm/discussion/40918/).

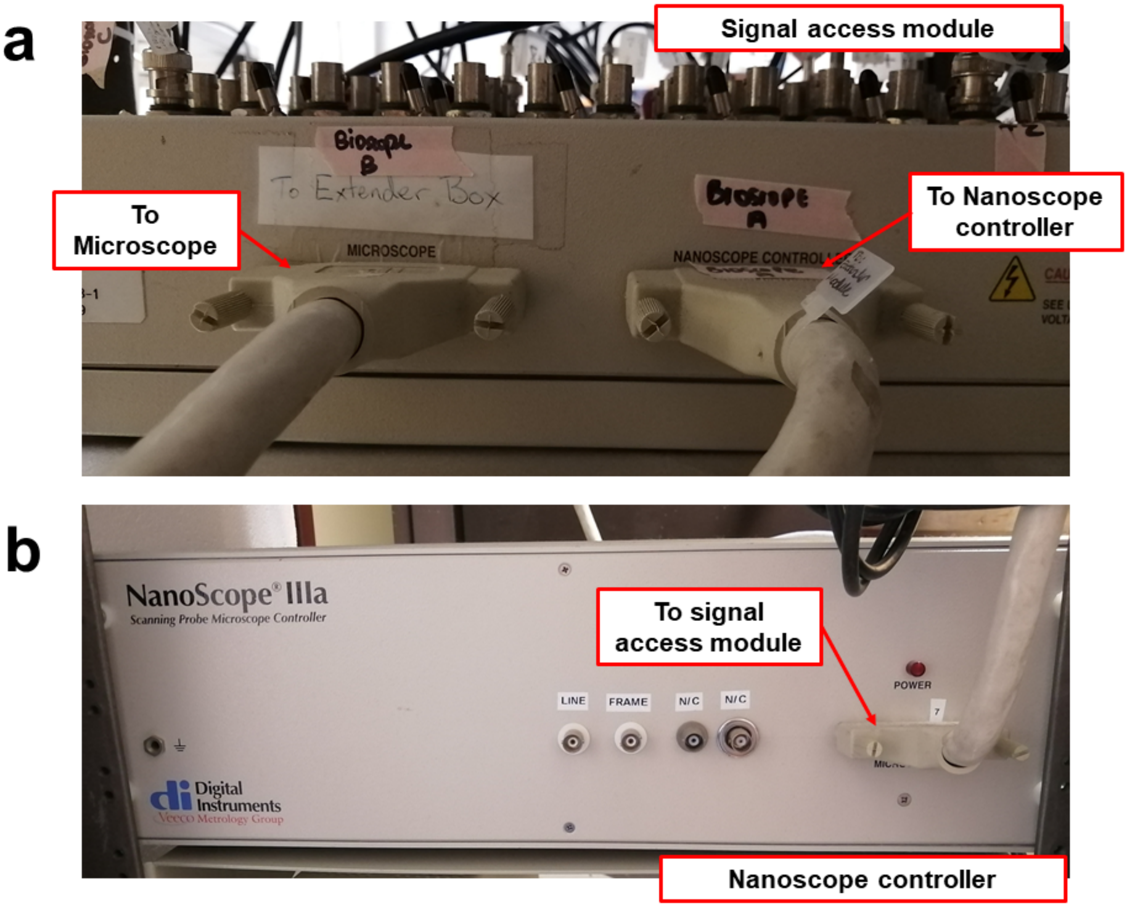

Figure S5: **Bioscope II connections without the Extender module. a.** The Signal Access Module connects to the Nanoscope controller through the **NANOSCOPE CONTROLLER** pin, and to Bioscope electronics box through the **MICROSCOPE** pin. **b.** The Nanoscope controller connects to the Signal Access Module.

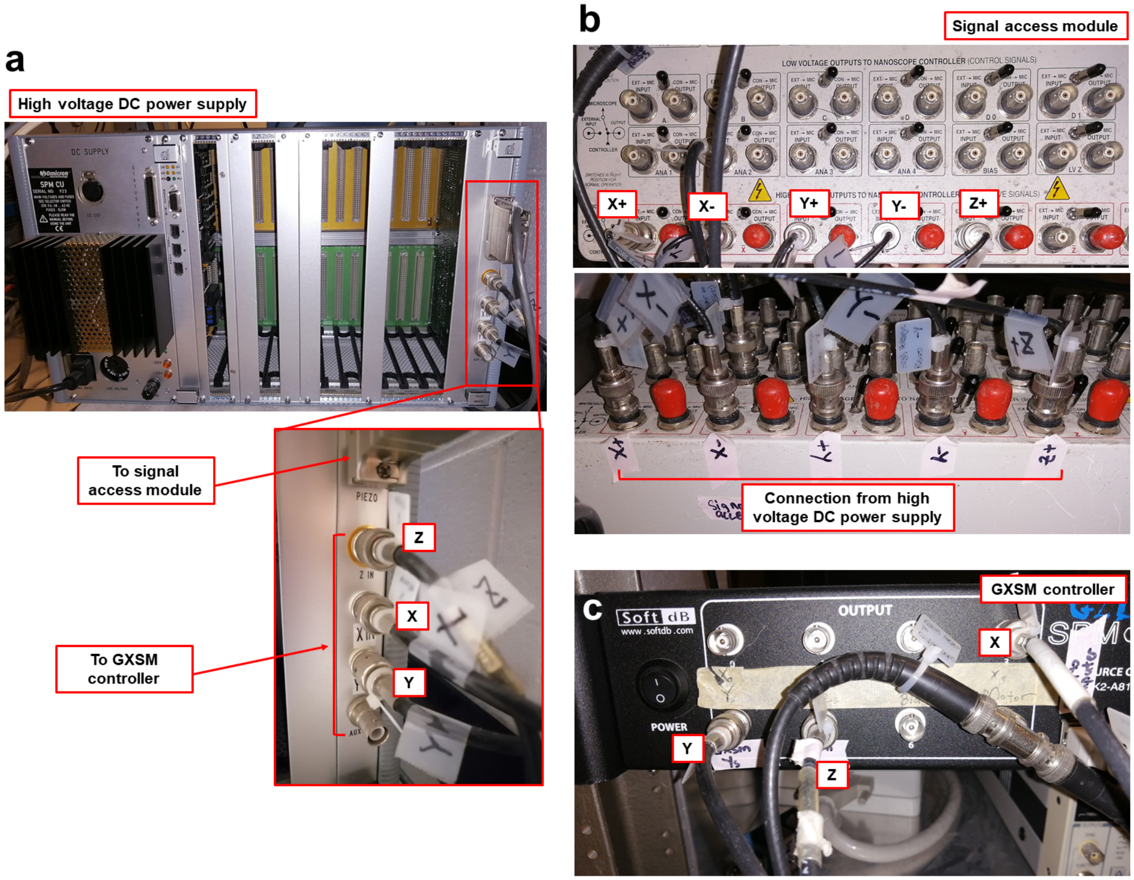

Figure S6: **High voltage power supply connections. a.** Back of the high voltage power supply. Connection labelled **PIEZO** connects to the Signal Access Module. Connections labelled **Z IN**, **Y IN**, and **X IN** connect to the GXSM controller. **b.** Connections in the Signal Access Module. The corresponding positions for the **X+**, **X-**, **Y+**, **Y-**, and **Z** connections are shown in the figure. **c.** Connections in the GXSM controller. The corresponding positions for the **X**, **Y**, and **Z** connections from the high voltage power supply are shown in the figure.

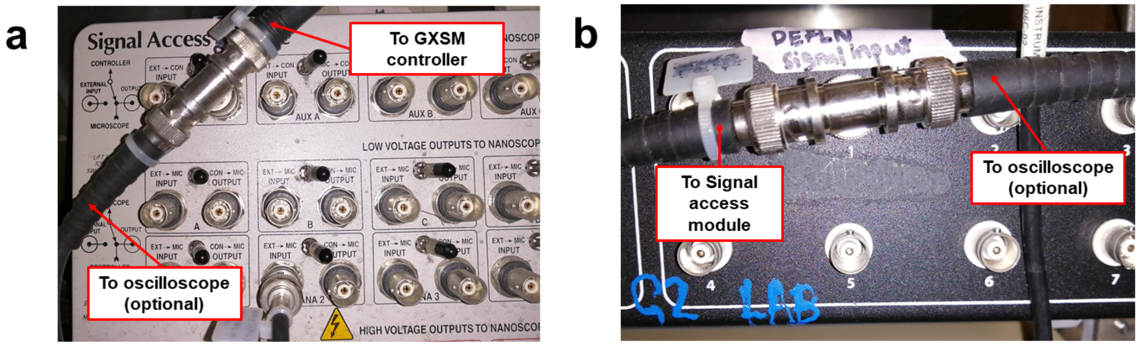

**Signal access module** **GXSM controller**

Figure S7: **Deflection signal connections.** The deflection signal connects from the **In0** channel of the Signal Access Module to the Channel Input **1** on the GXSM controller.

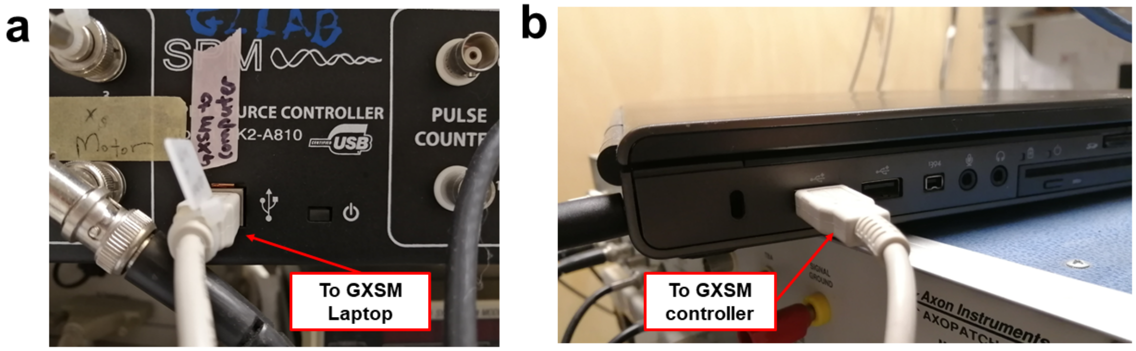

Figure S8: **GXSM laptop connections.** Figures show the output connection to the laptop controlling the GXSM controller.

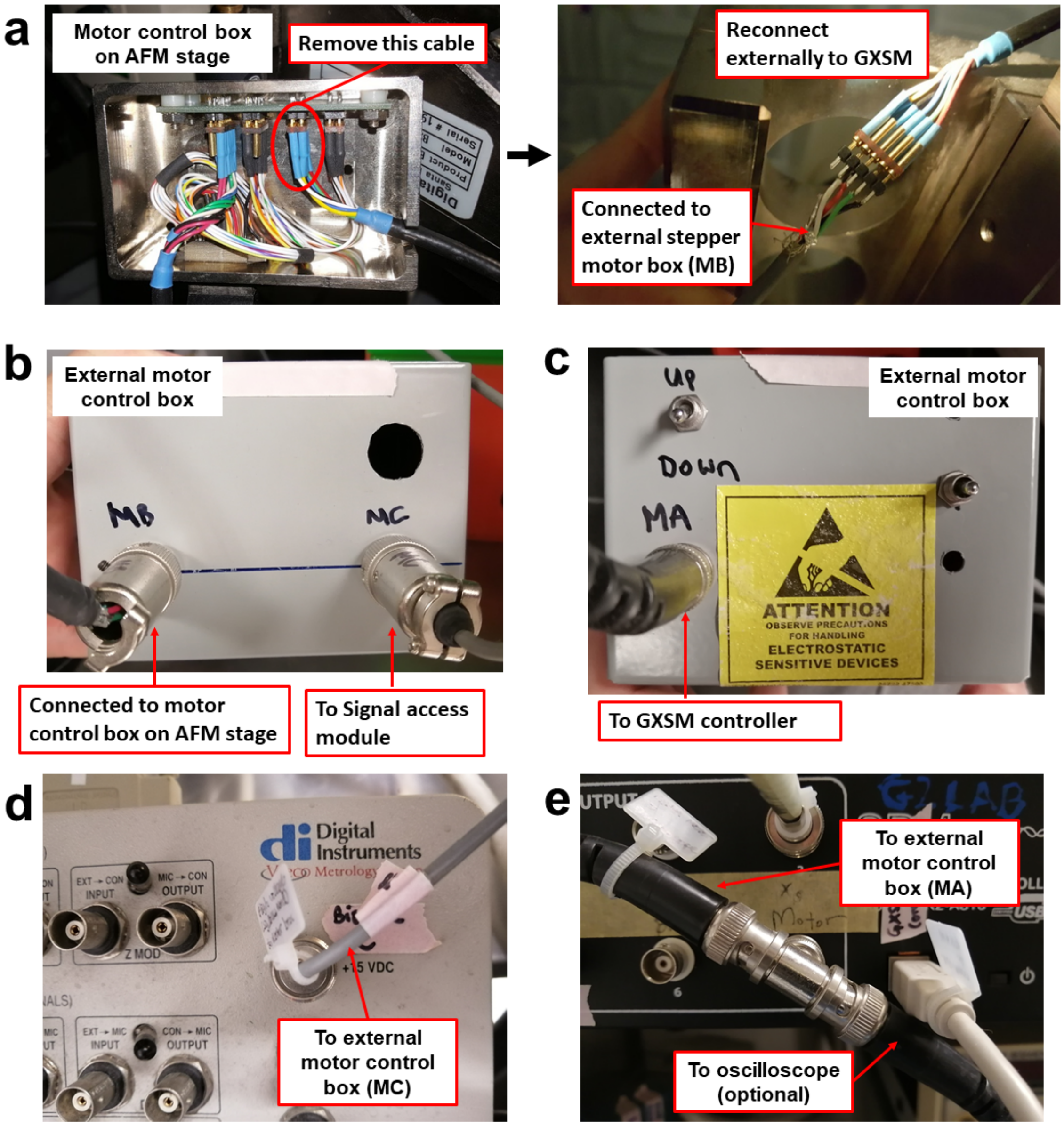

Figure S9: **Stepper motor connections. a.** Figure showing the 5 pin cable to be removed and connected to the external stepper motor control box. The corresponding connection is labelled **MB** on the external stepper motor control box. **b.** Back end of the external stepper motor control box showing the connections **MB** to the original Bioscope II motor control box and **MC** to the **+15VDC** port in the Signal Access Module. **c.** Front end of the external stepper motor control box showing the switch, which controls the Z-direction of the AFM head, and **MA** the connection to the GXSM controller. **d. +15VDC** connection port on the Signal Access Module connecting to the external stepper motor control box. **e. MOTOR** channel on the GXSM controller, which is connected to **MA** in the external stepper motor control box and to an oscilloscope.